Forschungsbericht 2017-35

Numerical Simulation Concept for Low-Noise Wind Turbine Rotors

Christof Rautmann

Deutsches Zentrum für Luft- und Raumfahrt
Institut für Aerodynamik und
Strömungstechnik
Braunschweig

169 Seiten
74 Bilder
11 Tabellen
84 Literaturstellen

DLR Deutsches Zentrum für Luft- und Raumfahrt

TU Braunschweig – Niedersächsisches Forschungszentrum für Luftfahrt

Berichte aus der Luft- und Raumfahrttechnik

Forschungsbericht 2017-11

Numerical Simulation Concept for Low-Noise Wind Turbine Rotors

Christof Rautmann

Deutsches Zentrum für Luft- und Raumfahrt
Institut für Aerodynamik und Strömungstechnik
Braunschweig

Diese Veröffentlichung wird gleichzeitig in der Berichtsreihe „NFL - Forschungsberichte“ geführt.

Diese Arbeit erscheint gleichzeitig als von der Fakultät für Maschinenbau der Technischen Universität Carolo-Wilhelmina zu Braunschweig zur Erlangung des akademischen Grades eines Doktor-Ingenieurs genehmigte Dissertation.

Numerical Simulation Concept for Low-Noise Wind Turbine Rotors

Von der Fakultät für Maschinenbau
der Technischen Universität Carolo-Wilhelmina zu Braunschweig

zur Erlangung der Würde
eines Doktor-Ingenieurs (Dr.-Ing.)
genehmigte Dissertation

von
Christof Rautmann, M.Sc.
geboren in Greifswald

eingereicht am:	08.12.2016
mündliche Prüfung am:	07.07.2017
Vorsitz:	Prof. Dr.-Ing. R. Radespiel
Gutachter:	Prof. Dr.-Ing. J. W. Delfs
	Prof. Dr.-Ing. F.-H. Wurm

2017

Summary

Wind power is the major technology in the transition from conventional energy towards greener, renewable energy. Especially for its public acceptance, the noise emission of the turbines plays an important role. Against this background, this thesis deals with the acoustic simulation of wind turbine noise. The work focuses on the main noise source of the rotor blades, the turbulent boundary layer trailing-edge interaction noise.

Numerous simulations of two-dimensional aerodynamic profiles were performed within the framework of the investigations. Therefore, several consecutive steps are necessary. An initial numeric flow simulation (CFD) yields the aerodynamic coefficients of the airfoils for the defined set of flow conditions. The turbulence model used in the CFD simulations provides time-averaged turbulence statistics which are subsequently used as input values for a stochastic turbulence reconstruction utilizing the fast random particle mesh method (FRPM). This enables the stationary average turbulence to be resolved in time and space and thus to generate the transient turbulent sound sources in the subsequent computational aeroacoustic simulation (CAA) with the acoustic solver `PIANO`. Sound pressure levels and spectra can be evaluated at arbitrary positions from the calculated spatio-temporal sound pressure field. Compared to other methods for the calculation of trailing-edge noise, the described hybrid approach (CFD/CAA) offers the advantage of high quality results with comparatively little computational effort (less than 20 h on 6 CPUs).

The validation of the results was based on published data of the BANC-II workshop. For all airfoils, the simulated spectra were within the uncertainty range of the measurement data. The accuracy was higher than with the classical semi-empirical calculation models usually used for this purpose. Physical effects, such as the apart drifting of the pressure and suction side spectrum with increasing angle of attack were correctly reproduced.

A best practice setup was created using parameter studies. Furthermore, the CFD-FRPM-CAA simulation toolchain was largely automized. Thus, arbitrary airfoil geometries could be examined for their aerodynamic as well as acoustic characteristics. Systematic variation of the DU-96-W180 airfoil geometry showed a noise mitigation potential of approx. 4 dB with the same aerodynamic performance (same L-over-D ratio c_L/c_D). Applying a forced transition of the wall boundary layer from laminar to turbulent flow results in a noise increase of approx. 3-4 dB.

On the basis of the simulation toolchain's results, characteristics of a low-noise airfoil were formulated, e.g. low turbulence kinetic energy values and a low positive pressure gradient at the suction side in the vicinity of the trailing-edge. A low-noise airfoil was developed and its effect on the turbine level was investigated using the NREL 5 MW reference rotor. Since three-dimensional CAA simulations showed a too high computational effort, an alternative procedure based on 2D airfoil sections and a blade element momentum method (BEM) for the rotor blade aerodynamics was developed. A 2 dB noise reduction without sacrificing the turbine's energy generation or loads could be achieved by using the low-noise airfoil. Furthermore, by varying the observer position around the turbine, it was possible to show that the lowest sound pressure levels occur directly in the rotor plane (crosswind direction from the turbine), but at this location they exhibit the highest temporal fluctuations. A phenomenon which is also known as amplitude modulation within the wind turbine acoustic community.

The developed calculation methods as well as their results provide a great potential for finding the next generation designs of wind turbine power plants. The future will show whether the noise reduction potentials will be used to increase public acceptance of wind turbines or to further optimize their costs.

Zusammenfassung

Windkraft spielt eine entscheidende Rolle beim Übergang von konventioneller Energieerzeugung zu regenerativen Energien. Besonders wichtig für die Akzeptanz von Windenergieanlagen (WEAs) ist deren Lärmemission. Vor diesem Hintergrund beschäftigt sich die vorliegende Arbeit mit der akustischen Simulation des Windturbinengeräusches. Der Fokus liegt dabei auf der Hauptlärmquelle der Rotorblätter, dem Hinterkantenschall durch Interaktion der turbulenten Grenzschicht mit der Hinterkante.

Im Rahmen der Untersuchungen wurden umfangreiche numerische Simulationen an zweidimensionalen aerodynamischen Profilen durchgeführt. Hierfür sind mehrere aufeinander aufbauende Schritte notwendig. Aus einer initialen Strömungssimulation (CFD) können die aerodynamischen Beiwerte des Profils bestimmt werden. Das Turbulenzmodell der CFD Simulation liefert zeitlich gemittelte Turbulenzstatistiken, die im weiteren Verlauf als Eingangswerte für eine stochastische Turbulenzrekonstruktion mit dem FRPM Verfahren genutzt werden. Hierin wird die stationäre Turbulenz wieder zeitlich und räumlich aufgelöst und dient anschließend als instationäre Turbulenzschallquelle in der aeroakustischen Simulation (CAA) mit dem Akustiklöser `PIANO`. Aus dem berechneten Schalldruckfeld können an beliebigen Positionen Schalldruckpegel und Spektren ausgewertet werden. Im Vergleich zu anderen Verfahren zur Berechnung von Hinterkantenschall bietet das beschriebene hybride Vorgehen (CFD/CAA) den Vorteil einer hohen Genauigkeit des Ergebnisses bei vergleichsweise geringem Rechenaufwand (weniger als 20 h auf 6 CPUs).

Eine Validierung der Ergebnisse erfolgte anhand veröffentlichter Daten aus den BANC-II Workshop. Für alle Profile lagen die simulierten Spektren innerhalb des Unsicherheitsbereichs der Messdaten. Die Genauigkeit war höher als mit alternativen klassischen semiempirischen Berechnungsmodellen. Physikalische Effekte, wie z. B. das Auseinanderdriften des Druck- und Saugseitenspektrums bei Anstellwinkelerhöhung, wurden korrekt wiedergegeben. Anhand von Parameterstudien wurde ein Best-Practice-Setup erstellt. Weiterhin wurde die CFD-FRPM-CAA Rechenkette weitestgehend automatisiert. Somit konnten beliebige Profilgeometrien sowohl auf ihre aerodynamischen als auch akustischen Kennwerte untersucht werden. Eine systematische Variation des DU-96-W180 Profils zeigte ein Lärmminderungspotential von ca. 4 dB bei gleicher aerodynamischer Güte (gleicher Gleitzahl c_L/c_D). Erzwungene Transition der Wandgrenzschicht von laminar zu turbulent hat eine Lärmerhöhung von ca. 3-4 dB zur Folge.

Mit den Ergebnissen wurden Eigenschaften eines lärmarmen Profils identifiziert, z.B. geringe Werte turbulenter kinetischer Energie und ein niedriger positiver Druckgradient auf der Saugseite nahe der Hinterkante. Ein lärmarmes Profil wurde entwickelt und sein Einfluss auf die Gesamtanlage am NREL 5 MW Referenzrotor untersucht. Da sich dreidimensionale CAA-Simulationen als zu rechenintensiv herausstellten, wurde ein alternatives Verfahren beruhend auf Simulationsdaten von 2D Schnitten und einer Blatt-Elementen-Methode (BEM) für die Rotorblattaerodynamik entwickelt. Mit dem neuen Profil konnte der Schalleistungspegel der Referenzanlage bei gleicher Leistung und identischen Lasten um bis zu 2 dB reduziert werden. Weiterhin ließ sich durch Variation der Beobachterposition relativ zur WEA zeigen, dass die Schalldruckpegel in der Rotorebene (querab der WEA) zwar am geringsten sind, sie jedoch die größten zeitlichen Schwankungen aufweisen. Ein Phänomen, dass in der Windkraftakustik als Amplitudenmodulation bekannt ist.

Die entwickelten Rechenverfahren sowie deren Ergebnisse bieten großes Potential Einzug in den Entwurf von Windenergieanlagen der nächsten Generation zu finden. Ob die Lärmminderungspotentiale dabei zur Akzeptanzsteigerung oder zur Kostenoptimierung der Turbinen verwendet werden, wird die Zukunft zeigen.

Contents

List of Figures

List of Tables

Nomenclature

Latin Symbols

A	rotor area
a	axial induction factor
$\hat{A}$	amplitude function
a'	tangential induction factor
B	number of blades
c_D	drag coefficient
c_f	skin friction coefficient
c_L	lift coefficient
c_n	normal load coefficient
C_P	turbine power coefficient
c_p	pressure coefficient
C_T	turbine thrust coefficient
c_t	tangential load coefficient
c_∞	ambient speed of sound
c_{M25}	pitching moment coefficient around $l_c/4$
c_M	pitching moment coefficient
$\overline{D}$	directivity
E	internal energy
e	specific internal energy
e_t	specific total energy
F	correction factor
f	frequency
$\boldsymbol{F}$	flux density tensor
$\vec{f}$	external forces vector
F_n	load normal to rotor plane
F_t	load tangential to rotor plane
$\mathcal{G}^0$	Gaussian filter kernel
h_r	Rayleigh wind speed distribution
h_r	Weibull wind speed distribution
k	wave number

k_t	turbulence kinetic energy (TKE)
l	length scale
$\vec{L'}$	Lamb vector
l_c	chord length
L_p	sound pressure level
L_W	sound power level
l_{ref}	reference length
M	Mach number
m	camber as fraction of chord
$\dot{m}$	mass flow
P	power
p	chordwise position of maximum camber
p	pressure
p'	fluctuating sound pressure
p_0	mean flow pressure
p_∞	ambient pressure
$\vec{Q}^F$	vector of fluxes over control volume
$\vec{q}$	heat flux vector
r	radius position
r	tip radius
$\mathcal{R}$	correlation
Re	Reynolds number
S_{ij}	mean strain tensor
St	Strouhal number
T	temperature
T	thrust
t	airfoil thickness
t	time
u	axial velocity component in the rotor plane
$\mathcal{U}$	spatiotemporal white-noise field
u_1	velocity in wake
$\bar{V_0}$	mean wind speed
$\vec{v}$	velocity vector
V_0	wind speed
$\vec{v}_0$	mean flow velocity vector
$\vec{W}$	vector of conserved quantities
x	coordinate
y	coordinate

z	coordinate

Greek Symbols

α	angle of attack
β	twist angle
δ	boundary layer thickness
δ^*	boundary layer displacement thickness
ϵ	error estimator
κ	ratio of specific heats (isentropic exponent)
κ	von Kármán constant
λ	tip speed ratio
μ	dynamic viscosity
ν	$= \mu/\rho$ kinematic viscosity
ω	angular velocity
ω	specific dissipation
Φ	flow angle
Φ	local angle from source to observer
φ	rotor blade position
ψ	stream function
ρ	density
ρ_0	mean flow density
ρ_∞	ambient density
σ	solidity
$\boldsymbol{\tau}$	stress tensor
τ_w	wall shear stress
Θ	local angle from source to observer
Θ	local pitch angle
$\dot{\theta}$	external heat
Θ_p	blade pitch angle

Indices

avg	average
c	convective
ff	far-field
i	direction i
j	direction j
k	direction k
max	maximum value

min	minimum value
OA	over all (sound pressure level)
obs	observer location
opt	optimum value
ref	reference or standard value
t	indicates fluctuating turbulent value
0	steady mean flow quantity

Abbreviations

AEP	Annual Energy Production
AM	Amplitude Modulation
AoA	Angle of Attack
ASD	Artificial Selective Damping
AWB	Acoustic Wind Tunnel Braunschweig
BANC	Benchmark for Airframe Noise Computations
BC	Boundary Condition
BEM	Blade Element Momentum Method
BL	Boundary Layer
BPM	Brooks, Pope and Marcolini (semi-empirical method)
CAA	Computational Aeroacoustics
CFD	Computational Fluid Dynamics
CFL	Courant–Friedrichs–Lewy (condition)
COE	Cost of Energy
DLR	Deutsches Zentrum für Luft- und Raumfahrt (German Aerospace Center)
DNS	Direct Numerical Simulation
DRP	Dispersion Relation Preserving (scheme)
EWEA	European Wind Energy Association
FFT	fast Fourier transformation
FRPM	Fast Random Particle Mesh (method)
FWH	Ffowcs-Williams and Hawkings (method)
GCI	Grid Convergence Index
GWEC	Global Wind Energy Council
HAWT	Horizontal Axis Wind Turbine
IAG	Institute of Aerodynamics and Gasdynamics (University of Stuttgart)
IEC	International Electrotechnical Commission
LDDRK	Low-Dissipation, Low-Dispersion Runge-Kutta (algorithm)
LEE	Linearized Euler Equations
LES	Large Eddy Simulation

NREL	National Renewable Energy Laboratory
NS	Navier Stokes (equations)
OASPL	Overall Sound Pressure Level
PIANO	Perturbation Investigation of Aeroacoustic Noise (CAA code)
PV	Photovoltaic
RANS	Reynolds Averaged Navier Stokes (equations)
RPM	Revolutions per Minute
SPL	Sound Pressure Level
TBL-TEN	Turbulent Boundary Layer Trailing-Edge Noise
TEN	Trailing-Edge Noise
TKE	Turbulence Kinetic Energy
TNO	The Netherlands Organization of Applied Scientific Research
TSR	Tip Speed Ratio

1 Introduction

Harvesting the wind has been a challenge to mankind ever since. The energy contained in the flowing mass of air was used over centuries by windmills to grind grain, pump water or propel other machinery. It drove sailing boats across the oceans long before the steam engine was invented and is used today by many wind and kite surfers to power their sporting goods.

With an energy resource that is quasi infinite, carbon emission free, decentralized usable and reasonable in its efficiency the focus nowadays shifts more towards wind turbines as energy producers. They are the cornerstone technology for most countries in their renewable energy politics. Ongoing improvements and the maturation of the technology led to turbine dimensions way beyond those of modern commercial airliners[1]. Due to the limited areas suitable to build wind farms turbines are moving closer to inhabited areas. Here, beside aesthetic aspects noise coming from the turbines is one of the major issues for the nearby living people. This thesis aims on the understanding of the noise generation process and the development of tools for low noise turbines.

The following chapter outlines the thesis by explaining the background of the wind turbine noise issue. A classification with view towards political and technical fields is given. The idea behind the chosen noise prediction approach is presented and compared to other state-of-the-art methods.

1.1 Motivation

Over the last decade energy politics around the world have changed progressively towards greener and renewable energy sources. In the aftermath of the Fukushima nuclear disaster in 2011 many governments decided to reduce their nuclear power production or even shut down all nuclear power plants as introduced within the German Energiewende (Energy transition). The transition from nuclear power and classical fuels (e.g. coal, oil and gas) to renewable energy (e.g. wind and solar photovoltaics (PV)) led to an increasing number of wind turbines which are apparent in today's environment. According to the Global Wind Energy Council (GWEC) a total amount of 432 GW of wind capacity was installed by the end of 2015 [1]. The worldwide development is depicted in Figure 1.1. In 2015 alone the volume of 63 GW of new capacity was added, representing an annual growth rate of 17 % (which is still below the average annual growth rate of 25 % over the last 18 years).

[1] For example the rotor blade of a Nordex N131 turbine with a length of 65.5 m is about 25.6 m longer than the wing of an Airbus A380-800 with a span of 79.8 m.

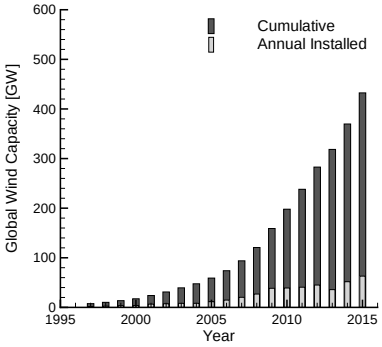

Figure 1.1: Annual installed and cumulative global installed wind capacity in GW. (Data from GWEC[1])

In Europe, where according to the European Wind Energy Association (EWEA) the installed cumulative capacity by the end of 2015 was 142 GW [2][2], the wind power sector is the number one in terms of newly installed capacity. Figure 1.2 (a) shows the distribution of the 28.9 GW overall newly installed capacity in 2015. With an amount of 44.2 % the wind power sector clearly has the biggest share, before solar PV (29.4 %), coal and gas (together 22.7 %) and other minor contributors (hydro, biomass, waste, etc: 3.6 %). In 2015, with a 15.6 % share of the total amount of installed capacity, wind energy was the third largest energy contributor in the EU behind coal (17.5 %) and gas (21.1 %). The distribution is depicted in Figure 1.2 (b).

Most turbines are still built in onshore wind farms, where space is limited. Especially in densely populated countries (e.g. Netherlands, Belgium, UK, Germany) this often leads to conflicts with the nearby living residents. Due to the growing turbine dimensions and their increased power not only aesthetic concerns arise, but also noise becomes an issue. This happens particularly in rural areas which used to be very quiet. Consequently, noise regulations govern the noise emissions of turbines, distances to residents or time frames of wind farm operations. So, from a wind farm operator point of view low noise turbines might be more profitable. It is therefore the task of a turbine manufacturer or designer to incorporate the acoustic design challenges into the development process. Hence, precise acoustic evaluation tools and methods are needed.

Beside mechanical noise in the turbines nacelle different flow-induced noise mechanisms can be distinguished for the rotor blades airfoils[3, 4], e.g. turbulent inflow noise, tip vortex formation noise, blunt trailing-edge vortex shedding noise, separation noise and turbulent boundary layer trailing-edge noise (TBL-TEN). It can be shown (refer to Section 2.3.7) that TBL-TEN represents the main noise source for modern Multi-Mega-Watt wind turbines. It is generated at the outer part of the rotor blades where the highest

[2] Totally installed wind capacity in Europe by 2015: 142 GW from which 11 GW (7.7 %) are offshore and 131 GW (92.3 %) are onshore.

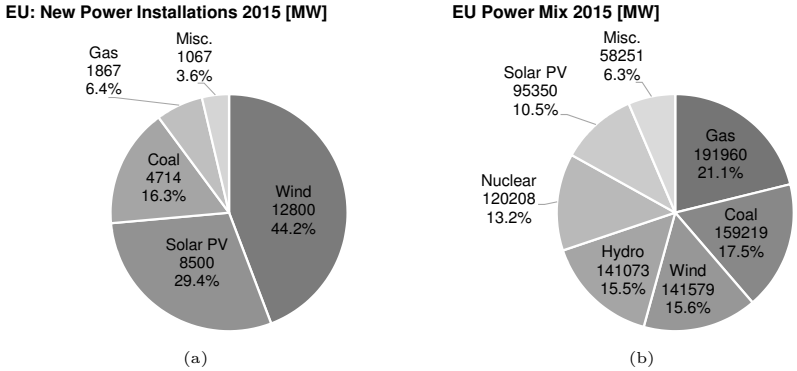

Figure 1.2: Overview of European Power data from 2015: (a) new installations by type; (b) distribution of the different energy sources by accumulated capacity. (Data from EWEA[2])

relative flow speeds are reached. This area is also the crucial part for the aerodynamic rotor blade design, as most of the rotor's torque is produced here (lever arm). Geometrical changes in this area need to be analyzed on the aerodynamic as well as aeroacoustic scale. Hence, the choice of a rotor blade cross section, or airfoil must be carried out with high confidence. This implies the need for precise calculation methods.

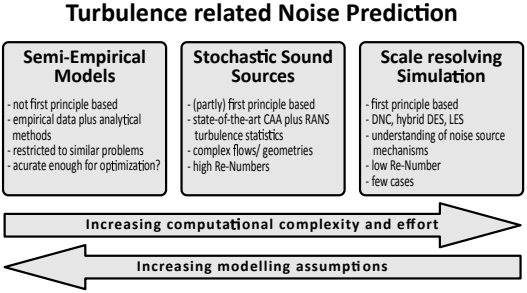

Figure 1.3: Turbulence related Noise prediction.

Depending on the complexity of the noise prediction problem, different prediction approaches are known (see Figure 1.3). The simplest and fastest approach is to use a semi-empirical method (e.g. the method proposed by Brooks, Pope and Marcolini[3] - BPM method) to determine TBL-TEN based on boundary layer parameters and acoustic measurements from reference airfoils. As this technique is based on measurements from NACA airfoils, it is prone to inaccuracy. Especially, when applied to arbitrary airfoils

with a geometrical shape significantly different from a NACA0012. A considerable level of simplification is introduced into the prediction and does not allow taking into account the full geometrical and flow complexity that might be present.

In contrast to that, scale resolving simulations, like Large Eddy Simulation (LES) approaches, could provide a clearer insight into the turbulent flow problem that underlies the aerodynamic sound generation process. As such, they yield the best level of physical modeling of the problem. For that purpose the Navier-Stokes equations are solved directly and only with the modest additional assumptions. This leads to a very high computational effort. Even on modern high-performance clusters computation times are out of reach for the simulation of complex flow problems for industrial application.

Stochastic approaches might bridge the gap between scale resolving methods and semi-empirical approaches. Herein a time-averaged solution of the RANS equations is used to prescribe the turbulent flow problem. Unsteady sound sources must be reconstructed from the turbulence statistics, which is in general incomplete as it lacks some information about the turbulence, e.g. the complete length scale anisotropy tensor. Nevertheless, the RANS information might be sufficient for a proper prediction of aeroacoustic trends even for relatively subtle changes in the problem statement such as flow velocity, angle of attack (AoA), or geometrical changes. Stochastic approaches have the advantage of being computationally more efficient than scale resolving simulation and as such allow to simulate full-scale high Reynolds number problems or a greater number of modifications in the aeroacoustic design process.

1.2 Previous Work

Trailing-edge noise prediction and mitigation have been (and still are) a challenging subject to the scientific community. Groundbreaking work was done by Sir Michael James Lighthill. He was the first one to formulate a theory for the sound emitted by a moving fluid. His famous aeroacoustic analogy where the sound field is represented by a distribution of acoustic quadrupole sources was first published in 1952 [5] and further improved towards the study of turbulence as a sound source in 1954 [6]. The work of Lighthill formed the basis for extensions towards reflection and diffraction effects of sound waves at solid boundaries by Curle [7]. Ffowcs Williams and Hawkings [8] extended the theory to the sound emitted by surfaces in arbitrary motion in 1969. In 1970 Ffowcs Williams and Hall [9] were the first to formulate a basic theory for the noise generation mechanism of the trailing-edge scattering problem. Assuming the vortex convection with the potential flow field around a semi-infinite flat plate (with zero thickness) and adapting Lighthill's quadrupole source model with the static fluid Green's function, they were able to derive some basic relations for the TBL-TEN problem. The velocity scaling with the fifth power of the flow velocity and the basic TBL-TEN directivity with a cardioid shape were direct results of their work. Several theories on the scattering half-plane issue were formulated mostly based on the Lighthill analogy. A good overview can be found in the classification done by Howe [10] in 1978. He distinguished three different categories:

- Theories based on Lighthill's acoustic analogy, for example by Ffowcs Williams and Hall [9], Crighton and Leppington [11] and others.

- Theories based on linearized hydroacoustic methods, e.g. Crighton [12] or the evanescent wave theory by Chase [13, 14] or Amiet's approach where the trailing-edge noise is generated by a scattering hydrodynamic pressure wave [15, 16].
- *Ad hoc* models which are not purely theoretical but involve source distributions and strengths which are determined empirically.

The prediction of trailing-edge noise was further promoted by the use of semi-empirical prediction models. In 1989 Brooks, Pope, and Marcolini [3] published their BPM (abbreviation of the initials of the three authors) model. It is based on extensive noise measurements of a NACA0012 airfoil at various Reynolds and Mach numbers, as well as several angles of attack. By appropriate scaling of peak levels, spectral shape and Strouhal numbers the model can be used for the noise prediction of arbitrary airfoils. It also includes other airfoil self-noise mechanisms e.g. stall or separation noise. However, as only symmetric NACA airfoils were used for the generation of the underlying data sets, the question remains of how accurate the BPM model performs for dissimilar airfoil geometries.

Other prediction approaches were done using diffraction theories for example by Brooks and Hodgson [17] or by Parchen [18]. A result of Parchen's work is the Blake-TNO model [18] where major turbulent boundary layer characteristics, e.g. the main velocity profile, turbulence kinetic energy and turbulence length scale, are linked to the trailing-edge noise generation. The BPM and the TNO model are incorporated into the freely available airfoil noise prediction software NAFNoise (NREL Airfoil Noise[19, 20]) developed by NREL for the design of wind turbine airfoils.

A good summary of the wind turbine noise issue can be found in the book by Wagner, Bareiss and Guidati [4]. Relevant theoretical background as well as prediction and mitigation approaches can be found here. Recent work in the wind turbine sector was done in the European project SIROCCO [21], where a noise reduction by the optimization of wind turbine airfoils was investigated. Moreover several contributions in the field of wind turbine noise mitigation of reduction by airfoil design can be found, for example the work of Lutz [22], Oerlemanns [23–26] and Hutcheson [27, 28] to only name a few of the most relevant publications. Moreover, simulation approaches were used to calculate the trailing-edge noise generation. Among others the hybrid RANS based approach presented by Ewert [29–31] showed the most promising results concerning result quality and computational efficiency and is thus used as a basis for the further development presented in this thesis.

1.3 Objectives

Within in the described background, trailing-edge noise is identified to be the main driver of the overall wind turbine noise. The scope should therefore be, to reduce this main noise contributor by a better understanding of the relevant relations between rotor blade geometry as well as aerodynamic and acoustic influence parameters. As discussed, the available semi-empirical or high fidelity tools are not suitable for this task under industrial aspects, because they either lack accuracy or they raise the computational effort to an unreachable amount.

Therefore, a combined modeling approach which connects flow and acoustic simulations with a high degree of accuracy but which is requiring a reasonable amount of computational resources will be chosen and validated for its use in the rotor blade design process. Starting from two-dimensional CFD and CAA simulations the generated results will be used in a toolchain to simulate the overall power and noise levels of a wind turbine. With this approach it should be possible to build a low noise rotor blade from the simulated and evaluated airfoils and prove the overall ability of the procedure. Condensed, the main objectives of this thesis are:

- Improve and validate the hybrid numerical approach for two-dimensional airfoil simulations.
- Identify the main noise drivers for wind turbine airfoil design.
- Improve the noise emission by geometric changes to a reference airfoil geometry without compromising its aerodynamic performance.
- Incorporate the aerodynamic and acoustic results into a toolchain for the prediction of a whole wind turbine's performance.
- Show the noise reduction effects in the rotor blade design.

1.4 Structure

The thesis is divided into five main parts. The theoretical background of wind turbine aerodynamics together with the relevant basics of the used numerical flow and acoustic simulations are presented in Chapter 2. Thereafter, the hybrid aerodynamic/aeroacoustic simulation toolchain for the precise and efficient simulation of trailing-edge noise is described in detail in Chapter 3. Validation results are presented in Chapter 4. Moreover, the influence of geometric airfoil variations is investigated by using a systematic approach, based on a wind turbine reference airfoil. A closer look into the noise driving parameters is conducted together with guidelines for a low noise airfoil design. The results on the airfoil level are used in Chapter 5 to calculated the noise and power of the NREL 5 MW reference turbine. The influence of a newly developed low noise airfoil is investigated and advantages on aerodynamic and acoustic performance are shown. The last part of the thesis (Chapter 6) summarizes the main insights and gives advices for future work.

2 Theory

As wind turbine noise is a multidisciplinary subject, a short theoretical review of the major issues is presented in this chapter. An introduction to specific wind turbine aerodynamics and the standard calculation models is given. The different operational modes are described to understand the necessity for noise reduction in certain wind speed ranges. A classification of typical wind turbine noise sources is discussed, from which the main source can be identified. For the noise calculation approach presented in this thesis aerodynamic (CFD) and aeroacoustic (CAA) simulations are used. The underlying fundamentals will be presented. To keep the overall extend of this chapter as short as possible, only the major aspects are discussed. For further insights the reader is directed to the published supplementing literature (e.g. see References [4, 32–37]).

2.1 Making Torque from Wind

The transformation of kinetic energy contained in the wind into mechanical energy and finally into electrical energy is the main purpose of a wind turbine. If it would be possible to extract all the energy contained in the wind by reducing its speed to zero, the maximum extractable energy would be:

$$P_{\max} = 1/2\dot{m}V_0^2 = 1/2\rho A V_0^3 \ . \tag{2.1}$$

Equation 2.1 shows, that the extractable energy depends cubically on the wind speed V_0, linearly on the fluid density ρ and also linearly on the (rotor) area A over which it is extracted. Two major trends in the wind turbine industry can directly be derived from this insights:

- **Increasing Turbine Dimensions:** With new manufacturing techniques and lighter materials longer rotor blades can be built to enlarge the area A over which the wind is harvested. Due to $A = \pi R^2$ the energy output scales quadratically with the rotor radius R or the rotor blade length. In addition, the fact that the wind speed V_0 increases with the height above the ground (atmospheric boundary layer) is utilized with higher towers.

- **Ideal Turbine Site:** Due to the cubical influence of the wind speed, sites with high constant wind speeds (e.g. coastal regions or flat table lands) are preferred for wind turbine projects. As space is limited, turbines are also build in places with lower wind speeds. The loss of energy output is often compensated by the turbine dimensions. Consequently, turbines are getting bigger and moving closer to populated areas.

The most common wind turbine design nowadays is the three bladed horizontal axis wind turbine (HAWT). The rotor is mounted in a upwind position in relation to the tower. The generator is placed in the nacelle. Depending on the turbine type, a gearbox is used to convert the rotational speed of the rotor. The turbine is controlled via its rotational speed and the incidence angle (pitch angle) of the rotor blades. This design has proven its technical and economic feasibility throughout all kinds of fields (manufacturing, cost of energy, transportation, erection, loads, etc.).

2.1.1 1D Momentum Theory

The extraction of mechanical energy from the wind can be described by a simple one-dimensional model. Herein, the rotor is considered as a permeable disc with ideal conditions. It is placed in a control volume. The flow is incompressible, frictionless and has no rotational velocity in the wake behind the turbine. The wind velocity decreases from V_0 far upstream of the rotor to u in the rotor plane and finally to u_1 in the wake (see Figure 2.1 (a)).

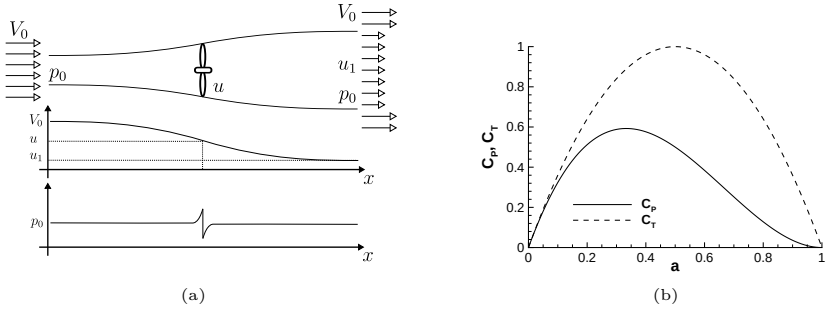

Figure 2.1: 1D momentum theory, (a) control volume, pressure and velocity around turbine; (b) thrust and power coefficient (C_P and C_T) as a function of the induction factor a.

By applying Bernoulli's equation and the equation of continuity, the pressure drop Δp over the rotor can be determined to:

$$\Delta p = \frac{\rho}{2}\left(V_0^2 - u_1^2\right) \ . \tag{2.2}$$

From that, the thrust force $T = \Delta p A$ acting on the rotor area A can be calculated. Together with the alternative derivation of $T = \rho u A\left(V_0 - u_1\right)$ from the axial momentum equation from Reference [33] the following relation for the wind speed u in the rotor plane can be found:

$$u = \frac{1}{2}\left(V_0 + u_1\right) \ . \tag{2.3}$$

After defining the axial induction factor a (with $u = (1-a)\,V_0$) and non-dimensionalizing power and thrust with respect to $P_{\max}$ and $T_{\max}$, the power and thrust coefficients (C_P and C_T) can be derived:

$$C_P = \frac{P}{\frac{1}{2}\rho V_0^3 A} = 4a\,(1-a)^2 \ , \tag{2.4}$$

$$C_T = \frac{T}{\frac{1}{2}\rho V_0^2 A} = 4a\,(1-a) \ . \tag{2.5}$$

By differentiating C_P with respect to a the maximum power coefficient $C_{P,max} = 16/27$ for $a = 1/3$ can be found. This theoretical maximum for an ideal wind turbine is also known as the Betz limit. It describes, that a maximum of approximately 59.3 % of the energy contained in the wind can be extracted if the wind speed is reduced to $u = 2/3V_0$ in the rotor area or $u_1 = 1/3V_0$ behind the turbine. Graphs for C_P and C_T are plotted against the axial induction in Figure 2.1 (b). The desired maximum C_P at $a = 1/3$ can clearly be seen.

So far, rotational effects in the wake of the turbine were neglected for the ideal rotor. For a more realistic model it is necessary to include these effects. This is done by introducing a local tangential induction factor a' (with $V_{\text{rot}} = (1+a')\omega r$) at each radius position r of the rotor. The rotor has the tip radius R. Due to the rotation of the blades an opposite rotation is imposed on the wake behind the turbine. Following Reference [33], an optimum relationship for the induction factors a and a' can be found:

$$a' = \frac{1-3a}{4a-1} \ . \tag{2.6}$$

It was shown by Glauert [38] that there is a reduction of efficiency due to the rotation in the wake. This effect decreases with increasing tip speed ratio (TSR) $\lambda = \omega R/V_0$. Figure 2.2 depicts the ratio between the power coefficient C_P and the Betz limit $C_{P,max} = 16/27$ for different tip speed ratios (i.e. different rotational speeds ω).

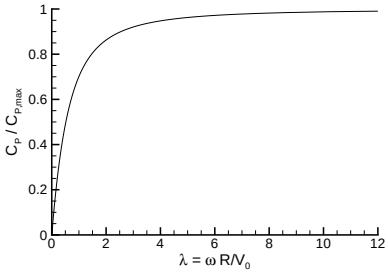

Figure 2.2: Efficiency of an optimum turbine including rotational effects.

For tip speed ratios greater than approximately six, only a small loss, in contrast to the idealizing case with neglected rotation effect, can be found. For example for a tip speed

ratio of $\lambda = 7.5$ a power coefficient of $C_P = 0.983 \cdot C_{P,max} = 0.5825$ could be reached for an ideal turbine. For a real turbine losses due to aerodynamic friction as well as three-dimensional flow phenomena at the blade root and tip lead to an even lower value, usually around $C_P \approx 0.5$.

Figure 2.2 also explains the trend to go for high tip speed ratios on modern turbines. If this is done via the increase of the rotational speed ω, also the rotor torque $M = P/\omega$ could be reduced. This offers benefits for all mechanical parts (e.g. rotor shaft, bearings, gearbox, etc.). Unfortunately, this also results in a high tip speed ($V_{tip} = \omega R$), which is unfavorable due to acoustic reasons (see Section 2.3.2).

2.1.2 Blade Element Momentum Method (BEM)

The classical BEM method is used to calculate thrust, power and the steady loads of a wind turbine rotor at a given point of operation (wind speed, RPM, pitch). In addition to the 1D momentum theory the shape of the rotor blades and their aerodynamic properties are taken into account. Therefore, a control volume over the spanwise extension of the rotor blade is discretized into N elements with no radial dependency and no lateral flow across the elements. A cross section of a blade element with relevant forces and velocities is depicted in Figure 2.3. It is located at the position r of the rotor blade with the spanwise extension R.

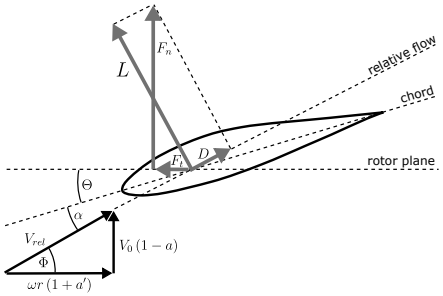

Figure 2.3: Local velocities and forces on a spanwise rotor blade element.

The angle between the airfoil chord and the plane of rotation is called pitch[1] (Θ). The angle of attack α can be calculated as the difference of the local flow angle Φ and the pitch. It is influenced by the velocities in the rotor plane, which are a result of the axial induction factors, the wind speed V_0 and the rotational speed ω of the section at the local radius position r ($\tan\Phi = \frac{(1-a)V_0}{(1+a')\omega r}$). Assuming that the coefficients for lift and drag, c_L and c_D, are known (either from a calculation method or measurements) the local section

[1] Note, that this angle is a combination of the local twist angle (which is a geometric property of the rotor blade) and the actual pitch angle which can be varied for pitch-regulated turbines.

forces, tangential and normal to the rotor plane F_t and F_n respectively their coefficients c_t and c_n, can be determined:

$$c_n = \frac{F_n}{\frac{1}{2}\rho V_{rel}^2 l_c} = c_L \cos\Phi + c_D \sin\Phi \ , \tag{2.7}$$

$$c_t = \frac{F_t}{\frac{1}{2}\rho V_{rel}^2 l_c} = c_L \sin\Phi - c_D \cos\Phi \ . \tag{2.8}$$

These results can be related with the 1D momentum theory. After introducing the solidity $\sigma(r) = \frac{l_c(r)B}{2\pi r}$, which is the ratio of the blade surface and surface of the annular area of the element (for B blades), the equations for the induction factors:

$$a = \frac{1}{\frac{4\sin^2\Phi}{\sigma c_n} + 1} \ , \tag{2.9}$$

$$a' = \frac{1}{\frac{4\sin\Phi\cos\Phi}{\sigma c_t} - 1} \tag{2.10}$$

can be found. Now, the induction factors can be calculated iteratively by solving the equation for the flow angle Φ and the corresponding aerodynamic forces at the chosen point of operation (see Appendix A.1 for a detailed description). As each annular control volume is - per definition - independent from the others, each radial position can be solved on its own. Finally Prandtl's tip loss factor (correction for a finite number of rotor blades) and the Glauert correction (correction for induction factors $a > 0.4$) need to be considered to yield the full picture (see also Appendix A.1 for more details).

One of the major wind turbine attributes - the power curve - can be computed using the BEM method. If this function of shaft power against wind speed is combined with a probability density function $f\left(V_i < V_0 < V_{i+1}\right)$ for the occurrence of certain wind speeds at a specific location, the annual energy production (AEP) can be calculated. The function $f\left(V_i < V_0 < V_{i+1}\right)$ is typically obtained from a Weibull or Rayleigh distribution for the mean wind speed ($\bar{V_0}$). It includes correction factors for the local meteorological and siting effects (landscape, vegetation, obstacles). They can be taken from the literature, e.g. Refernce [39]. By the AEP the turbine efficiency can be evaluated in an economical kind of sense. Basically, the only input data needed therefore is the rotor blade design (geometry, aerodynamic coefficients) and the operational conditions at the proposed location. The low computational resources to conduct the BEM method and the precise results in comparison with measurements made it the industry standard for quick estimations of new turbine designs. Note, that it is important to provide the method with precise input data, e.g. aerodynamic coefficients or meteorological conditions in order to provide high quality results. Aerodynamic phenomena (e.g. stall effects) can only be evaluated by a limited accuracy due to the two-dimensional modeling approach. High fidelity calculation methods (e.g. CFD simulations) are thus needed in the design phase of a rotor blade.

2.1.3 Turbine Operation

The efficiency of a wind turbine depends on its control algorithm. Some basic aspects for pitch regulated HAWTs with variable speed[2] are discussed in the following. The interplay of specific turbine parameters like tip speed ratio ($\lambda = \omega R/V_0$), rotational speed (ω), power coefficient (C_P) and pitch angle (Θ) with the wind speed (V_0) is depicted in Figure 2.4 for a generic HAWT. It can be seen, that the turbine exhibits four distinct states of operation throughout the increasing wind speed V_0.

- **State I:** For very low wind speeds the energy contained in the wind is not enough to turn the rotor. The turbine is idling and waiting for V_0 to increase. Once the so-called cut-in wind speed is reached, the rotor begins turning and mechanical energy is converted into electrical energy. The rotational speed is constant and determined by the minimum speed allowed by the partial converter. This leads to a relative high λ above the optimal tip speed ratio λ_{opt} and thus to a reduced C_P below $C_{P,max}$. The pitch is zero.
- **State II:** Further increase of the wind speed brings the power coefficient to its maximum value of $C_{P,max}$[3]. The rotational speed of the rotor is increased related to the wind speed in order to keep the tip speed ratio constant at the optimum λ_{opt}. As a result of that, local angles of attack at each section of the blade stay constant (see Figure 2.3). Energy output increases with the third power of V_0 but is still below rated power. The pitch is zero.
- **State III:** The maximum rotational speed of the partial converter is reached and thus limits further increase of ω. While the rotational speed is held constant from the beginning of state III the tip speed ratio decreases with increasing V_0. The power coefficient moves slightly away from its maximum. The energy output is still growing with approximately the third power of the wind speed and the pitch is still zero.
- **State IV:** The turbine reaches rated power (P_{rated}) and the energy output is now held constant over the increasing wind speed. This is done by the increase of the pitch angle Θ. The intended loss of C_P is compensated by the higher amount of kinetic energy contained in the incoming flow. The local angles of attack are decreased. Finally the turbine will stop its operation (not shown in Figure 2.3) at the cut-off wind speed of around $2.5 \sim 3 \cdot V_0$ to avoid critical loads outside the desired design conditions.

For the acoustic evaluation of a wind turbine the states II and III are of primary interest. For state II the local sections angle of attack stays constant ($\lambda_{opt} = const.$), while the flow speed (Reynolds and Mach number) increases because of the increasing ω. For a standard turbine design, this range of maximum C_P corresponds with the maximum

[2] The predominant amount of currently installed turbines utilizes this control strategy, where the blades can be rotated around the pitch axis in order to adjust the local incidence angles and thereby determine the aerodynamic forces. In contrast to that, smaller turbines from the early years of wind power had fixed rotor blades and were only be controlled by variable rotor speeds. Increasing wind speeds in combination with a fixed maximum rotational speed led to high angles of attack at the rotor blades and finally to stalled flow conditions with reduced forces. This, so-called stall regulation, is only applicable for small turbines as loads and vibrations can become very high.

[3] Modern wind turbines can reach $C_{P,max}$ values around 0.5 which is still below the Betz-limit of $16/27 \approx 0.593$ for an ideal wind turbine (ref. Section 2.1.1).

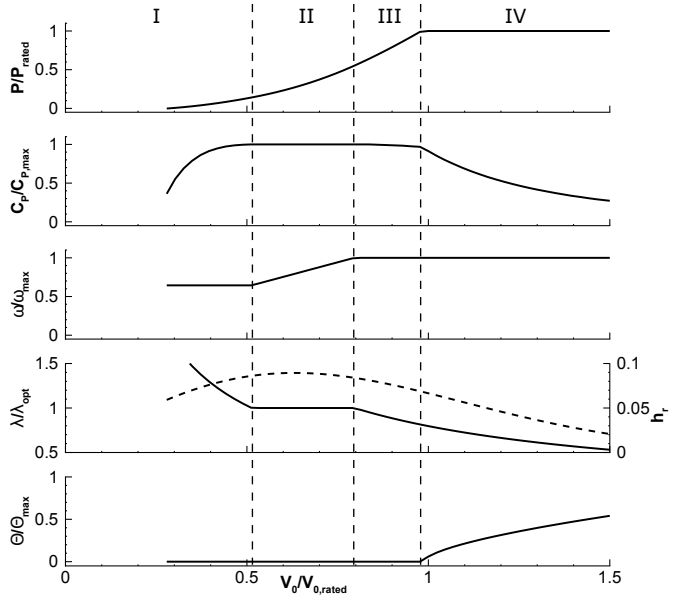

Figure 2.4: Operational parameters of a generic HAWT (dashed graph indicates typical probability of wind speed occurrence h_r)

probability h_r of the occurrence of the mean wind velocity $\overline{V}_0$. Consequently, most of the turbine operation hours are within this wind speed range. In state III the magnitude of the incoming flow velocity for each blade segment is constant, while the angle of attack is increasing with the wind speed up to the point where the rotor blades are pitched. Close to rated power (just before the blades are pitched) the local angles of attack reach their maximum values. Amongst others, the influence of these two parameters (incoming flow vector and angle of attack) on the emitted noise of the turbine will be investigated. For state IV the wind turbine noise issue vanishes, as the turbine noise levels stay nearly constant (constant tip speed due to limited ω) At the same time, the background noise levels (eg. wind whistling through the trees) steadily increase. The turbine noise is masked by the background noise.

2.2 Aerodynamics - CFD

A short theoretical review of the relevant aspects for the numerical flow simulation is given in this section. Individual settings and chosen models are further described in Section 3.2 in Chapter 3.

2.2.1 Governing Equations

The behavior of a compressible fluid is described by the conservation equations for mass, momentum and energy. These equations are an extension of the Euler equations and include the effects of viscosity on the flow. They were derived independently by Claude Louis Marie Henri Navier and Sir George Gabriel Stokes in the first half of the nineteenth century. In the conservative differential form the Navier-Stokes (NS) equation system reads:

$$\frac{\partial \rho}{\partial t} + \nabla \cdot (\rho \vec{v}) = \dot{m} \tag{2.11}$$

$$\frac{\partial \rho \vec{v}}{\partial t} + \nabla \cdot (\rho \vec{v} \vec{v}) + \nabla p = \nabla \boldsymbol{\tau} + \vec{f} + \dot{m} \vec{v} \tag{2.12}$$

$$\frac{\partial \rho e_t}{\partial t} + \nabla \cdot (\rho e_t \vec{v}) + \nabla (\rho \vec{v}) = -\nabla \vec{q} + \nabla \cdot (\boldsymbol{\tau} \vec{v}) + \dot{\theta} + \vec{f} \vec{v} + \dot{m} e_t \tag{2.13}$$

In the above equations ρ represents the fluid density, $\vec{v}$ the velocity vector, p the pressure and $e_t = e + \frac{1}{2}\vec{v}^2$ the specific total energy. On the right hand side of the equations the source terms for mass $\dot{m}$, external forces $\vec{f}$ and external heat $\dot{\theta}$ can be found. The viscous stresses in the fluid are represented by the stress tensor $\boldsymbol{\tau}$ and the heat flux is denoted as $\vec{q}$. The stress tensor can be calculated by the Stokes hypothesis $\boldsymbol{\tau} = \left(\nabla \vec{v} + {}^t\nabla \vec{v} - \frac{2}{3}\boldsymbol{I} \nabla \cdot \vec{v}\right)$, where μ represents the dynamic viscosity of the fluid. For the heat flux Fourier's law of heat conduct $\vec{q} = -k \nabla T$, with the heat conductivity k and the temperature T can be used. Together with the thermal and caloric equation of state, $p = \rho R T$ and $e = c_v T$ (with the gas constant R and the specific heat at constant volume c_v) the equation system can be solved for the seven unknowns (ρ, $\vec{v}$, p, e_t, T).

2.2.2 Numerical Simulation Technique

Apart from some special cases, where an analytical solution is possible, the equation system (2.11-2.13) is solved numerically by means of computational fluid dynamics (CFD). Each CFD simulation thereby consists of the same basic steps:

- **Pre-Processing:** Definition of the problem geometry, discretization of the volume under investigation (mesh) and setting of the boundary conditions and flow parameters.
- **Solving:** Choice of physical models and equations (viscosity, compressibility, turbulence treatment, boundary treatment, etc.), iteratively solving of the equations until a defined convergence criteria is reached.
- **Post-Processing**: Evaluation of flow parameters or integral results for the problem, visualization and analysis of the results.

To iteratively solve the equations a discretization of the governing equations (2.11-2.13) is needed. In the majority of the CFD codes finite volume methods are used for this. The main advantage of a finite volume method is that the mesh can be of an unstructured type. An acceleration of the mesh generation process, especially for complex geometries is

possible. The conservation equations are normally used in their conservative integral formulation for the control volume V with the vector of conserved quantities $\vec{W}$ (containing ρ, $\vec{v}$, e) and the flux density tensor $\boldsymbol{F}$ (containing the fluxes):

$$\frac{\partial}{\partial t}\iiint_V \vec{W} = -\iint_{\partial V} \boldsymbol{F}\cdot\vec{n}dS \ . \tag{2.14}$$

See Appendix A.2 for more details. Basically, the change of the flow parameters in a fixed (time and space) control volume can be determined from the fluxes over its boundaries ($\vec{Q}^F$):

$$\frac{d}{dt}\vec{W} = -\frac{1}{V}\cdot\vec{Q}^F \ . \tag{2.15}$$

For the integration of the fluxes over the control volume boundary different discretization schemes can be used[4]. They distinguish in their numerical stability, order of accuracy and computational effort. Moreover, artificially added numerical dissipation has to be considered. For most engineering CFD applications in a subsonic flow regime central schemes show good results with reasonable stability.

The spatial discretization of the computational domain around the geometry is done with a mesh (or grid). Different commercial and non-commercial grid generators can be used for the mesh generation. Areas with large gradients (for example boundary layers) need to be resolved with a high mesh density. Moreover, certain quality criteria (grid lines parallel and perpendicular to the flow direction, limited skewness and aspect ratios, moderate size increase of neighboring cells) need to be observed. The mesh generation is a crucial process of each CFD simulation. Poor mesh quality can easily lead to wrong results.

In a CFD simulation, the flow problem can be computed either for a time-averaged (steady state) or a time-accurate (unsteady) solution. Time-accurate solutions require more disk space and computational time. For attached flow conditions (for example a wind turbine airfoil under normal operation conditions) steady-state solutions are the best tradeoff of computational resources and accuracy. Moreover, the commonly used turbulence models also average out the temporal fluctuations even in an unsteady simulation so that only large scale effects (like flow separation) can be resolved.

CFD simulations offer a lot of insights into specific flow characteristics and phenomena. However, all subsequent steps and sub-models in the working process need to be carefully scrutinized by the user in order to avoid incorrect final results. Profound verification and validation steps are thus crucial for high quality solutions.

2.2.3 Turbulence Modeling

By nature, most of the flows considered for technical applications (such as the flow around a wind turbine airfoil) are turbulent. Turbulent flows are unsteady, highly diffusive,

[4] Depending on the used discretization method and the flow problem under investigation a whole lot of different discretization schemes and variations of them can be used (e.g. upwind, downwind, central). The complete description of the discretization and solving procedure can fill books and is skipped here as it is not the main matter of this thesis (for further reading see References [36, 40])

highly dissipative, rotational and three-dimensional. The flow regime is characterized by irregular and seemingly random (chaotic) rapid variations of pressure and flow velocity in time and space on many different length scales, which all interact with each other. The complete simulation of all turbulent features, down to the smallest length scale with a DNS (Direct Numerical Simulation) or LES (Large Eddy Simulation), is a very challenging task. Even with modern high performance computing equipment the calculation times are very high - especially for high Reynolds number flows - and not applicable in an industrial environment.

For engineering applications the modeling of turbulence is the state of the art method. Therefore Reynolds Averaged Navier Stokes equations (RANS) are used. Herein, the flow quantities are decomposed into a mean part and a fluctuating part (e.g $u = \bar{u} + u'$). As a consequence additional terms result from all non-linear terms in the NS equations. These additional terms are of the form $-\rho\overline{u_i' u_j'}$ and are called Reynolds stresses. They built the Reynolds stress tensor. The calculation of the Reynolds stress tensor is needed in order to close the equation system (closure problem). In analogy to the viscous stresses (where the stresses are proportional to the viscosity and the velocity gradient) the Reynolds stresses are often determined from a (turbulent) eddy viscosity μ_t and the gradient of the mean velocity (Boussinesq Approximation).

$$-\rho\overline{u_i' u_j'} = 2\mu_t S_{ij} - \frac{2}{3}\rho k_t \delta_{ij} \tag{2.16}$$

With the mean strain tensor S_{ij} and the mean turbulence kinetic energy k_t as:

$$S_{ij} = \frac{1}{2}\left(\frac{\partial \overline{u}_i}{\partial \overline{x}_j} + \frac{\partial \overline{u}_j}{\partial \overline{x}_i} - \frac{2}{3}\frac{\partial \overline{u}_k}{\partial \overline{x}_k}\delta_{ij}\right) \tag{2.17}$$

and

$$k_t = \frac{1}{2}\left(\overline{u_1' u_1'} + \overline{u_2' u_2'} + \overline{u_3' u_3'}\right) \tag{2.18}$$

and the Dirac delta function as:

$$\delta_{ij} = \begin{cases} 1 \text{ for } i = j \\ 0 \text{ for } i \neq j \end{cases} . \tag{2.19}$$

Different turbulence models based on empirical constants can be used for the modeling of the eddy viscosity and the turbulence kinetic energy k_t. In this thesis, the two-equation SST-k-ω turbulence model as proposed by Menter[41] is used. It is a combination of the k-ϵ-model with:

$$\mu_t = C_\mu \rho k^2/\epsilon \tag{2.20}$$

and the k-ω-model with:

$$\mu_t = \rho k/\omega \tag{2.21}$$

from Wilcox[42]. Note, that in this context ω is a turbulence dissipation quantity rather than an angular frequency. Two more differential equations are solved in the iteration process for k and $\omega = \epsilon/k$. They contain several model constants which were determined from a comparison with experimental data (see Reference [42]).The SST-k-ω turbulence model overcomes the disadvantages of using the k-ϵ-model in near wall regions with strong adverse pressure gradients by switching to the more accurate k-ω-model. Precise results throughout a wide range of applications made this model very popular. It became the industry standard for most flow simulation problems.

2.3 Aeroacoustics - CAA

A review of the relevant theoretical background for the aeroacoustic phenomena and their numerical simulation is given in this section. The main focus is put on the simulation of trailing-edge noise. The actual settings and modeling decisions made for the individual simulations can be found in Section 3.3.

2.3.1 General

Sound is characterized by small fluctuations of a quantity Φ' around its steady mean value Φ_0. For example, the pressure $p(t)$ can be divided into:

$$p\left(t\right) = p_0 + p' \ . \tag{2.22}$$

With the steady part p_0:

$$p_0 = \lim_{T\to\infty} \frac{1}{T} \int_{-\frac{T}{2}}^{\frac{T}{2}} p\left(t + t'\right) dt \tag{2.23}$$

and the fluctuating sound pressure $p'(t)$. Introducing this principle into the governing equations for fluid dynamics (2.11 - 2.13), together with standard perturbation techniques for linearization, leads to the wave equation for the pressure fluctuation p' (see Appendix A.3 for further details):

$$\frac{1}{c_0^2} \frac{\partial^2 p'}{\partial t^2} - \Delta p' = Q_p \ . \tag{2.24}$$

And similar for the velocity perturbation (or particle velocity) $\vec{v}'$:

$$\frac{1}{c_0^2} \frac{\partial^2 \left(\nabla \cdot \vec{v}'\right)}{\partial t^2} - \Delta \left(\nabla \cdot \vec{v}'\right) = Q_v \ . \tag{2.25}$$

Note, that in the above equations the medium is supposed to be stagnant ($\vec{v}_0 = 0$) and the mean density and mean pressure are assumed constant ($\rho_0 = \text{const.}$, $p_0 = \text{const.}$). Δ denotes the Laplacian, where $\Delta = \nabla \cdot \nabla$. If the compression and expansion of the medium is supposed to be isentropic ($s = \text{const.}$) , the relationship

$$p' = c_0^2 \rho' \tag{2.26}$$

holds. Where, for a perfect gas the propagation speed of the disturbances (speed of sound) c_0 can be calculated as:

$$c_0^2 = \left(\frac{\partial \rho}{\partial p}\right)^{-1} \Big|_{s=\text{const.}} = \kappa R T \tag{2.27}$$

Herein κ is the ratio of specific heats (or isentropic exponent), R the specific gas constant and T the absolute temperature. The Equations 2.24 and 2.25 are called wave equations. Their left hand side describes the wave dynamics of a perturbation wave (p' or $\vec{v}'$) in

time and space. The right hand side stands for the source terms Q_p and Q_v which are considered given and can be calculated for a perfect gas (e.g. air) as:

$$Q_p = \frac{1}{\kappa}\frac{\partial \dot{m}}{\partial t} + \frac{\kappa - 1}{c_0^2}\frac{\partial \dot{\vartheta}}{\partial t} - \nabla \cdot \vec{f}' \tag{2.28}$$

and

$$Q_v = \frac{1}{\rho_0}\left(-\Delta\dot{\theta}' + \frac{1}{c_0^2}\frac{\partial \nabla \cdot \vec{f}'}{\partial t}\right) . \tag{2.29}$$

It can be seen, that sound can be generated by either a mass source $\dot{m}$, external forces $\vec{f}'$ or a heat sources $\dot{\theta}$ (respectively their time derivatives). Especially sources from unsteady local fluid forces and their interaction with inhomogeneities are the most important ones for the wind turbine trailing-edge noise problem.

2.3.2 Acoustic Analogy

A further look into the nature of aeroacoustic sources is given by Lighthill's famous acoustic analogy[5]. It can be derived by subtracting the divergence of the momentum equation (Eq. 2.12) from the time-derivative of the continuity equation (Eq. 2.11) and neglecting mass flow sources and external forces.

$$\frac{\partial^2 \rho}{\partial t^2} = \nabla \cdot \nabla \cdot (\rho \vec{v}\vec{v} + p\boldsymbol{I} - \boldsymbol{\tau}) \tag{2.30}$$

The term $c_0^2 \Delta\rho$ needs to be subtracted from both sides of Equation 2.30 to achieve the form of the wave equation. Additionally, the fluctuating quantities for the acoustic pressure p' (Equation 2.22) and similar fluctuating density ρ' are introduced. The mean values are supposed to be constant ($p_0 = const.$, $\rho_0 = const.$).

$$\frac{\partial^2 \rho'}{\partial t^2} - c_0^2 \Delta\rho' = \nabla \cdot \nabla \cdot \left(\rho \vec{v}\vec{v} + \left(p' - c_0^2\rho'\right)\boldsymbol{I} - \boldsymbol{\tau}\right) \tag{2.31}$$

Equation 2.31 is the basis of the acoustic analogy as formulated by Lighthill. The left hand side represents a wave equation (see Equation 2.24) while the right hand side is the double divergence of the so-called Lighhill stress tensor. It is now possible to directly connect the wave equation with the aeroacoustic sources calculated from the governing equations. The Lighthill stress tensor $\boldsymbol{T} = \left(\rho \vec{v}\vec{v} + \left(p' - c_0^2\rho'\right)\boldsymbol{I} - \boldsymbol{\tau}\right)$ consists of three parts which can be identified as distinct source mechanisms.

- $\rho\vec{v}\vec{v}$: changes in flow velocity (e.g. turbulence)
- $s' = p' - c_0^2\rho'$: changes in entropy s (e.g. temperature changes due to combustion)
- $\boldsymbol{\tau}$: changes in viscous friction (usually unimportant)

If in Equation 2.28 one would identify $\dot{m} = 0$, $\dot{\vartheta} = 1/(\kappa - 1)\partial s'/\partial t$ and $\vec{f}' = \nabla \cdot (\boldsymbol{\tau} - \rho\vec{v}\vec{v})$, these source quantities are equivalently related to the Lighthill sources.

Introducing source quantities in in Equation 2.28 directly leads to the pressure from of the Lighthill analogy:

$$\frac{1}{c_0^2}\frac{\partial^2 p'}{\partial t^2} - \Delta p' = \nabla \cdot \nabla \cdot (\rho \vec{v}\vec{v} - \boldsymbol{\tau}) + \frac{1}{c_0^2}\frac{\partial^2}{\partial t^2}\left(p' - c_0^2 \rho'\right) \ . \tag{2.32}$$

If no entropy changes are present the source mechanisms can be reduced to the turbulence introduced velocity changes as the main noise source for aeroacoustic problems. With his concept for the sound radiation caused by fluctuating Reynolds stresses, Lighthill found the following dependence of the sound intensity I of the main parameters:

$$I \propto \rho_0 c_0^3 M^8 \left(\frac{l}{r}\right)^2 \alpha^2 \ . \tag{2.33}$$

Herein l denotes the dimension of the turbulent region, α is the normalized turbulence intensity and $M = v_\infty / c_\infty$ the Mach number. Note, that the intensity scales with the eighth power of the Mach number for free turbulence (e.g. as present in a jet or homogeneous boundary layers). This dependence is also known as the eighth power law. It shows, that especially at low Mach numbers ($M < 1$), free turbulence is a very inefficient sound source.

2.3.3 Scattering Half Plane

When the turbulent structures interact with an edge in the flow their inefficient quadrupole radiation is superimposed by an additional, much more efficient dipole type radiation. Ffowcs Williams and Hall [9] investigated the sound field due to a turbulent eddy in the vicinity of a scattering half plane. They could show, that the intensity I now scales with the following relation with respect to the main parameters:

$$I \propto \rho_0 c_0^3 \cos^3\left(\bar{\Theta}\right) M^5 \frac{sl}{r^2}\alpha^2 \cdot \sin(\phi) \sin^2\left(\frac{\Theta}{2}\right) \ . \tag{2.34}$$

In the above equation, a convecting turbulent stream of the height l and the width s is assumed. The definition of the respective angles relative to the flow (ϕ and Θ) can be seen in Figure 2.5.

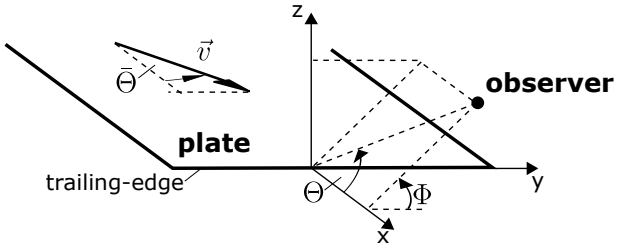

Figure 2.5: Flow over the semi-infinite half plane with the respective angles.

The flow vector is aligned parallel to the surface. Usually, it passes the trailing-edge with an angle of 90 ° ($\bar{\Theta} = 0\,°$).

Comparing Equation 2.33 with Equation 2.34 it can be seen, that the radiation efficiency changes from M^8 to M^5 for turbulent eddies in the vicinity of an edge. As the flow Mach number for typical wind turbine issues is $M = 0.3$ or less, this indicates a clearly more efficient radiation for the presence of an edge by a factor of M^{-3}. Remember, that this not only holds for incoming turbulence which hits the rotor blades but also for self produce turbulence in the boundary layer of the airfoils.

2.3.4 Governing Equations

The simulation of noise generation and propagation is the main objective of a CAA code. With the `PIANO` code, the inviscid dynamics of the perturbations are simulated over a steady, time-averaged mean-flow field. Interactions of vorticity with solid structures or gradients in the flow field can be covered. In the code non-dimensionalized quantities are used for the calculations. The reference values for the nondimensionalization are the reference length l_{ref} (usually the chord length $l_{\mathrm{ref}} = l_c$), the pre-multiplied ambient pressure $\kappa p_\infty = \rho c_\infty^2$ (with the isentropic exponent κ), the ambient density ρ_∞ and the ambient speed of sound c_∞. The mean flow and FRPM quantities are non-dimensionalized as follows (values with dimension are indicated by *):

$$x_i = \frac{x_i^*}{l_{\mathrm{ref}}},\ \vec{v} = \frac{\vec{v}^*}{c_\infty},\ \rho = \frac{\rho^*}{\rho_\infty},\ p = \frac{p^*}{\rho_\infty c_\infty^2},\ k = \frac{k^*}{c_\infty^2},\ \omega = \frac{\omega^* l_{\mathrm{ref}}}{c_\infty}\ . \tag{2.35}$$

At standard conditions where $T_{\mathrm{ref}} = 288.15\,\mathrm{K}$ and $p_\infty = 101325\,\mathrm{Pa}$ the reference density is $\rho_\infty = 1.225\,\mathrm{kg/m^3}$ and the reference speed of sound is $c_\infty = 340.3\,\mathrm{m/s}$. The nondimensionalization has to be considered for all steps throughout the acoustic simulation process. For the interpretation of absolute results, a reverse conversion needs to be done. An equation system for the small perturbations about the (viscous) mean flow may be derived from the Navier-Stokes Equations (refer to Section 2.2.1). For this purpose they are put into the primitive formulation for the quantities of interest (ρ,$\vec{v}$,p) to yield (non-dimensional):

$$\frac{\partial \rho}{\partial t} + \vec{v}\cdot\nabla\rho + \rho\nabla\cdot\vec{v} = 0\ , \tag{2.36}$$

$$\frac{\partial \vec{v}}{\partial t} + \vec{v}\cdot\nabla\vec{v} + \frac{1}{\rho}\nabla p = \frac{M}{Re}\frac{1}{\rho}\nabla\cdot\boldsymbol{\tau}\ , \tag{2.37}$$

$$\frac{\partial p}{\partial t} + \vec{v}\cdot\nabla p + p\nabla\cdot\vec{v} = \frac{M}{Re}\left[(\kappa-1)\,\boldsymbol{\tau} : \nabla\vec{v} - \frac{1}{Pr}\nabla\cdot\vec{q}\right]\ . \tag{2.38}$$

In the equations above, the Reynolds number for the reference length L and the reference dynamic viscosity μ_∞ is expressed by $Re = \rho_\infty v_\infty L/\mu_\infty$ and the Prandtl number by $Pr = \mu_\infty c_p/k_\infty$ (with the reference thermal conductivity k_∞). The non-dimensional heat flux density is represented by $\vec{q}$ (referenced to $k_\infty c_0^2/\left(c_p\,(1-\kappa)\,L\right)$).

To account for the amplitude fluctuations about a steady mean-flow a further splitting of the variables, to a steady mean flow quantity and a small fluctuating part, is done (e.g. $(\rho,\vec{v},p,\boldsymbol{\tau},\vec{q}) = (\rho_0,\vec{v}_0,p,\boldsymbol{\tau}_0,\vec{q}_0) + \epsilon\,(\rho',\vec{v}',p',\boldsymbol{\tau}',\vec{q}')$). Following the linearization strategy

described in Refernce [43] and assuming that direct viscosity and heat conduction effects on the perturbation field may be neglected (i.e. $\boldsymbol{\tau}'$ and $\vec{q}'$), the linearized Euler equations or LEE can be derived:

$$\frac{\partial \rho'}{\partial t} + \vec{v}' \cdot \nabla \rho_0 + \vec{v}_0 \cdot \nabla \rho' + \nabla \cdot \vec{v}_0 \rho' + \nabla \vec{v}' \rho_0 = 0 \ , \tag{2.39}$$

$$\frac{\partial \vec{v}'}{\partial t} + \vec{v}' \cdot \nabla \vec{v}_0 + \vec{v}_0 \cdot \nabla \vec{v}' + \frac{1}{\rho_0} \left(\nabla p' + \rho' \vec{v}_0 \cdot \nabla \vec{v}_0 \right) = 0 \ , \tag{2.40}$$

$$\frac{\partial p'}{\partial t} + \vec{v}' \cdot \nabla p_0 + \vec{v}_0 \cdot \nabla p' + \kappa \left(\nabla \cdot \vec{v}_0 p' + \nabla \cdot \vec{v}' p_0 \right) = 0 \ . \tag{2.41}$$

The equation system can be solved for the acoustic field with the variables ρ', $\vec{v'}$ and p'. The (turbulent) mean-flow field is represented by the variables ρ_0, $\vec{v_0}$ and p_0.

The acoustic perturbation equations (APE[44]) are a modification of the LEE so, that vorticity or entropy convection is entirely prescribed by the source term (which adds stability to the equation system by removing the vorticity convection mode from the governing equations), whereas acoustic generation and radiation is simulated dynamically. The APE realize a solution to the wave operator of irrotational flow. Together with proper right-hand side volume sources this becomes an acoustic analogy based on the wave operator. The source term mainly acts as a vorticity source term. Sound due to the interaction of vorticity with the trailing-edge is generated as part of the CAA simulation step. The vortex dynamic is dominated by linear contributions to the source terms. Non-linear contributions mainly deemed responsible for sound generation of free turbulent flow are neglected. It was observed that for edge noise problems the incorporation of turbulence decay into the source model had no effect on the spectra compared with simulations based on frozen turbulence.

Neglecting entropy fluctuations and density fluctuations, due to turbulent velocities in (cold) low Mach number flows, the APE-4 equation system (with corresponding right-hand sides) reads:

$$\frac{\partial p'}{\partial t} + c_0^2 \nabla \left(\rho_0 \vec{v'} + \vec{v_0} \frac{p'}{c_0^2} \right) = 0 \ , \tag{2.42}$$

$$\frac{\partial v'}{\partial t} + \nabla \left(\vec{v_0} \cdot \vec{v'} \right) + \nabla \left(\frac{p'}{\rho_0} \right) = \vec{L'} \ . \tag{2.43}$$

The turbulent sources are represented by the fluctuating Lamb vector $\vec{L'}$. Quantities with subscript 0 denote mean-flow variables. The prime indicates fluctuating quantities. The perturbation velocity is represented by $\vec{v'}$. The fluctuating acoustic pressure p' and fluctuating density ρ' are linked via

$$p' = c_0^2 \rho' \ , \tag{2.44}$$

where the squared speed of sound c_0^2 is defined by the mean-flow variables (with the isentropic exponent of air $\kappa = 1.4$):

$$c_0^2 = \kappa \frac{p_0}{\rho_0} \ . \tag{2.45}$$

2.3.5 Numerical Simulation Technique

Turbulent noise sources are computed from synthetic turbulence generated by the FRPM code (see Section 2.3.6). In the computational domain this turbulence is coupled with the CAA solver. For the spatial discretization of a CAA code it is important to use a scheme which minimizes the numerical dispersion[5]. This can be done either via the use of high-order discretization schemes or even better with the dispersion relation preserving (DRP) scheme proposed by Tam & Webb [45]. Figure 2.6 depicts the resolution capacity of different differencing schemes. The product of the wave number $k = 2\pi/\lambda$ (with the wave length λ) and the grid spacing Δx is compared to the product of the approximated wave number k_{modified} and the the grid spacing. The approximated wave number can be calculated from the coefficients c_k of the differencing scheme:

$$k_{\text{modified}}\Delta x = i \sum_{j=-N}^{N} c_k e^{-ij(k\Delta x)} \ . \tag{2.46}$$

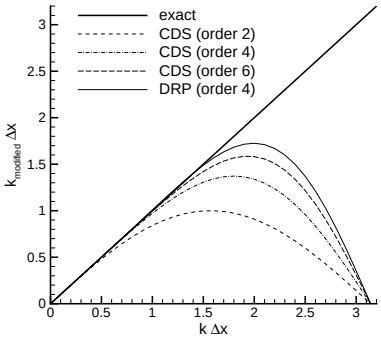

Figure 2.6: Resolution capacity of different finite differencing schemes (CDS = central differencing scheme; DRP = dispersion relation preserving scheme).

See Reference [43] for the used coefficients in `PIANO`. A favorable scheme would follow the exact solution ($k = k_{\text{modified}}$) throughout a wide wave number range. It can be seen, that this is true for the DRP scheme with fourth order accuracy up to $k\Delta x \approx 1.5$. A central differencing scheme of the same order could only realize waves up to $k\Delta x \approx 0.8$ and even with sixth order accuracy only waves up to $k\Delta x \approx 1.0$. Considering the accuracy $k\Delta x \approx 1.0$ (conservative assumption), acoustic waves up to a wave length $\lambda_{\min} \approx 2\pi\Delta x \approx 6.3\Delta x$ can be resolved by the DRP scheme almost without dispersion. If the minimum resolvable

[5] Dispersion means the phenomenon in which the phase velocity of a wave depends on its wave length or frequency. Dispersion occurs when the phase velocities of the traveling acoustic waves are not the same for all frequencies. If it is introduced by a numerical scheme it reduces the accuracy of the simulated results and yields artificial noise.

wave lengths is thus resolved by at least seven points, the maximum frequency can be calculated to:

$$f_{\max} = \frac{c_0}{\lambda_{\min}} = \frac{c_0}{7 \cdot \Delta x} \ . \tag{2.47}$$

In the numerical code `PIANO`, seven point stencils are used for the numerical approximation of the derivatives with the DRP scheme. Special formulations for non-uniform grid spacings as well as modified stencils for unsymmetrical stencils (e.g. at mesh boundaries) are applied. Further details can be found in Reference [43].

For very short wave lengths ($f > f_{\max}$), which cannot be represented correctly due to the finite grid spacing, the artificial selective damping (ASD) approach of Tam, Webb and Dong [46] is used. The damping can be applied to the whole computational domain or to distinct physical areas (for example around the airfoil's leading-edge).

The temporal discretization is done using a two-step low-dissipation, low-dispersion Runge-Kutta (LDDRK) algorithm from Hu et al. [47]. The coefficients in this approach are chosen to minimize dissipation and dispersion errors without compromising the stability of the procedure. It also has the advantage of low storage requirements. The coefficients as well as further details can also be found in [43].

2.3.6 FRPM

For the preparation of unsteady vortex sound sources a synthetic turbulence method developed at DLR is adopted to force the linearized applied acoustic perturbation equations. The stochastic approach is especially well suited for aeroacoustics purposes, e.g. realizing a four-dimensional time and space based prediction of fluctuating sources in a restricted volume. This volume is called the source patch (or short: patch). The Random Particle-Mesh Method (RPM) was first published in 2005 by Roland Ewert [48]. It allows to synthetically realize the time-dependent, turbulent fluctuations from averaged turbulence statistics. It is discretized by equidistantly distributed mean flow stream lines that cover the resolved source domain. To avoid this elaborate patch generation procedure, the method was extended to the fast Random Particle-Mesh Method (FRPM) in 2007[29] so, that a single block Cartesian background mesh could be used for its spatial discretization. Fluctuating sound sources are computed in the cell vertices of the background mesh (patch) and further interpolated onto the CAA mesh. Despite the discretization procedure RPM and FRPM rely on the same theoretical background. In the following, the term FRPM will be used for the descriptions.

FRPM generates synthetic turbulence by means of spatially and temporally fluctuating quantities. These fluctuations accurately reproduce provided autocorrelations and integral length scales, for example from a time-averaged RANS simulation. According to [49] the two-point spatiotemporal correlation $\mathcal{R} = \overline{\psi^t\left(\vec{x},t\right)\psi^t\left(\vec{x}+\vec{r},t+\tau\right)}$ of a turbulent quantity ψ^t can be written as:

$$\mathcal{R}\left(\vec{x},\vec{r},\tau\right) = \hat{R} \cdot \exp\left(-\frac{|\tau|}{\tau_s} - \frac{\pi\left(\vec{r}-\vec{v}_c\tau\right)^2}{4l^2}\right) \ . \tag{2.48}$$

The relevant parameters are the time and length scales τ_s and l, the mean square value of the correlated quantity $\hat{R}$ and the convection velocity $\vec{v}_c$.

The turbulence is generated by spatially filtering of a convective white-noise field with a Gaussian filter of the respective length scale. A scaling with the local variance (e.g. the turbulence kinetic energy k_t or TKE) yields the final fluctuating quantities. Due to the filter kernel an energy spectrum of Gaussian shape is realized.

For the turbulence reconstruction FRPM realizes a fluctuating stream function ψ^t of the following form for the n-dimensional problem:

$$\psi^t\left(\vec{x},t\right) = \int_{V_S^{(n)}} \hat{A}^{(n)} \mathcal{G}^0\left(\vec{x}-\vec{x}',l\right) \mathcal{U}\left(\vec{x}',t\right) d^n\vec{x}' \ . \tag{2.49}$$

Fluctuating turbulent values are represented by the superscript t. The term $\hat{A}^{(n)}$ is responsible for the local amplitude scaling (as a result of the local turbulence statistics k_t and ω from RANS). The Gaussian filter kernel is represented by $\mathcal{G}^0\left(\vec{x}-\vec{x}',l\right)$ and $\mathcal{U}\left(\vec{x}',t\right)$ is the used spatiotemporal white noise field which contains the random values. The integration is done over the volume $V_S^{(n)}$, where the unsteady sources are realized. The filter kernel is normalized, so that the autocorrelation $\overline{\psi^t\left(\vec{x},t\right)\psi^t\left(\vec{x},t\right)} = 1$ for $\hat{A} = 1$. The filter kernel depends on the distance $\vec{x}-\vec{x}'$ and the kernel width l which represents the local length scale.

For the simulation of frozen turbulence the white-noise field $\mathcal{U}\left(\vec{x}',t\right)$ is uniquely defined by the properties:

$$\overline{\mathcal{U}\left(\vec{x},t\right)} = 0 \ , \tag{2.50}$$

$$\overline{\mathcal{U}\left(\vec{x},t\right)\mathcal{U}\left(\vec{x}+\vec{r},t\right)} = \delta\left(\vec{r}\right) \ , \tag{2.51}$$

$$\frac{D_0}{D_t}\mathcal{U}\left(\vec{x},t\right) = 0 \ . \tag{2.52}$$

Here, $\delta\left(\vec{r}\right)$ denotes the multi-dimensional Dirac δ-function. The term $\frac{D_0}{D_t}$ in Equation 2.52 denotes the material derivative, e.g. $\frac{D_0}{D_t}\varphi = \frac{\partial}{\partial x}\varphi + \vec{v}_0 \cdot \nabla\varphi$. It is responsible for the convective property of the fluctuation model. So, the white noise field is passively convected with the mean-flow velocity ($\vec{v} = \vec{v}_0$). It is discussed in Reference [29], that for larger length scales l the convection velocity will be an average over the surrounding mean-flow field. For example in turbulent boundary layers, where the convection velocity $\vec{v}_c$ is slower than the velocity outside the boundary layer ($\vec{v}_c \approx 0.6...0.7\vec{v}_\infty$), this length scale dependent averaging yields the correct physical behavior of the turbulent noise sources and the proper Mach scaling. The Gaussian filter kernel reads:

$$\mathcal{G}^0 = \exp\left(-\frac{\pi}{2}\frac{\left|\vec{x}-\vec{x}'\right|^2}{l^2}\right) \ . \tag{2.53}$$

It is shown in Reference [48] that the spatial normalized correlation

$$\mathcal{R}^0\left(\vec{r},\tau\right) = \frac{\overline{\psi\left(\vec{x}+r,t+\tau\right)\psi\left(\vec{x},t\right)}}{\overline{\psi\left(\vec{x},t\right)\psi\left(\vec{x},t\right)}} \tag{2.54}$$

satisfies $\mathcal{R}^0(0,0) = 1$ and

$$\mathcal{R}^0(\vec{r},0) = \exp\left(-\frac{\pi}{4}\frac{|\vec{x}-\vec{x}'|^2}{l^2}\right) . \tag{2.55}$$

For the realization of turbulent vortex sound sources, the turbulent velocity $\vec{v}^t$ is calculated from the curl of the stream function:

$$\vec{v}^t = \nabla \times \vec{\psi} . \tag{2.56}$$

Taking again the curl of the turbulent velocity $\vec{v}^t$ yields the fluctuating vorticity vector:

$$\vec{\omega}^t = \nabla \times \vec{v}^t . \tag{2.57}$$

With the results of Equation 2.56 and 2.57 the linearized fluctuating Lamb vector that occurs as the major vortex-force source term on the right-hand side of the momentum equation (Equation 2.43) can be calculated to:

$$\vec{L}' = w(\vec{x})\left(-\vec{\omega}_0 \times \vec{v}^t - \vec{\omega}^t \times \vec{v}_0\right) . \tag{2.58}$$

In the above given source term $\vec{v}_0$ and $\vec{v}^t$ are the mean and fluctuating velocity that define the unsteady flow velocity via $\vec{v} = \vec{v}_0 + \vec{v}^t$. The local source term weighting is represented by $w(\vec{x})$. Furthermore, $\vec{\omega}_0 = \nabla \times \vec{v}_0$ and $\vec{\omega}^t = \nabla \times \vec{v}^t$ denote the mean and fluctuating vorticity, respectively. While $\vec{\omega}_0$ and $\vec{v}_0$ are results of the RANS simulation, $\vec{v}^t$ and $\vec{\omega}^t$ are results of the FRPM turbulence reconstruction.

It was shown by Ewert [29], that for the two-dimensional case the amplitude $\hat{R}$ in Equation 2.48 must be set to

$$\hat{R} = \frac{4l^2 k_t}{3\pi} \tag{2.59}$$

to reconstruct convecting isotropic frozen turbulence with the appropriate statistics given by RANS (according to the desired correlation given in Equation 2.48). The resulting longitudinal correlation function is a Gaussian ($f(r) = \exp\left(-\frac{\pi}{4}\frac{\vec{r}^2}{l^2}\right)$) with an integral length scale l. The length scale can be directly determined from the RANS solution. For a k-ω turbulence model the corresponding relation reads:

$$l = \frac{c_l}{C_\mu}\sqrt{\frac{k}{\omega}} . \tag{2.60}$$

According to Reference [50] the constant $c_l \approx 0.54$ can be approximated for a modified van Kármán turbulence spectrum. Together witch the constant $C_\mu = 0.09$ from the turbulence model, the length scale factor $l_{\text{fac}} = \frac{c_l}{C_\mu} \approx 6.0$ can be determined.

The simulations are carried out by generating one turbulent two-dimensional slice out of the three-dimensional turbulent field (see Reference [30]) and conducting a CAA simulation on a two-dimensional mesh. The result is a severe benefit in terms of computational times, compared to other scale resolving turbulence simulations (e.g. LES or DNS). It

was shown in Reference [30] that a 2D-to-3D correction has to be applied to the spectrum to correct the two-dimensional simulation for the three-dimensional sound radiation:

$$L_{p,3D} = L_{p,2D} + 10\log\left[\frac{C}{2\pi}\frac{L}{R}M_\infty\right] \quad . \tag{2.61}$$

In the above equation taken from Reference [30], L represents the wing span of the three-dimensional wing section, R is the observer distance, C is a constant for the relation of the spanwise correlation length scale of the sources ($C \approx 1.4...1.6$ according to Reference [3]) and M_∞ represents the free stream Mach number. The correction needs to be applied to the two-dimensionally simulated narrow-band spectrum $L_{p,2D}$ to calculate the three-dimensional spectrum $L_{p,3D}$. However, the correction does not reveal an explicit frequency dependence. Therefore, despite a constant off-set, the procedure provides the correct spectral shape. Thus, relative differences in the spectra should be covered. A constant off-set has to be removed which is determined by the calibration of the results with a set of experimental reference data.

2.3.7 Wind Turbine Noise Sources

The overall wind turbine noise is composed of several contributions from different sources. A distinct differentiation can be found in the literature [3, 4, 51, 52]. A short roundup of this will be given in the following section.

Basically, the noise emitted from an operating wind turbine can be divided into two types:

- **Mechanical Noise:** Due to the relative motion between mechanical parts of the turbine noise is emitted. Sources are for example: the gearbox, the generator, hydraulic units or cooling equipment[52]. All these contribute to airborne and structure-borne noise of broadband and tonal character[6]. Classical reduction methods, like the insulation of specific parts, flexible couplings between different machinery or precise and noise-optimized manufacturing of gearbox gears, can efficiently reduce mechanical noise. Moreover an acoustic casing in the nacelle helps to keep contributions to the overall turbine sound to a minimum. All in all this leads to an overbalance of the second basic noise source - the aerodynamic noise - for modern wind turbines.
- **Aerodynamic Noise:** By its nature a wind turbine creates aerodynamic forces via the relative motion between the rotor blades and the surrounding air. Thereby, multiple complex flow phenomena can occur which can lead to flow induced noise sources. Especially the steady increase of rotor diameters throughout the last decades, together with high tip speeds, emphasized velocity depending scaling effects of some noise generation mechanisms. Due to its high relative velocity the outer part of the rotor blade is the main contributor.

Different self induced aerodynamic noise sources exist in the flow regime around the rotor blades. A differentiation was given by Lowson [51]. They are depicted in Figure 2.7.

The main self noise sources are:

[6] Tonal noise contributions are critical for wind turbines as they can lead to a penalty which is added on the overall turbine sound power level. The mitigation of tones emitted from wind turbine machinery is therefore a main focus in the design process.

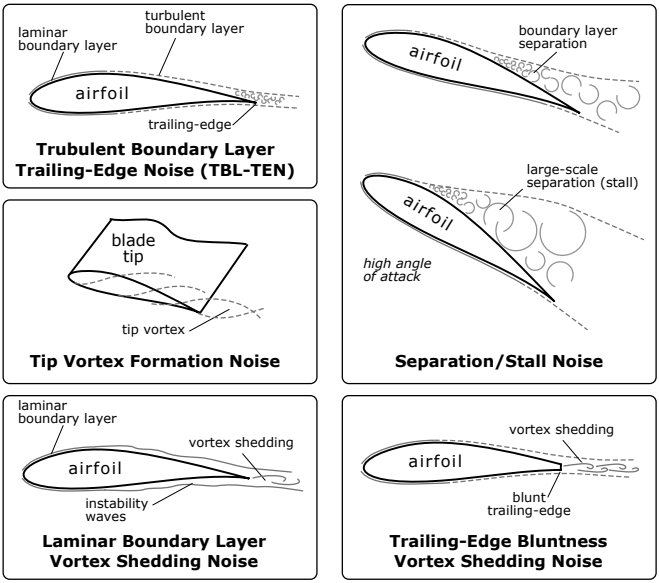

Figure 2.7: Airfoil self noise mechanisms. (Picture reffering to [51])

- **Turbulent Boundary Layer Trailing-Edge Noise (TBL-TEN):** A broadband noise source caused by the interaction of boundary layer turbulence with the trailing-edge.
- **Tip Vortex Formation Noise:** A broadband noise source due to the interaction of the tip turbulence (vortex) with the blade surface.
- **Stall or Separation Noise:** A broadband noise source which is caused by the interaction of the massive turbulence in the separated flow with the blade surface. It is the most prominent noise source when separation is present. It can be up to 10 dB louder than attached flow condition [53].
- **Laminar Boundary Layer Vortex Shedding Noise:** A tonal noise caused by a feed back loop in the laminar (normally pressure side) boundary layer of the airfoil.
- **Trailing-Edge Bluntness Vortex Shedding Noise:** Tonal noise triggered by the von-Kármán like vortex shedding behind the blunt trailing-edge.
- **Noise from Flow over Surface Disturbances (Holes, Slits):** Tonal noise which is caused by instable shear flows over surface disturbances.

Different studies on wind turbine noise[23] have shown that TBL-TEN is the dominant noise source for modern multi-Megawatt wind turbines as long as no separated flow is present in the outer rotor blade parts[4]. This finding is further underlined by tests with trailing-edge devices which showed good results in reducing TBL-TEN and thereby the

overall levels [21, 22, 54]. As TBL-TEN scales with the fifth power of the relative flow velocity[9], the outer parts of the rotor (with high relative velocities) are of most interest.

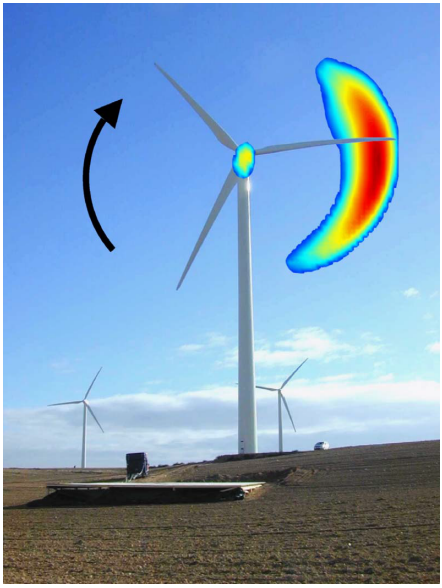

Figure 2.8: Visualization of aerodynamic noise on downward moving rotor blade. (Picture from [23])

Figure 2.8 shows the aerodynamic noise of the downward moving blade of a G58 wind turbine taken by Oerlemans[23] in the framework of the European SIROCCO project[21]. The noise signature is visualized with an acoustic array of 148 microphones situated in front of the turbine. Two main noise sources can be distinguished: the nacelle and the outer part of the rotor blade. Note, that it is clearly visible that the main noise source (indicated by the red color) is the rotor blade. The strength of the aerodynamic noise is first increasing from the blade root towards the tip, due to the increased relative velocity(velocity scaling) with increasing rotor radius, but then decreases again at the tip part of the blade. This circumstance can be observed at almost every modern wind turbine. The reason is the reduction in the airfoil incidence angle and chord length in the blade tip region to reduce lift production and tip vortex formation. Thereby, two noise mechanisms (tip vortex formation noise and TBL-TEN) are reduced in this region. Consequently, the most interesting part of the rotor blade for noise reduction is the utmost third fraction of the blade and not necessarily the blade tip[7]. Aside from noise,

[7] This statement relies on the assumption, that a conservative low noise tip design is used (reduction of chord and twist). Low noise airfoils or the reduction of the tip vortex strength might also help to increase the blade's twist angles and thereby the lift production in the tip area. Thus, a higher energy production of the turbine might be possible.

aerodynamic design constraints need to be considered in this region, as most of the rotor's torque is produced here. A high influence on the turbine's energy production as well as loads is implied. Therefore, changes in airfoil geometry must always be analyzed against the backdrop of aerodynamic as well as acoustic performance.

3 Simulation Methods

The choice of a wind turbine airfoil has been a challenging task in rotor blade design ever since. Competing functions have to be weighed against each other in order to find the "perfect" airfoil. Most times, it is even hard to define what is understood as "perfect" and what is not. In this thesis, the main focus is put on aerodynamic as well as aeroacoustic aspects[1]. They are analyzed in a combined, first principle based numeric procedure which consists of multiple consecutive steps.

An overview of the toolchain is given in Section 3.1. Sections 3.2 and 3.3 comprise all information necessary to set up the aerodynamic and aeroacoustic simulation steps which are implied into the method. Due to the rather large amount of airfoils to investigate, automation scripts were generated for several steps of the procedure. The automation is described in Section 3.4. The methods shown in this chapter build the foundation for the analysis presented and discussed in Chapter 4. The validation of the described approach is shown in Section 4.1 by a comparison with available measurement data. While Chapter 3 and Chapter 4 deal mainly with the investigation of two-dimensional airfoil geometries, Chapter 5 is dedicated to the performance of the whole wind turbine. The related methods for this full turbine investigation are presented in Chapter 5 as well.

3.1 Toolchain Overview

A combination of different simulation tools is used to determine the broadband trailing-edge noise signal of the airfoils under investigation and finally of a rotor blade comprising these airfoils. Besides that, several aerodynamic characteristics are analyzed. A rather large amount of data is recorded during the process which has the advantage that nearly all interesting parameters (acoustic as well as aerodynamic) can be evaluated from the available simulation data. The major steps of the toolchain which is depicted in Figure 3.1 are:

- **CFD Flow Simulation:** With the airfoil geometry (given as x and y coordinates) a simulation of the time-averaged turbulent flow field around the airfoil is conducted. In the rotor blade design process this data might already exist and a dual use is possible if the boundary layer is resolved correctly. From the CFD results the mean-flow variables (velocity vector $\vec{v}_0$, density ρ_0 and pressure p_0) are extracted for the CAA step. Moreover, the turbulence statistics are used as an input for the FRPM turbulence reconstruction. For more details on the CFD simulation see Section 3.2.
- **CAA Acoustics Simulation:** The time and space resolved fluctuating sound pressure field ($p' = f(\vec{x}, t)$) around the airfoil is simulated in the CAA step. For this purpose

[1] Nevertheless, structural requirements are considered in terms of geometrical boundary conditions in order to guarantee the structural strength and integrity of the airfoil geometry.

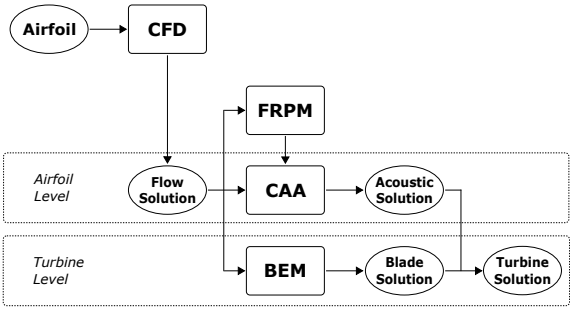

Figure 3.1: Schematic toolchain showing the consecutive steps for the simulation of aerodynamic and acoustic properties.

linear perturbation equations are solved. The required turbulent noise sources are calculated in the FRPM step. For more details on the CAA simulation refer to Section 3.3.

- **FRPM Turbulence Reconstruction:** For the acoustic simulation time resolved turbulent fluctuations are necessary as input values. As the flow simulation is based on RANS equations, where the turbulence is only modeled with a time averaged character, a procedure is required to overcome this lack of information. The FRPM[31, 55] (Fast Random Particle Mesh) method uses the turbulence statistics from RANS in combination with a stochastic procedure to reconstruct the four-dimensional time and space resolved turbulence in the source region. There, it is coupled with the acoustic solver. For more details on the FRPM turbulence reconstruction refer to Section 3.3.

- **BEM Turbine Simulation:** The link between the aerodynamic parameters of the airfoil and the performance of a turbine blade built from these airfoils can be found via the BEM (Blade Element Momentum) method. Herein the aerodynamic coefficients together with the blade geometry are used to calculate the turbine performance for chosen meteorological conditions (see Section 2.1). As the acoustic and aerodynamic performance of the airfoil is known from the previous simulations the final picture is now completed. It is possible to see if for example an acoustically improved airfoil has significant influence on the turbine performance. A trade-off between acoustics and performance (in terms of COE (cost of energy) and AEP (annual energy production)) can be derived for a whole wind turbine.

The procedure shown in Figure 3.1 can be used with two different levels of detail. On the airfoil level only representative parameters of the airfoils under investigation are analyzed. Aerodynamic coefficients as well as acoustic parameters can be compared to other airfoils or weighted against each other (Which airfoil has the least noise with the maximum L-over-D ratio?). Increasing the level of detail by conducting a BEM simulation (turbine level) yields performance parameters of the planned wind turbine. The performance of the chosen airfoil in a certain rotor blade design can be judged against the noise created by the blade (How large is the turbine's sound power level at a certain wind speed? What

would be the annual energy production for a given location?). By nature, these two levels are highly interactive. A low noise airfoil can only show its full advantages if it is used at its desired optimum point of operation (angle of attack, Reynolds number). The design parameters of the desired turbine have to be considered in advance to choose the right parameters on the airfoil level.

3.2 CFD

For the simulation of the flow field around the airfoil a two-dimensional CFD simulation is conducted. From the results integral coefficients for lift (c_L), drag (c_D) and pitching moment around the quarter chord point (c_{M25}) can be determined. Moreover, necessary inputs for the subsequent acoustic simulation (pressure, density, turbulence parameters) are calculated. The rather large amount of data helps to draw conclusions between aerodynamic and aeroacoustic parameters if further analyzed.

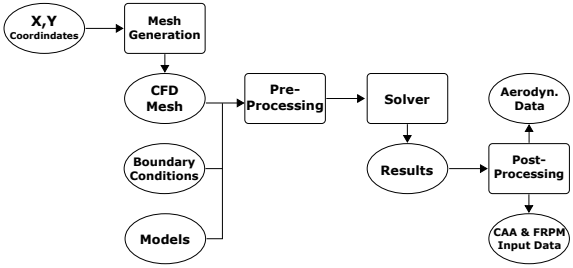

Figure 3.2: Schematic toolchain showing the consecutive steps for the CFD simulation.

The standard CFD workflow is shown in Figure 3.2. The simulations are carried out using the unstructured DLR in-house CFD solver `TAU`[56, 57]. Note, that each other CFD solver (commercial or open-source) might also be suitable for the simulations, as far as the prescribed flow values and turbulence statistics can be calculated[2].

From the known airfoil geometry (given in x and y coordinates and normalized to a chord length $l_c = 1$) a CFD mesh is generated in the flow domain. Boundary conditions as well as appropriate models (e.g. turbulence model, fluid model, etc.) are set in the pre-processing step. An iterative solution is then calculated by the solver. Finally, a post-processing of the data is done to extract relevant parameters and data for the subsequent steps. The overall time of such a process is normally determined by the computational time necessary to calculate the final (converged) solution. Nevertheless, the generation of the mesh can take a big share in overall time, especially for very complex geometries. If only parameters (like the angle of attack) are changed and the same mesh is used, the time for meshing and preparation of the simulation needs to be spent once only. Moreover, the turnaround time can be significantly reduced by automation.

[2] In a later stage of the thesis, CFD Simulations were also done using ANSYS CFX. With the same models as in `TAU` and same mesh strategy used, no significant differences between the results were found.

On standard hardware (6 CPU machine) it takes less than 20 minutes to conduct a CFD simulation for one set of input parameters. Thus, a whole angle of attack polar can be simulated in just a few hours.

3.2.1 Mesh

For each airfoil a two-dimensional computational domain is generated using the commercial grid generator `ICEM CFD`. With the use of replay-scripts it was possible to automate all steps of the mesh creation. In this way a consistent meshing approach with almost unvarying quality could be ensured for all geometries.

The domain's outer boundaries extend about 100 chord lengths around the airfoil to prevent unphysical interferences of the boundary conditions with the near airfoil flow. A hybrid meshing strategy is chosen where the viscous sub-layer and the near airfoil region are resolved by a structured grid and areas far away from the airfoil are resolved by a coarser, quad-dominated unstructured grid. This meshing strategy reduces cells in less interesting areas (far away from the airfoil) and thereby saves computational effort (time and storage space). The total number of grid cells is approximately 100k. A grid refinement study is shown in Section 3.2.3.

The near airfoil mesh is built in a C-type topology for airfoils with a sharp (one point) trailing-edge[3]. Throughout the airfoil surface 225 nodes are distributed along the upper side and the same number is also used for the lower side. Both sides are treated individually and are divided at the airfoil nose in order to set individual boundary conditions in the pre-processing (e.g. transition locations). Moreover, a separate post-processing of the results from both sides is possible. A smooth transition between different cell sizes along the surface is enforced with an exponential growth ratio for neighboring cells not bigger then the factor 1.2. For the correct simulation of near-wall viscous flow effects (boundary layer development, laminar turbulent transition etc.) a correct resolution of the airfoil boundary layer is mandatory. Otherwise, wall-functions would be used (instead of the desired turbulence model) whose accuracy is not sufficient for the designated aerodynamic and aeroacoustic investigation. An indicator for the correct mesh resolution in the boundary layer and the height of the first cell at the wall is the dimensionless wall distance y^+. It can be calculated from the wall shear stress τ_w, the fluid density ρ and the kinematic viscosity $\nu = \mu/\rho$ for a specific distance y.

$$y^+ = \frac{\sqrt{\frac{\tau_w}{\rho}}y}{\nu} \tag{3.1}$$

[3] An alternative strategy using a O-type grid topology, to account for finite TE thickness, was also developed. The basic concepts and dimension are the same, so that only the C-type meshing strategy is explained in this section. In the outer part of a wind turbine rotor blade it is always the aspiration to keep the trailing-edge thickness as thin as possible to avoid tonal blunt trailing-edge vortex shedding noise. The exact thickness value depends on the manufacturing and finishing process of the blade and is usually around 2-3 mm. As the main objective of this thesis is the simulation of broadband TBL-TE noise, the simulations are conducted with zero TE thickness. This hypothesis is valid, as long as no blunt TE noise according to Reference [4] occurs. The validity of neglecting a small trailing edge thickness on the radiated broadband spectrum of an airfoil slat was shown by Marcus Bauer[58]. Note, that the nature of the used hybrid CFD-CAA approach would (also with the O-grid topology and the consideration of finite TE thickness) not allow the simulation of blunt trailing-edge vortex shedding noise, as it relies on the time averaged (RANS) flow simulation where the vortex shedding would be suppressed.

An estimation of the height of the first cell at the wall $y = \Delta s_1$ can be done using the estimation for the smooth flat plate with turbulent boundary layer (see Schlichting[59]). It relates the skin friction coefficient (c_f) with the local Reynolds number Re_x based on empirical data:

$$c_f = 2\left(\frac{\kappa}{\ln Re_x} G\left(\ln Re_x\right)\right)^2 \quad . \tag{3.2}$$

With a von Kármán constant of $\kappa = 0.41$ and the function $G\left(\ln Re_x\right) \approx 1.5$ (according to [59]) c_f and from it $\tau_w = 1/2 c_f \rho v_\infty^2$ can be determined. Equation 3.1 can now be solved for $y = \Delta s_1$ with a desired dimensionless wall distance $y^+ = 1$ or below. For standard conditions ($\rho = 1.225\,\mathrm{kg/m^3}$ and $\mu = 1.79 \cdot 10^{-5}\,\mathrm{kg/ms}$) and a typical wind turbine airfoil Reynolds number between $3 \cdot 10^6$ and $6 \cdot 10^6$, the height Δs_1 lies between $6.6 \cdot 10^{-6}\,\mathrm{m}$ and $3.45 \cdot 10^{-6}\,\mathrm{m}$ (with a corresponding airfoil chord length of $l_c = 1\,\mathrm{m}$). A value of $\Delta s_1 = 3.0 \cdot 10^{-6}\,\mathrm{m}$ is chosen for all generated CFD meshes. This low value ensures y^+ values less than one for all typical Reynolds numbers and accounts for the uncertainties in the estimation procedure. Nevertheless, y^+ values need to be checked in the final simulation results.

The structured near-airfoil grid extends about 110 layers from the wall with an exponential growth factor of 1.1. Hence, a good resolution of the viscous sub-layer is realized and the numerical error is reduced. Moreover, the near airfoil blocks are distributed such, that almost perpendicular cells are generated at the airfoil wall. Therefore, the block corners are positioned with respect to the airfoil geometry by the `ICEM` replay script to account for changes of the geometry.

As an example, the CFD mesh for a 18 % thick DU-96-W-180[60] airfoil, normalized by the chord lengths l_c is depicted in Figure 3.3 (a). The structured region in the vicinity of the airfoil can be seen in detail (b) of Figure 3.3 and the high mesh resolution towards the wall (to resolve the boundary layer) can be seen in detail (c). The same blocking strategy and meshing procedure was used for all airfoils in this thesis.

To quantify the mesh quality the following indicators where extracted for the example DU-96 mesh using `ICEM CFD`:

- Maximum Aspect Ratio = 2250 (highest ratio for thin cells directly at the wall; low values are desired but not possible within the very thin boundary layer cells)
- Minimum Angle = 52.5 ° (minimum angle of cell internal faces; values should be at least greater than 20 ° for reasonable result quality)
- Maximum Angle = 126 ° (maximum angle of cell internal faces; values should be at least lower than 160 ° for reasonable result quality)
- Minimum Eriksson Skewness = 0.806 (empirical criterion in `ICEM CFD` to judge the element shear for a hexahedral element[4]; acceptable elements should have a skewness greater than 0.5)
- Maximum Volume Change = 1.15 (in the structured near airfoil region and 1.4 in the outer mesh region; ensures smooth increase in volume of neighboring cells; low values are desired)

[4] calculated by dividing the volume of its closest parallelepiped by the product of its edges (ranging between 1=perfect and 0=unacceptable)

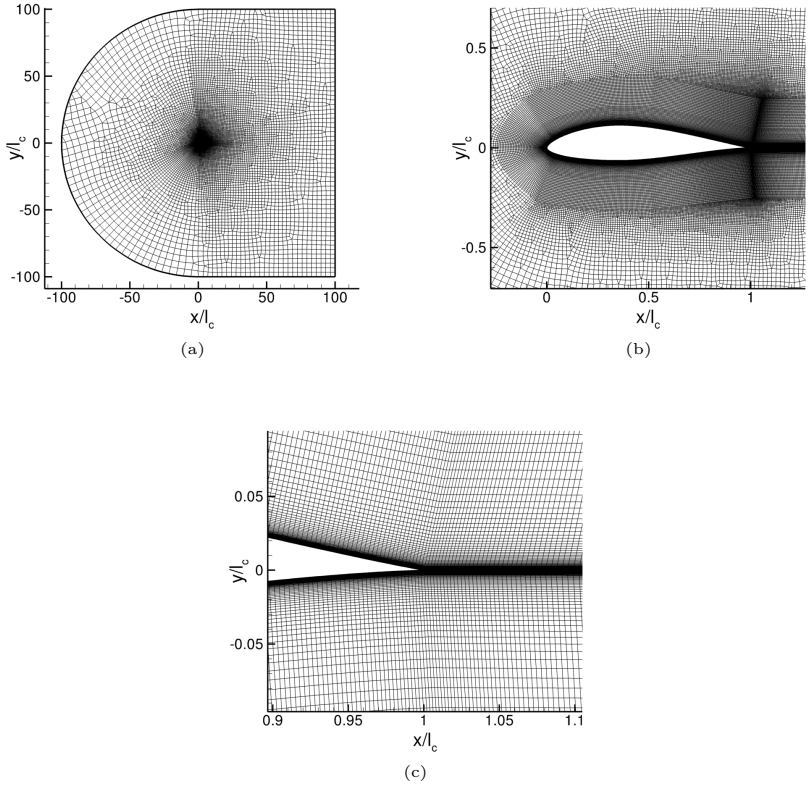

Figure 3.3: CFD mesh example for a DU-96-W-180 airfoil; (a) domain overview; (b) structured near airfoil region; (c) cells in the vicinity of the trailing-edge.

It is supposed, that the grid quality is maintained throughout the exchange of airfoil geometries. The reason for that is the automatic grid generation procedure realized by the `ICEM CFD` replay script. Herein the near-airfoil blocks are rearranged according to the geometry of suction and pressure side. Edges between surface blocks are always modified so, that they are perpendicular to the surface. Matching cell sizes and exponential growth factors are automatically set at block corners and along the edges to avoid discontinuities in the grid cell sizes. The high aspect ratio of the grid cells close to the wall - due the required low y^+ values - need to be accepted with regard to the total amount of mesh cells and the computational effort of the CFD simulation step.

For the automatic generation beside the airfoil geometry no further input is needed. The

new CFD mesh is created within a few seconds.

3.2.2 Boundary Conditions and Models

For the simulations the CFD code `TAU` is used. `TAU` can only process three-dimensional cases which makes it necessary to conduct the simulations in a quasi-two-dimensional procedure. Therefore the two-dimensional CFD mesh is extruded in the spanwise direction (z-direction) with the extent of only one cell. The resulting faces (normal vector in z-direction) are deemed as symmetry faces with the appropriate boundary conditions. A flow in spanwise direction is not possible. The simulation can be considered as two-dimensional. Figure 3.4 shows an overview of the computational domain and the relevant boundary conditions. Note, that there is no interface between the structured and unstructured volumes of the mesh. Instead, one-to-one nodal connections are used (hybrid mesh). `TAU` interprets the whole grid as unstructured. Even though, the high quality of the former structured mesh cells in the vicinity of the airfoil is necessary for the precise simulation of the viscous sub-layer and the flow phenomena present in the boundary layer.

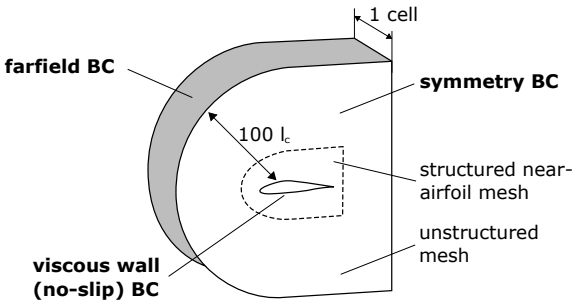

Figure 3.4: Sketch of the CFD domain; boundary conditions (BC) for the relevant faces are indicated in bold letters.

The following boundary conditions (BC) where used at the appropriate faces in the mesh:

- **Far-Field BC:** A far-field boundary condition is defined at the outer borders of the mesh ($100 l_c$ away from the airfoil). It acts as an inflow and outflow condition. All gradients are assumed to be zero and no viscous effects are taken into account. On the far-field BC the flow vector $\vec{v}_0$, with the magnitude $v_\infty = f\,(Re, l_c)$ and the angle of attack α relative to the airfoil chord, is defined.
- **Symmetry BC:** The symmetry boundary condition is used to model zero-shear slip walls at both spanwise borders of the domain. On these walls no viscous flow effects are present. Due to the mesh dimension of only one cell in spanwise direction only two-dimensional flow effects are captured. This quasi-two-dimensional flow can be interpreted as the flow around an unswept wing with infinite span.

- **Viscous Wall BC:** A wall with viscous effects is defined. That imposes a velocity directly at the wall of zero ($\vec{v}\,(y=0)=0$, no-slip condition) and a zero pressure gradient in wall normal direction ($\partial p/\partial y = 0$). Different types of transition treatment (turbulent, laminar, transition prediction or prescription) are distinguished and optional. Due to their strong influence on the airfoil performance different transition cases are analyzed. On the walls pressure forces and from them coefficients for lift, drag and momentum may be calculated.

All simulations are conducted under standard conditions for temperature and pressure ($p_{\mathrm{ref}} = 101325\,\mathrm{Pa}$, $T_{\mathrm{ref}} = 288.15\,\mathrm{K} = 15.0\,^{\circ}\mathrm{C}$). The angle of attack is varied by changing the velocity vector at the far-field boundary. Under normal wind turbine operation below rated power the local angle of attack of the rotor blade airfoils lies within the linear part of the lift curve (normally around its optimum value ($\alpha_{\mathrm{opt}} = \alpha\,(\max\,(c_L/c_D))$). For the simulations α is varied within this linear range (usually starting from $\alpha = 0\,^{\circ}$ up to the stall angle of attack α_{stall} (e.g. $14\,^{\circ}$ for a NACA0012 at the relevant blade chord Reynolds numbers)). The Reynolds number is chosen according to values present at the rotor blade section under operating conditions. It depends on the relative flow velocity of the blade section, its local chord length and the kinematic viscosity of the fluid (air at standard conditions: $\nu = 1.46 \cdot 10^{-5}\,\mathrm{m^2/s}$). Figure 3.5 depicts the local Reynolds numbers over the relative rotor radius (r/R) for the 126 m diameter NREL 5 MW reference turbine[61] and a state of the art 100 m 2.5 MW standard rotor. For each turbine the lower line shows the values at cut-in wind speed and the upper line the values for the wind speed of rated power (refer to Section 2.1.3). For the acoustically interesting outer third fraction of the rotor the Reynolds numbers are between $6 \cdot 10^6$ and $11 \cdot 10^6$ for the NREL turbine and $3 \cdot 10^6$ and $7 \cdot 10^6$ for the standard rotor.

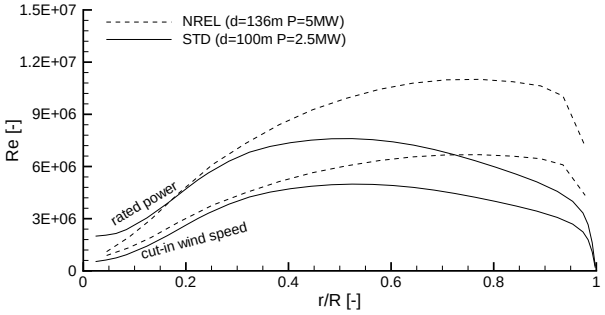

Figure 3.5: Distribution of the local Reynolds number for two different Rotor blades.

Note, that the relatively high Reynolds numbers of the NREL rotor are due to the chord length distribution of this blade. Chord lengths of more than 2 m even in the outer part of the rotor blade can be found. Modern blades are usually designed with shorter chords in order to achieve a lighter overall weight with a more slender design. Therefore, the values from the standard turbine are closer to reality. Throughout the simulations the focus is put on Reynolds numbers between $3 \cdot 10^6$ and $6 \cdot 10^6$.

The turbulence intensity of the incoming flow is an important setting in the simulation. Its default value is set to 0.03 % at the airfoil (similar to wind tunnel conditions). It can be varied by changing the turbulence intensity for the incoming flow (at the far-field boundary) and the eddy viscosity ratio μ/μ_t.

The two-equation SST-k-ω turbulence model as proposed by Menter[41] is used for the simulation of viscous effects and turbulence statistics. The analysis also includes cases with natural transition from laminar to turbulent boundary layer flow. The $\gamma - Re_\theta$ transition model[62] is used to capture this feature. Both models are implemented in the DLR flow solver `TAU`.

3.2.3 Grid Refinement Study

A grid refinement study is conducted to verify the independence of the simulated CFD results from the mesh resolution. In the sense of efficiency this is done only for two representative airfoils. A symmetric NACA0012 airfoil and a cambered NACA64618[5] airfoil were simulated on different computational meshes. The Reynolds number was set to $Re = 3 \cdot 10^6$, the angle of attack to $\alpha = 6\,^\circ$ and the boundary layer flow was treated as fully turbulent (no laminar running length). The total number of grid cells is doubled from one mesh to the next in order to use the uniform grid convergence reporting technique proposed by Roache [64]. The main focus was laid on the aerodynamic coefficients and their behavior for increasing mesh density. The results for four different meshes with a total number of cells ranging from ∼24k to ∼220k are shown in Table 3.1 for the NACA0012 airfoil and Table 3.2 for the NACA64618 airfoil.

Table 3.1: Results of grid convergence study for the NACA0012 airfoil; $Re = 3 \cdot 10^6$; $\alpha = 6\,^\circ$; transition: fully turbulent

mesh	N	c_L	Δc_L	c_D	Δc_D	c_M	Δc_M
N1	23960	0.652725		0.010999		-0.159016	
N2	52864	0.656851	0.63%	0.010694	-2.78%	-0.160425	0.89%
N3	110917	0.657931	0.16%	0.010691	-0.02%	-0.160871	0.28%
N4	220937	0.658966	0.16%	0.010689	-0.02%	-0.161303	0.27%

The coefficients are depicted in Figure 3.6 for both airfoils and an increasing number of total mesh cells N[6].

Both airfoils show almost no variations in the lift coefficient with finer meshes (see Figure 3.6 (a)). Even an increasing the number of cells from ∼110k to ∼220k results only

[5] In the NACA systematic the correct name of this airfoil would be NACA64$_3$618, where the subscripted 3 indicates the lift coefficient in tenths above and below the design lift in which favorable pressure gradients exist[63]. As this is unique for the 64$_3$618 airfoil only the short form NACA64618 without the subscript will be used.

[6] The total number of cells is mainly influenced by the number of cells within the structured region of the mesh. For the generation of finer meshes the density in the structured region is increased. Thus, more layers are distributed along the boundary layer and near airfoil region. Moreover, the number of grid points along the upper and lower side of the airfoil is increased. The refinements within the unstructured domain directly resulted from the increased number of nodes on the transition surface between the two regions.

Table 3.2: Results of grid convergence study for the NACA64618 airfoil; $Re = 3 \cdot 10^6$; $\alpha = 6\,°$; transition: fully turbulent

mesh	N	c_L	Δc_L	c_D	Δc_D	c_M	Δc_M
N1	23391	1.089958		0.014982		-0.38325	
N2	50560	1.092741	0.26%	0.014723	-1.73%	-0.38429	0.27%
N3	105180	1.097548	0.44%	0.014598	-0.85%	-0.38623	0.51%
N4	208674	1.100856	0.30%	0.014576	-0.15%	-0.38768	0.38%

in a minor change in c_L from one mesh to the other (0.16 % NACA0012 and 0.30 % NACA64618). The c_D values show a stronger dependence on the mesh resolution, especially for coarser meshes (see Figure 3.6 (b)). This is due to the need of a finer resolution within the boundary layer. Again, when the resolution is fine enough, the doubling of the mesh cells from the N3 to N4 mesh has only minor influence on the c_D values (-0.02 % NACA0012 and -0.15 %). The pitching moment coefficient c_M shows the same behavior as the lift coefficient.

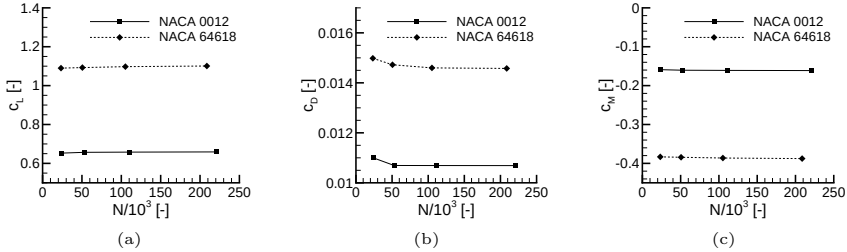

Figure 3.6: CFD grid refinement study showing dependence of aerodynamic coefficients on increasing mesh resolution; (a) lift coefficient c_L; (b) drag coefficient c_D; (c) pitching moment coefficient c_M.

It is argued, that the independence of these two airfoils from the mesh resolution with the chosen N3 mesh holds for all other airfoils within the investigation, as the main geometry is still of an airfoil type and thereby only 'minor' changes occur. Thus, for the further process of the simulations the N3 mesh configuration is chosen and implemented in the automatic mesh generation procedure. Details on this can be found in Section 3.2.1.

For a uniform reporting of grid refinement studies, Roache [64] proposed the use of the grid convergence index (GCI) which is based on the generalization of the Richardson Extrapolation. For the coarser mesh (in this case N3 in comparison with N4) it is defined as:

$$GCI = 3r^p \left|\epsilon\right| \left(r^p - 1\right) \ . \tag{3.3}$$

Herein $\epsilon = \left(f_2 - f_1\right) / f_1$ represents an error estimator based on the actual grid solution f_1 and the solution of the coarser grid f_2 (analogous to the Δc_i values given in Table 3.1 and

Table 3.2). The theoretical order of convergence is indicated by p (estimated with $p = 2$ for the present study) and the grid refinement ratio by r ($r = 1.41$ for present study). This results in the following GCI values for the chosen coarser N3 grids in comparison with the finer (more accurate) N4 ones (see Table 3.3).

Table 3.3: NACA0012 and NACAC64618 GCI values for N3 grids

Airfoil	$GCI\ c_L$	$GCI\ c_D$	$GCI\ c_{M25}$
NACA0012	0.95%	0.14%	1.62%
NACA64618	1.82%	0.89%	2.27%

It can be seen from the values that the simulated coefficients can be considered accurate within the range of 1-2 %. It also needs to be said, that the constant factor 3 in Equation 3.3 represents a judgment call from Roache, which is possibly too conservative[64]. The actual GCI value might therefore be lower and the accuracy higher.

Another important fact to consider is the boundary resolution of the mesh. It should be fine enough to fulfill the y^+-criteria ($y^+ < 1$). Figure 3.7 depicts the calculated y^+-distribution over the suction and pressure side for a NACA0012 (a) and a NACA64618 (b) airfoil at a Reynolds number of $Re = 3 \cdot 10^6$ and an angle of attack of $\alpha = 6\,^\circ$. A fully turbulent boundary layer was enforced by the appropriate setting in the CFD simulation (no laminar running length). According to the graph, y^+ values smaller than one are achieved throughout the whole airfoil surface on both sides. The estimation of the height of the first cell near the walls holds in this case and still bears enough reserve for higher Reynolds numbers.

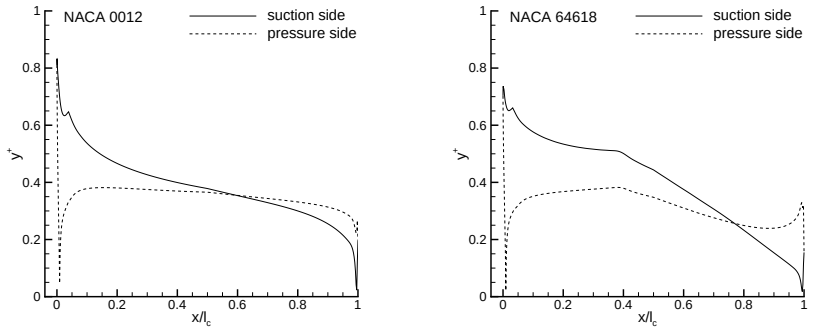

Figure 3.7: Dimensionless wall distance y^+ at $Re = 3 \cdot 10^6$, $\alpha = 6\,^\circ$, fully turbulent boundary layer; (a) NACA0012 airfoil; (b) NACA64618 airfoil.

3.2.4 Validation

Finally the results from the CFD simulations are juxtaposed to measurement data obtained from Abott [63]. The results for lift and drag coefficients for three different angles of attack ($\alpha = 0\,°, 3\,°, 6\,°$) for the two airfoils are depicted by the symbols in Figure 3.8. The experimental data is shown by the solid and dashed graphs.

A good agreement for the numerically predicted lift coefficient can be seen in Figure 3.8 (a) for both airfoils. The simulated values nearly match the experimental data. For the lift coefficient (Figure 3.8 (b)) an underprediction of the values in the CFD simulation can be observed. The error increases with higher α and is also more pronounced for the symmetric NACA0012 airfoil. Nevertheless, the trend of the measurement data can be seen from the numerical results. One reason for the deviation of the values might be treatment of the laminar turbulent transition in the measurements. To achieve a fully turbulent BL flow a standard roughness was applied to the surface. This was done in the form of carborundum grains applied to the first 8 % of the airfoil's chord on both sides [63]. This heavy roughness might lead to the higher drag values in comparison with the smooth surface (with only tripped boundary layer at the leading-edge) assumed in the CFD simulations.

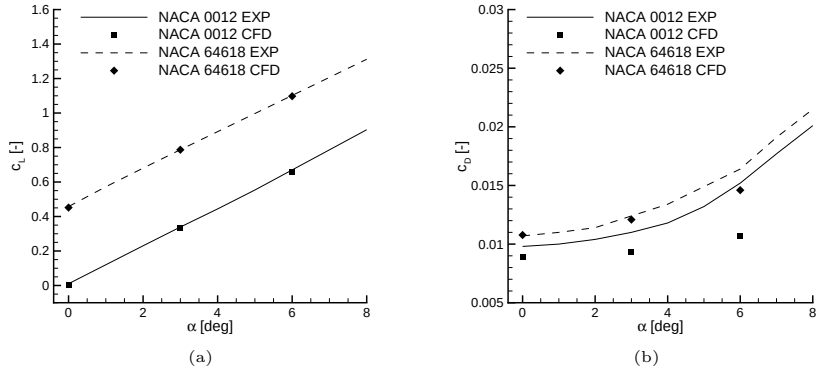

Figure 3.8: Comparison of CFD results on chosen N3 mesh with experimental data from [63]; $Re = 3 \cdot 10^6$; (a) lift coefficient c_L; (b) drag coefficient c_D.

A more precise validation of the CFD results from the toolchain can be found in Section 4.1 were a closer look is also taken on the boundary layer data which builds the basis for the subsequent aeroacoustic simulation steps.

3.3 CAA with FRPM

The numerical simulation of trailing-edge noise is done using a two-dimensional computational aeroacoustics (CAA) simulation. Therefore the DLR code `PIANO` (acronym for Perturbation Investigation of Aerodynamic Noise) is used. Figure 3.9 illustrates the workflow. Based on the airfoil geometry (which was already used to create the CFD mesh)

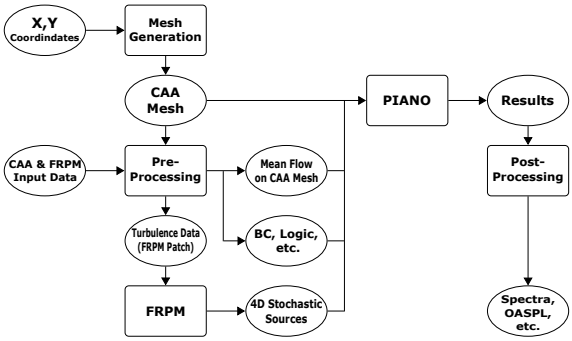

Figure 3.9: Schematic toolchain showing the consecutive steps for the CAA simulation.

a CAA mesh for the acoustic domain is generated. This block-structured grid differs in terms of meshing strategy and used resolution from the CFD grid in order to fulfill the acoustic criteria (for details refer to Section 3.3.1). For the simulation a logic file is needed in which the topology of the mesh and the boundary conditions (e.g. solid wall, inner cut, far-field radiation condition) are prescribed. Besides that, some more files need to be generated in the pre-processing step to yield all necessary inputs for the `PIANO` solver. The so-called mean-flow field is extracted from the CFD results. It is composed of the flow vector $\vec{v}$, the static pressure p and the density ρ. All values are non-dimensionalized by corresponding reference values (see Equation 2.35). Thereafter, they are interpolated from the CFD mesh onto the CAA mesh by the DLR tool `UGINT`.

As the acoustic simulation is done in the time domain, fluctuating, time-resolved turbulence information are needed to calculate the sound sources. This is done by the Fast Random Particle Mesh method (FRPM)[55]. Therefore the turbulence statistics (turbulence kinetic energy k_t and the specific dissipation ω) are extracted from the CFD results within a desired source region. This region (where the fluctuating and convecting turbulent eddies are reconstructed) is called the FRPM patch. A nondimensionalization (refer to Equation 2.35) and a calculation of the turbulence length scale on the patch (refer to Equation 2.60) is also done within the pre-processing step.

After all input data is gathered, the acoustic simulation with `PIANO` can be started. Considering the unsteady simulation in the time domain, the overall computation time depends on the period of real time which should be investigated. The traveling speed of the emerging sound waves, the mesh resolution and the overall extend of the acoustic domain need to be taken into account to determine the transient phase of the simulation, beyond which the data sampling may be started. Unsteady simulations usually

produce a lot of data throughout the simulation process. For efficiency reasons, time resolved fluctuations are only stored at prescribed points in the domain. These points are called virtual microphones. The microphone signals are analyzed in the post-processing step. Spectra (narrow, octave or third-octave band) can be derived by means of a fast Fourier transformation (FFT). Overall sound pressure levels ($L_{p,OA}$ or OASPL) can be calculated and directivities of the sound source can be determined by the use of multiple microphones. For visualization of the sound field snapshots or movie sequences of the fluctuating sound pressure field can be stored.

The usual computation time on standard hardware (6 CPU machine) is less than 20 hours to achieve an acoustic solution for one set of input parameters. As the CFD simulations are much faster (refer to Section 3.2), multiple CAA simulations were done simultaneous on a high performance cluster (DLR case cluster in Braunschweig) to counteract the time lag of the acoustic simulation for the calculation of angle of attack (acoustic) polar curves.

3.3.1 Mesh

The spatial discretization of the acoustic domain is realized with a structured multi-block mesh. The requirement of this mesh type comes from the solver `PIANO` as it can only process structured grids[7]. To calculate the needed derivatives with the 4th order DRP scheme, in the explicit solving process of the perturbation equations (refer to Section 2.3.4), a high quality mesh is required. It is generated within the acoustic domain which extends six by six chord lengths. The airfoil trailing-edge (the main noise source in this simulation) is centered in the middle. Figure 3.10 depicts the geometrical extends. The FRPM patch area is indicated by the gray rectangle at the trailing-edge. It extends $0.4\,l_c$ in the chordwise direction and approximately $0.1\,l_c$ in height (depending on the airfoil and boundary layer thickness). The CAA mesh consists of 64 blocks with a total number of approximately 1.1 million cells. It was created using the commercial grid generator `POINTWISE`[8]. The overlaying FRPM patch is built from one block with equidistant distributed squared cells (more details in Section 3.3.3).

In contrast to the CFD domain, the CAA domain is much smaller. This has two reasons. First, the sound waves emerging from the trailing-edge are moving out of the domain and the far-field boundaries are set as non-reflective. Due to that no interference of the actual solution with the far-field boundary condition is assumed[9]. The second reason is the high resolution of the CAA mesh (to account for the correct resolution of the acoustic waves)

[7] For more complex geometries this may be a disadvantage, as the grid generation process can be very complex. Whereas, for two-dimensional airfoil grids the meshing can still be done in reasonable time and with reasonable effort. Moreover, the structured approach can be automized, which (correctly done) guarantees a high level of constant quality. To overcome the gap of the structured mesh requirement, the acoustic solver DISCO based on the discontinuous Galerkin method was developed at DLR [65–67]. Still, `PIANO` was used for this investigation because the mesh generation was no severe problem for the two-dimensional airfoils. Furthermore, the parallelization of `PIANO` pledges a better performance in terms of computational times. For parallelization, sets of blocks can be distributed to different CPUs and solved there individually.

[8] In a later stage of the project an alternative meshing (using the same strategy as described) was also realized with the grid generator `ICEM CFD`.

[9] In contrast to CFD where a precise flow vector is set at the opening boundary condition, which clearly differs from the flow vector in the vicinity of the airfoil and as such would interfere with the solution and yield a non-physical result.

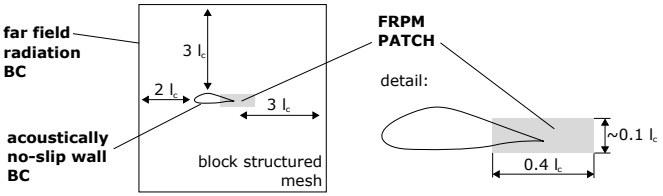

Figure 3.10: Schematic domain for the CAA simulation with FRPM patch shown in detail.

which leads to a high total number of cells. In favor of efficiency the mesh was kept at small as needed.

CAA meshes have a nearly uniform cell density in the far-field region to resolve the acoustic waves. A coarsening towards the outer boundaries beyond a minimum resolution is not reasonable. The minimum wave length (maximum frequency $f_{\max}$) has to be resolved with a resolution of seven points per wave-length (refer to Equation 2.47 in Section 2.3.5). The minimum far-field grid spacing $\Delta x_{\mathrm{i,min,ff}}$ can thus be calculated to:

$$\Delta x_{\mathrm{i,min,ff}} = \frac{1}{7} \cdot \frac{c_\infty}{f_{\max}} \ . \tag{3.4}$$

The used standard mesh can resolve frequencies up to maximum frequency of $f_{\max} = 5\,\mathrm{kHz}$ with a reference chord length of $l_c = 1\,\mathrm{m}$. The minim cell size in the far-field is $\Delta x_{\mathrm{i,min,ff}} = 0.01 x_i / l_c$. For an evaluation of the TBL-TEN peak frequency the estimation of Brooks, Pope and Marcolini[3] can be used:

$$St_{\mathrm{peak}} = 0.02 M^{-0.06} \ . \tag{3.5}$$

Herein St_{peak} represents the peak Strouhal number of the problem and M stands for the free stream Mach number. The peak frequency can be calculated as:

$$f_{\mathrm{peak}} = \frac{St_{\mathrm{peak}} \delta^*}{u_\infty} \ . \tag{3.6}$$

As a first estimation the turbulent boundary layer thickness δ of a flat plate can be used:

$$\delta = \frac{0.37 x}{Re(x)^{1/5}} \ . \tag{3.7}$$

Together with the assumption[68], that the boundary layer displacement thickness δ^* is 30 % of boundary layer thickness δ, this yields a peak frequency of $f_{\mathrm{peak}} \approx 450\,\mathrm{Hz}$ which is well below the resolved maximum frequency of $f_{\max} = 5\,\mathrm{kHz}$. For the airfoils under investigation, the adverse pressure gradient due to the surface curvature and inflow angle of attack, is supposed to lead to even thicker boundary layers at the trailing-edge resulting in decreased peak frequencies. Thus, the upper limit resolution of $f_{\max} = 5\,\mathrm{kHz}$ is still reasonable to capture nearly all parts of the resulting TBL-TEN spectrum. Note, that the peak frequency as well as the maximum resolvable grid frequency scale with the desired airfoil chord length. Thus, a decrease in chord length would result in a higher

peak frequency and also in a higher resolvable frequency. Consequently no mesh adaption is required if the absolute chord length is changed.

For the simulations with the FRPM method, the CAA mesh must have the same resolution as the FRPM source patch within the patch region. The resolution of the patch is determined by the smallest turbulent eddy size which should be reconstructed (for details see Section 3.3.3). For the trailing-edge noise problem, this resolution is usually way below the far-field resolution(e.g. $\Delta x_{\mathrm{i,min,patch}} = 0.0005 x_i/l_c$ which represents a size reduction by the factor 20). This leads to the difficulty that a much finer resolution occurs within the trailing-edge region (FRPM patch region) of the CAA mesh. If all the mesh would be resolved with this fine resolution, the total number of cells would get unacceptably high. This would either lead to a higher number of CPUs for the parallelization or simply to longer computational times. To counteract this, a meshing strategy is used, where the increase of cell numbers (and thereby the decrease of cell sizes) within a certain region around the trailing-edge is possible without interfering too strong with other parts of the block-structured mesh. Therefore, a so-called clamping grid will be used, where an O-type mesh runs around the trailing-edge. This strategy makes it possible to stretch the dense cells directly at the trailing-edge source region towards the outer parts of the mesh. Moreover the number of cells within the O-grid can directly be controlled without influence on other parts of the CAA mesh. The O-grid disembogues in a C-type grid around the airfoil nose which is further embedded in a H-grid topology towards the outer boundaries. Figure 3.11 shows an exemplary CAA mesh for a DU-96-W-180 airfoil created with the prescribed strategy. An overview of the acoustic domain is shown in Figure 3.11 (a). The trailing-edge region, the clamping meshing approach and the overlying FRPM patch (indicated in red) are shown in (b). A detailed view of the TE region can be seen in (c). Note, that due to visualization issues only every tenth grid line is shown in these plots.

The clamping CAA grid strategy allows it to keep the overall amount of cells within reasonable and feasible limits. Due to the rather large ratio of the different cell sizes a denser mesh region above and below the trailing-edge remains. A smooth transition between different cell sizes with an exponential growth factor of 1.1 is enforced. Further distortion of the cells towards the outside region is avoided to keep the internal cell angles as close to 90 ° as possible. Still, a very high grid quality is achieved which is mandatory for good aeroacoustic results. Finally, a smoothing algorithm is used to improve the blending between different cell sizes and angles, especially at the internal block intersections.

To quantify the mesh quality the following indicators are extracted from the example DU-96 mesh using `ICEM CFD`:

- Maximum Aspect Ratio = 21.9 (highest ratio for thin cells in the dense area above and below the TE towards the far-field)
- Minimum Angle = 39.5 ° (minimum angle of cell internal faces)
- Maximum Angle = 144.9 ° (maximum angle of cell internal faces)
- Minimum Eriksson Skewness = 0.638 (empirical criterion in `ICEM CFD` to judge the element shear for a hexahedral element (see Footnote 4))
- Maximum Volume Change = 1.15 in the structured near airfoil region and 1.4 in the outer mesh region (ensures smooth increase in volume of neighboring cells)

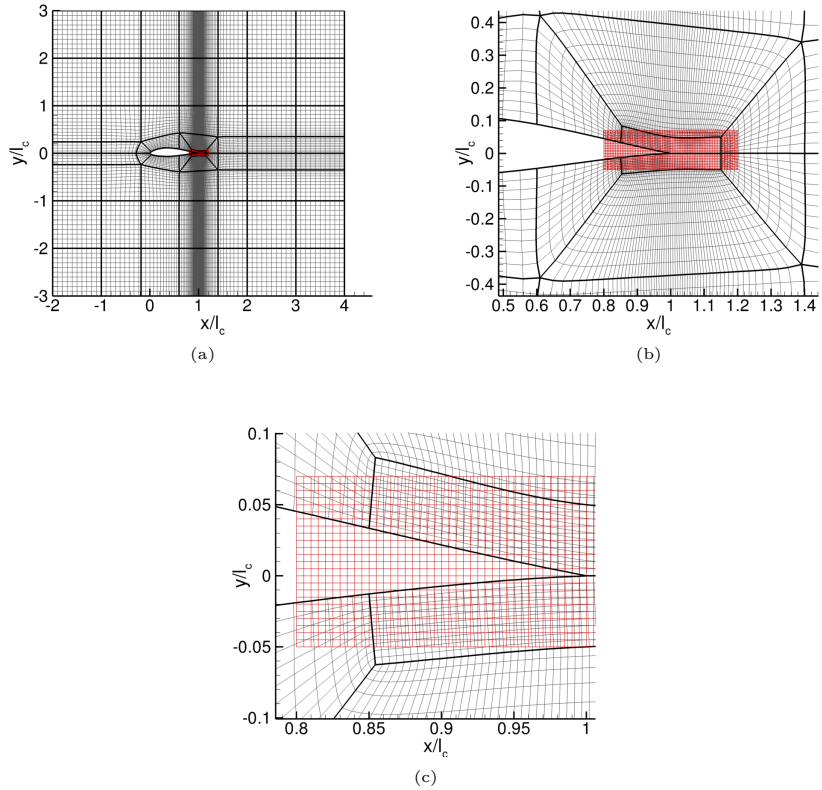

Figure 3.11: CAA mesh example for a DU-96-W-180 with FRPM source patch mesh (shown in red) - for better visualization only every tenth grid line is shown; (a) domain overview; (b) blocks in TE vicinity (clamping) with FRPM patch; (c) matching resolutions of CAA mesh and FRPM patch.

Similar to the preparation of the CFD grid an automation strategy relying on replay scripts was developed for the CAA meshes. Beside the fast generation of acoustic grids for new airfoil geometries it ensures a consistent mesh quality throughout arbitrary airfoil geometries.

3.3.2 Boundary Conditions and Models

The DLR in-house acoustic code PIANO is used for the acoustic simulations in the time domain. Therefore, a correct setting of the non-dimensional time step Δt is mandatory. The reference length l_{ref} (usually the airfoil chord length l_c) as well as the ambient speed of sound c_∞ need to be considered (* indicated quantity with dimension):

$$t = t^* \cdot \frac{c_\infty}{l_{\text{ref}}} \ . \tag{3.8}$$

A non-dimensional time step of $\Delta t = 2 \cdot 10^{-4}$ is used for the simulations. Under standard conditions and with a reference length of $l_{\text{ref}} = 1\,\text{m}$ this represents a time step of $5.88 \cdot 10^{-7}\,\text{s}$. A total number of 400000 time steps is conducted for each simulation resulting in an overall physical sampling time of 0.235 s. The small time step size is the result of the fulfillment of the Courant–Friedrichs–Lewy (CFL) condition which states, that the time step must be chosen in accordance to the traveling speed of the information and the spacial distance between two neighboring points in the computational grid. Sampling data is recorded on a microphone circle with 360 equidistantly distributed microphones and a radius of $r = 2.5 l_c$. The sampling rate is set to every 50th time step (real time sampling interval of $\Delta t^* = 2.94 \cdot 10^{-5}\,\text{s}$) which corresponds to a detectable Nyquist frequency of $f \approx 17\,\text{kHz}$ and is still above the maximum resolvable frequency of the used CAA mesh ($f_{\max} = 5\,\text{kHz}$).

The APE-4 equation system as shown in Equation 2.42 and 2.43 in Section 2.3.4 is used for the computations.

The following boundary conditions are set at the appropriate faces in the mesh (refer to Figure 3.10):

- **Far-Field Radiation BC:** A non-reflective far-field radiation condition according to Tam and Webb [45] is set at the outer edges of the CAA domain. Acoustic waves which are traveling towards these edges are not reflected. The solution is similar to an infinitely extended domain.
- **Acoustically no-slip Wall BC:** The airfoil's upper and lower side are set as acoustically no-slip walls according to Tam and Dong [69]. Directly at the wall the acoustic velocity in wall normal direction is zero ($v'_n = 0$). The boundary conditions is realized by a ghost point for the pressure beyond the wall and the fulfillment of the non-penetration condition.
- **Inner Cut BC:** Intersections of blocks within the computational domain are set as inner cuts. Thus, transmission of acoustic waves across the CAA grid and the block edges is possible.

The setting of the boundary conditions is done via flags in the logic file which corresponds to the CAA grid. Block numbers and the correct numbering of the edges need to be considered. The logic file is derived from the CAA mesh using the tool DLR tool LOGIC.

For a stable solution a global damping is applied to the simulation enforcing the so called the artificial selective damping (see Reference [69]). The very short wave lengths of signals which can not be represented physically correct are suppressed by this to avoid artificial noise within the simulation. For the airfoil trailing-edge noise simulations, the use of a

global damping factor in combination with Gaussian-shape damping spots, located at the leading and trailing-edge of the airfoil, have proven to be successful.

All global settings for the simulation are controlled from the `PIANO` input file. Herein, the required files for the CAA grid, the CAA grid logic, the mean flow data interpolated onto the CAA mesh, the CPU distribution used for parallelization of the computations and the FRPM patch are specified with their respective paths. Moreover, the global simulation parameters (e.g. total number of time steps) and the wanted output data parameters are set within this file. An additional section also controls the FRPM turbulence reconstruction and the used parameters for it. To remedy errors the input file is created automatically by a script. An example can be found in Appendix A.5.

3.3.3 FRPM

The turbulence reconstruction from the time averaged turbulence statistics is done with the FRPM method. It is thereby sufficient to reconstruct the turbulence within the patch area around the trailing-edge to simulate the TBL-TEN noise mechanism. The FRPM mesh size and the total number of cells within the patch account for the numerical effort in the simulation process. The FRPM calculations are processed solely by one CPU.

For all test cases a 800 by 200 cells source patch with quadratic cells and the dimensions $x/l_c = 0.4$ by $y/l_c = 0.1$ is used. It is indicated in red in Fig. 3.11 (c). The patch is centered at the trailing-edge. For airfoils with a higher relative thickness (t/l_c) the extension in y-direction is adjusted, e.g. $y/l_c = 0.12$ with 240 cells.

Besides the mean flow velocity vector $\vec{v_0}$ the patch contains the turbulence kinetic energy k_t as the variance and the turbulent length scale l as a size measurement of the reconstructed eddies. All values are extracted from the previously conducted RANS simulation and non-dimensionalized according to Equation 2.35. Additionally, a weighting function $w(\vec{x})$ as indicated in Equation 2.58 is set as a variable on the patch. This weighting function ramps the source strength towards 100 % at the trailing-edge ($x/l_c = 1$). A smooth ramping is thereby crucial for the avoidance of artificial noise sources (see Reference [70])

As an example the patch of a NACA0012 airfoil ($\alpha = 0\,^\circ$, $Re = 1.5 \cdot 10^6$, $M = 0.1664$) is shown in Figure 3.12. The trailing-edge is situated at $x/l_c = 1$ and $y/l_c = 0$. The mean flow velocity in x-direction v_x is shown in (a). Low values directly at the wall are due to the reduced flow velocity in the viscous boundary layer of the airfoil. Figure 3.12 (b) indicates the turbulence kinetic energy k_t extracted from turbulence statistics of the RANS solution. The highest values can be found slightly above the airfoil surface. The length scale l according to Equation 2.60 can be seen in (c). Larger turbulent structures can be found behind the trailing-edge, especially where the boundary layers of upper and lower side are moving closer together ($x/l_c > 1.1$). The weighting function which is responsible for the smooth ramping of the source strength towards 100 % is depicted in (d). All these parameters are input values for the FRPM calculation.

A snapshot of the result, the time resolved turbulence field, can be seen in Figure 3.12 (e). Here the vorticity calculated by FRPM for a certain time step is shown. Different sizes of turbulent eddies with different orientations and magnitudes can be seen. If again, the temporal average of the turbulence kinetic energy is computed for the time resolved

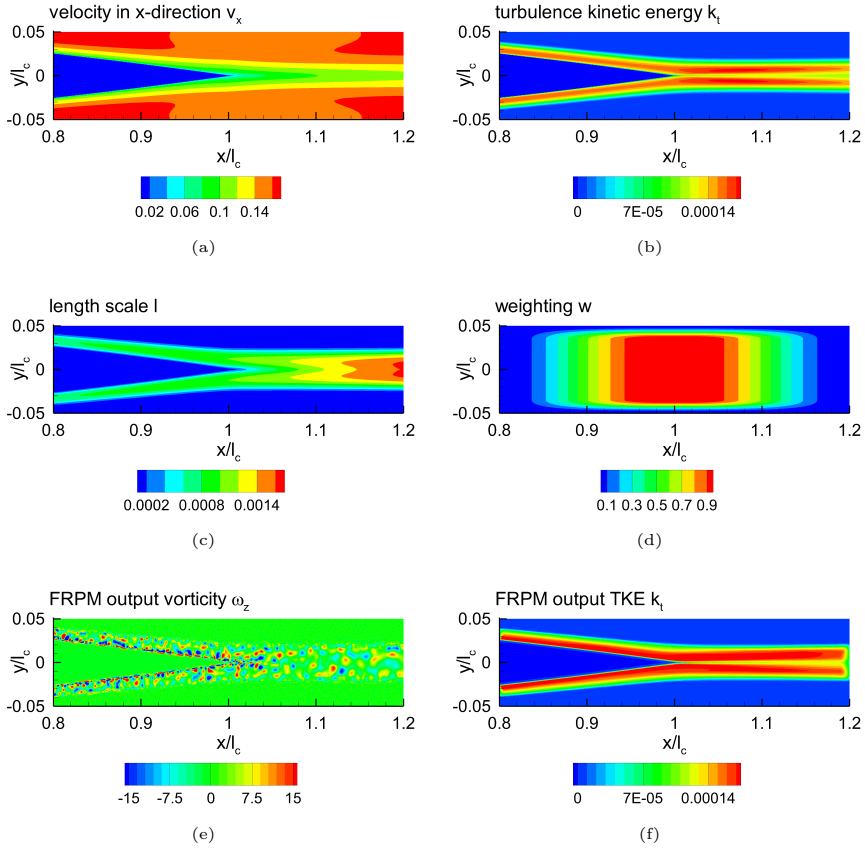

Figure 3.12: FRPM patch example (NACA0012, $\alpha = 0\,°$, $Re = 1.5 \cdot 10^6$, $M = 0.1664$, $l_c = 0.4\,\mathrm{m}$) with the respective (non-dimensional) variables: (a) velocity; (b) input turbulence kinetic energy; (c) length scale; (d) weighting; (e) snapshot of FRPM output vorticity; (d) FRPM output of time averaged TKE.

reconstructed turbulence, the result depicted in Figure 3.12 (f) can be produced. Comparing Figure 3.12 (f) (FRPM result) with Figure 3.12 (b) (FRPM input), the precise reconstruction ability of FRPM can be seen. The reconstructed statistics are almost equal to the input values. This can also be seen in the more detailed plots of Figure 3.13. Here, the turbulence kinetic energy distribution along a chord-perpendicular line for input and reconstructed TKE values is depicted. Figure 3.13 (a) shows the comparison directly at the trailing-edge ($x/l_c = 1.00$) while the position behind the trailing-edge ($x/l_c = 1.05$)

is shown in Figure 3.13 (b). The dashed line indicates the input TKE data (as extracted from the RANS calculation). The solid line represents the time averaged TKE distribution obtained from FRPM after 400000 time steps. Directly at the trailing-edge and close to the wall (small absolute y/l_c values), an overshoot of the reconstructed TKE can be observed. Further downstream this overshoot diminishes and the values are nearly identical.

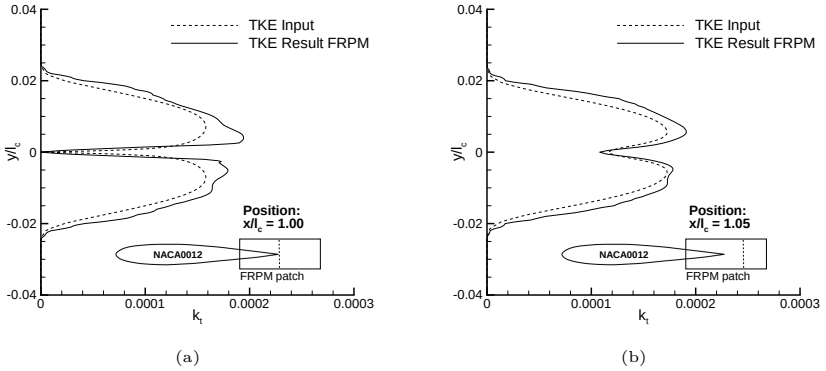

Figure 3.13: Comparison of input TKE to time averaged FRPM result along a vertical line (y-direction) (NACA0012, $\alpha = 0\,^\circ$, $Re = 1.5 \cdot 10^6$, $M = 0.1664$, $l_c = 0.4\,\mathrm{m}$): (a) directly at the trailing-edge at $x/l_c = 1.00$ and (b) behind the trailing-edge at $x/l_c = 1.05$.

It is shown in Reference [70], that the overshoot at the wall is influenced by the minimum resolved length scale $l_{\min}$, below which length scale values are automatically set to the value of $l_{\min}$. This results in a kink in the length scale distribution which has to be smoothed in order to calculate the correct derivatives in the FRPM procedure. This length scale trimming and smoothing was implemented into the used `PIANO` version. The result is a slightly smoother TKE distribution. Even with this procedure, the TKE overshooting of around 5-10 % close to the wall could not be remedied. It has to be considered in the error analysis of the results and might be remedied by the common off-set calibration of all CAA simulations suggested in Reference [70].

Another important finding in Reference [70] is the influence of the weighting function $w(\vec{x})$. It was found out that different spatial weighting functions produce different amounts of artificial noise. It can be shown, that this noise can directly be linked to the form of the weighting function. Thereby the dependence is mainly in x direction, as particles convecting through the patch are mainly moving in this direction for small angles of attack.

Figure 3.14 (a) shows two representative weighting functions $w_A(x)$ and $w_B(x)$ (indicated by the square symbols) . Function A shows a linear ramping towards $w(x) = 1$ with a

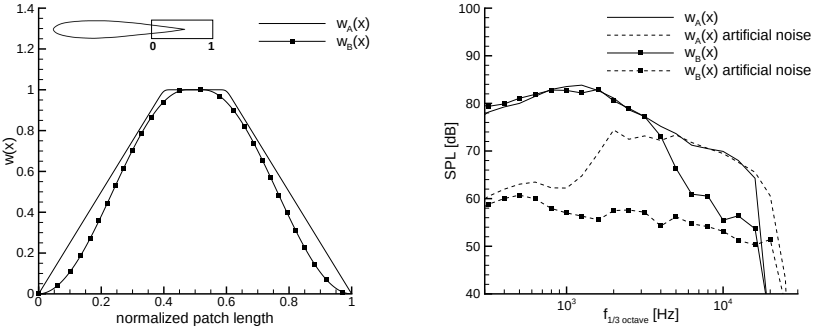

(a) (b)

Figure 3.14: Influence of the used weighting function $w(\vec{x})$ on the artificially created noise from FRPM (NACA0012, $\alpha = 0\,^\circ$, $Re = 1.5 \cdot 10^6$, $M = 0.1664$, $l_c = 0.4\,\mathrm{m}$): (a) different spatial weighting functions; (b) simulated broadband noise spectra directly below the trailing-edge at the distance $y/l_c = 1$ and the artificial noise produced by the weighting itself.

smoothed transition onto the middle plateau. Function B has been shaped like a $\sin^2(x)$-function[10]. Thus it has a zero gradient towards the beginning and end of the patch and also towards the middle plateau. Both patches are used on a NACA0012 test case. The resulting broadband spectra for the one-third-octave band sound pressure levels (SPL or L_p) are shown in Fig. 3.14 (b). The dashed lines indicate the amount of artificial noise. These values were calculated by introducing the patch to a CAA mesh with a constant cell distribution and no airfoil present. Thus, the resulting spectra is purely influenced by artificial noise, because the movement of the turbulent eddies without an edge present is supposed to radiate much less noise than in the case with the edge[9]. It can be seen that for the linear weighting the spectrum is dominated by spurious noise above a frequency of 5 kHz. Consequently this part of the spectra does not represent broadband trailing-edge noise and is of purely artificial nature. The rapid ramping at the beginning and the end of the patch seems to ramp up not fully developed vortices and thereby causes the high frequency noise. In contrast to that, the smoother $sin^2(x)$-function shows a better behavior. The artificial noise of the patch is 20 dB below the TBL-TE noise up to a frequency of 5 kHz. Above that frequency the trailing-edge signal decreases, reducing the threshold to approximately 5 dB. Even in this range the artificial noise is still below the target signal. Thus, it is recommended to use a weighting function similar to $w_B(x)$ to keep the contamination with artificial noise produced by the source term weighting to a minimum. This kind of function is used for all simulations conducted throughout this thesis.

Beside the influence of the FRPM weighting function, the effect of different length scale

[10] For the precise description of this function refer to the FRPM requirements from Section 3.3.5

factors l_{fac} is analyzed. According to Equation 2.60 a scaling of the turbulence length scale realized by FRPM is done via l_{fac} which results from the model constants of the RANS turbulence model and should be approximately $l_{\text{fac}} \approx 6.0$ (see Section 2.3.6). Nevertheless, the empirically determined constants of the turbulence model leave some room for interpretation. The plots in Figure 3.15 reveal the influence of different values of l_{fac} on the realized time averaged turbulence kinetic energy (a) and the resulting one-third-octave band spectra (b).

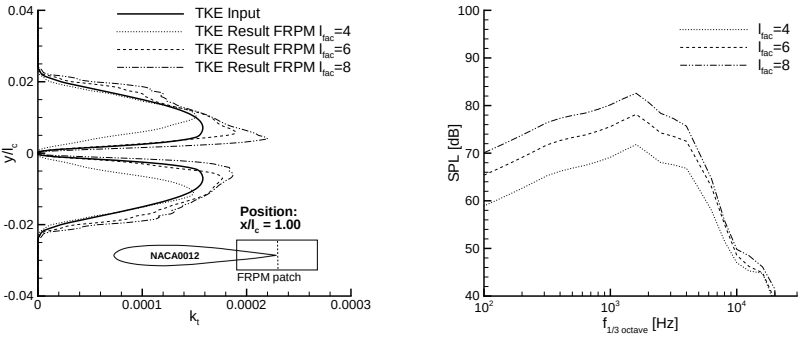

Figure 3.15: Influence of the used length scale factor l_{fac} (NACA0012, $\alpha = 0\,^{\circ}$, $Re = 1.5 \cdot 10^6$, $M = 0.1664$, $l_c = 0.4\,\text{m}$): (a) on the resulting time averaged TKE from FRPM along a vertical line directly at the trailing-edge ($x/l_c = 1.00$); (b) simulated broadband noise spectra directly below the trailing-edge at the distance $y/l_c = 1$.

In Figure 3.15 (a) it can be seen, that the target TKE distribution (FRPM input - solid line) is under-predicted with the low l_{fac} value of $l_{\text{fac}} = 4$. Especially close to the wall (at small absolute y/l_c values in the range of $|y/l_c| < 0.1$) a very strong deviation can be observed. The maximum TKE value on upper and lower side is slightly underestimated and its position is too far away from the walls on both sides. Increasing the length scale factor to $l_{\text{fac}} = 6$ results in a better coincidence of input and realized TKE value in the near wall region, while the maximum value is slightly over-predicted. Still, the distance of the maximum from the trailing-edge agrees with the input data. Further increase of l_{fac} to $l_{\text{fac}} = 8$ results in an over-prediction of TKE values in the near-wall region, while the maximum TKE is still increased. Looking on the related far-field noise spectra for the three different l_{fac} settings depicted in Figure 3.15 (b), the influence on the one-third-octave band levels can be seen. The peak level of each spectrum stays at the same frequency of about 1.5 kHz, while there is a severe influence on the slope of the decaying spectra and the SPL values. The higher the value of l_{fac} is chosen, the steeper is the slope and the higher are the absolute SPL values. For the following CAA airfoil simulations a value of $l_{\text{fac}} = 6$ is chosen, as this value matches the quotient of the underlying turbulence model constants ($l_{\text{fac}} = \frac{c_l}{C_\mu}$ with $C_\mu = 0.09$ and $c_l \approx 0.54$) and shows the best results

in turbulence statistics reconstruction. Also, a good agreement of the resulting far-field spectrum with experimental data could be achieved with this value (for details refer to Section 4.1).

In Reference [70] the problem of a too steep decrease of the far-field noise spectra in the high frequency region was discussed. The theory which links this decrease with the realized turbulent energy spectrum $E(k)$ (where k is the wave number $k = 2\pi/\lambda$) provided by FRPM was formulated. By its implementation FRPM realizes a Gaussian energy spectrum $E_G(k)$. Contrary to that, Liepmann[71] proposed a different form of the energy spectrum $E_L(k)$ with a much shallower decay of turbulence energy towards higher wave numbers. This can be seen in Figure A.2 (a) in Appendix A.4. In Reference [70] a method was shown to realize this Liepmann energy spectrum with a superposition of differently scaled mutually uncorrelated individual FRPM realizations with a Gaussian spectrum. Details on this can be found in Appendix A.4. Practically, multiple simulations with differently scaled TKE distributions on the FRPM patch according to Equation A.57 need to be conducted and later on superposed. The computational effort is thus multiplied by the number of scaled Gaussian FRPM realizations to achieve the Liepmann energy spectrum. First test cases showed that a number of ten individual simulations was needed to achieve a precise form of the spectrum. With a logarithmic distribution of the scaling factors a reduction to five individual simulations might be feasible. Still, the computational effort is increased by the factor of five with this method[11].

Throughout progressive research and testing it was found, that a smaller minimum length scale factor together with an adapted (finer) patch and CAA resolution, brought the same effect as the Liepmann realization. Especially in the high frequency region, the simulated sound pressure levels are better matching the available experimental results. As this solution is considered computationally more efficient than the Liepmann method, it is thus better suitable for the proposed best-practice CAA airfoil simulation. For the planed simulations of multiple airfoils it is chosen as the best tradeoff of result quality and computational efficiency. A non-dimensional grid spacing of $\Delta x/l_c = 0.0005$ must be used for the FRPM patch as well as the CAA grid in the source region to obtain reliable results for the desired frequency range. The minimum length scale resolved by FRPM $l_{\min}$ must be at least $l_{\min} = 0.002$. With this settings $l_{\min}$ is resolved with a resolution of four patch cells.

Figure 3.16 depicts the differences of the simulated CAA results in contrast to measurement data from Reference [72]. Together with the measurement values (black squares) error bars indicate the uncertainty range of the acoustic wind tunnel data which is given by 3 dB. For the symmetric NACA0012 airfoil under an angle of attack of zero degrees it can be seen, that the reference CAA simulation (solid line; $\Delta x/l_c = 0.0008$ and $l_{\min} = 0.005$) is able to reproduce the peak frequency of the experimental data around $f = 1.5\,\text{kHz}$. Up to a frequency of $f = 3\,\text{kHz}$ the sound pressure level decay lies within the uncertainty range of the measurements. For higher frequencies the simulated values are too low. In contrast to that, the Liepmann FRPM method (dashed line), which was condensed from ten individual simulations, shows a better matching in the high frequency range. Up to $f = 20\,\text{kHz}$ the CAA data lies well within the error bars. Note, that the used CAA mesh

[11] The parallel processing of the different FRPM source patches as multiple uncorrelated sources within one CAA simulation could help to reduce this effort. Thus, only additional CPUs are necessary to process the additional FRPM patches. In a limited resource environment this also might become a problem.

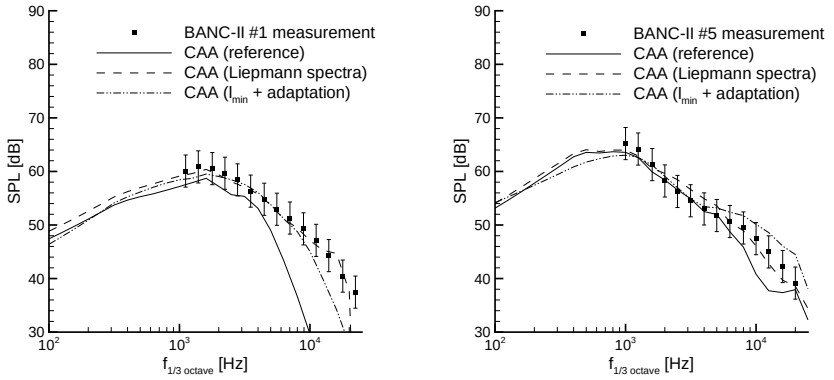

Figure 3.16: Influence of the Liepmann turbulence spectrum realization by the superposition of multiple FRPM realizations in contrast to the FRPM standard settings and the improved settings with smaller l_{min} values and adapted patch and CAA grid resolutions: (a) far-field spectra of NACA0012 airfoil according to BANC-II case #1 settings ($\alpha = 0\,^\circ$, $Re = 1.5 \cdot 10^6$, $M = 0.1664$, $l_c = 0.4\,\text{m}$); (b) far-field spectra of DU-96-W-180 airfoil according to BANC-II case #5 settings ($\alpha = 4\,^\circ$, $Re = 1.13 \cdot 10^6$, $M = 0.173$) directly below the trailing-edge at the distance $y/l_c = 2.5$.

was designed for a maximum frequency resolution of only $f = 10\,\text{kHz}$ and thus values above that maximum resolvable frequency have to be treated with caution. Considering the computationally much more efficient adapted CAA setup (dashed double dotted line; $\Delta x/l_c = 0.0005$ and $l_{\min} = 0.002$) an agreement with the measurements throughout all frequencies up to $f = 10\,\text{kHz}$ can be seen.

In Figure 3.16 (b) the same analysis is performed for the cambered, non-symmetric DU-96-W-180 airfoil with an angle of attack of $\alpha = 4\,^\circ$. The same trends as for the NACA airfoil can be seen. The reference CAA setup is able to correctly simulate the sound pressure levels up to a frequency of $f = 4\,\text{kHz}$. Beyond that the values are too low. Again, the Liepmann setup remedies this by stocking up the values between $f = 4\,\text{kHz}$ and $f = 20\,\text{kHz}$. In the DU96 case, the adapted CAA setup also amplifies the sound pressure levels in the high frequency range while the rest of the spectrum remains nearly unchanged. Unfortunately a slight overprediction of the values starts beyond $f = 6\,\text{kHz}$. Still, up to the desired maximum CAA grid resolution of $f = 10\,\text{kHz}$ (for this case) the simulated values lie within the uncertainty range.

It can be argued, that the Liepmann method produces the better results concerning the agreement with experimental data, especially in the high frequency range. However, through the conduction of multiple simulations it is computationally much more expensive. In contrast to that, the adopted method has only a slight increase in computational

time due to the increased mesh density in the source region around the trailing-edge. Furthermore the simulated results still show a reasonably good agreement with validation data. The slight inaccuracy in the very high frequency region is accepted, because the reproduction of the rest of the spectrum is done correctly. When overall sound pressure levels are considered, the contributions of this very low levels in the high frequency range are almost negligible. The results are acceptable for the planned evaluation of different airfoil shapes.

3.3.4 Grid Refinement Study

Similar to the analysis for the CFD mesh, the CAA and FRPM meshes are tested towards their influence on the simulated results. Therefore, three different CAA meshes are created for the NACA0012 airfoil. The coarse grid (N1) counts 326k cells in total and has a smallest cell size of $\Delta x/l_c = 0.0006$ at the patch area in the vicinity of the trailing-edge. The medium grid (N2) counts 473k cells and has a smallest cell size of $\Delta x/l_c = 0.0005$. For the finest mesh (N3) 680k cells are used. The smallest cell size is $\Delta x/l_c = 0.0004$. For all meshes the same FRPM source patch with the coarsest resolution of $\Delta x/l_c = 0.0006$ and with a dimension of 500 by 166 cells is used for the source generation. The flow parameters are chosen in agreement with the BANC-II #1 test case ($\alpha = 0\,^\circ$, $M = 0.1664$ and $Re_c = 1.5 \cdot 10^6$).

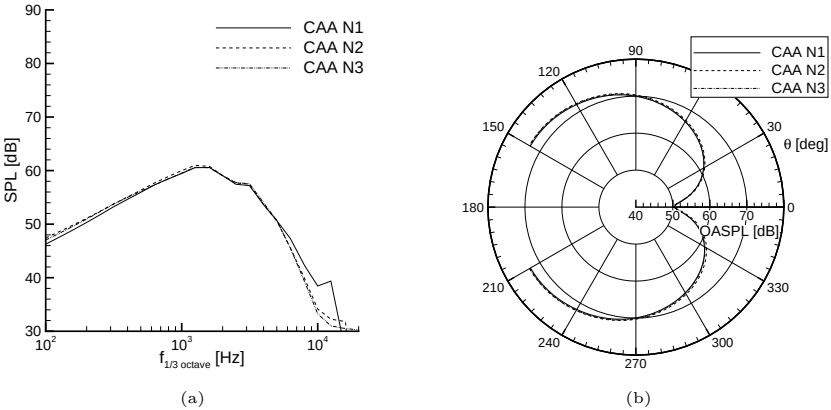

(a) (b)

Figure 3.17: Results of grid refinement for a NACA0012 airfoil according to BANC-II case #1 settings ($\alpha = 0\,^\circ$, $Re = 1.5 \cdot 10^6$, $M = 0.1664$, , $l_c = 0.4\,\mathrm{m}$) : (a) one-third octave band spectra directly below the trailing-edge ($\theta = 270\,^\circ$; $r/l_c = 0.8$); (b) directivity plot around the trailing-edge recorded at $r/l_c = 0.8$.

The results for the three different grids are depicted in Figure 3.17. One-third octave band SPL spectra are shown in Figure 3.17 (a) for a virtual microphone at a distance $r/l_c = 0.8$

directly below the trailing-edge. It can be seen, that the difference between these three solutions is less than 0.5 dB for all frequencies up to 5 kHz. Above that frequency the coarse N1 mesh shows slightly higher values. These might come from an under resolution of the higher frequencies by the grid. However, for the important frequency range up to 10 kHz, the solution tends to converge against the finest mesh resolution N3. Thus, it can be considered as grid-independent.

This assumption is also underlined by the directivity plot shown in Figure 3.17 (b). Here, overall sound pressure level (OASPL) are shown along a microphone circle around the trailing-edge with a radius of $r/l_c = 0.8$. The missing values between $\theta = 150\,^\circ$ and $\theta = 210\,^\circ$ are due to the intersection of the microphone circle with the airfoil in that region. All three grids show very small deviations in overall sound pressure levels due to the minor influence of the high frequency bands in the summation. The anticipated forward inclined lobe directivity of the trailing-edge noise is reproduced by all simulations. To save computational effort while maintaining result quality, subsequent simulations are conducted with a resolution similar to the medium mesh N2 ($\Delta x/l_c = 0.0005$ in the patch area, as stated in Section 3.3.1).

To determine the influence of the spatial FRPM source patch resolution an additional grid refinement study is conducted. Herein three FRPM patches with different grid spacings are analyzed. For each patch a single FRPM simulation is carried out. As these simulations were done without the underlying CAA grid, only the ability of the turbulence reconstruction is evaluated. It is argued that with the same reconstructed turbulence field, the influence on the fluctuating source term and the resulting sound waves is the same. Hence, if FRPM shows an independence of the used patch resolution, the acoustic results are supposed to be similar. The patch resolution is chosen analogously to the smallest resolutions of the CAA grid refinement study. The coarse N1 grid has a cell size of $\Delta x/l_c = 0.0006$ while the medium N2 grid has a size of $\Delta x/l_c = 0.0005$ and the fine N3 grid a size of $\Delta x/l_c = 0.0004$. For all patches equidistant quadratic cells were used. To keep the same geometric extensions for all patches the total number of cells is adopted. The resolutions are ranging from 500 by 166 cells for the coarse N1 patch over 600 by 200 cells for the medium N2 patch to 750 by 250 cells for the fine patch. The number of FRPM particles is determined by the total amount of patch cells ($n_{\text{particle}} = 2.5 \cdot n_{\text{cells}}$).

Figure 3.18 shows profiles of the non-dimensional turbulence kinetic energy distribution along chord-perpendicular lines at different positions behind the trailing-edge. Therefore, the turbulence statistics from the time resolved turbulent flow field of FRPM are calculated and compared to the target CFD input statistics. For an ideal solution the CFD input profile should be reproduced by the FRPM statistics (see also Section 3.3.3). It can be seen, that for all positions the reconstructed FRPM values are above the CFD values in the order of 15 to 20 percent, but similar in general shape. However, the deviation between solutions of the different patch resolutions N1 to N3 is much smaller. Only for the position $x_1/l_c = 1.05$, the coarse N1 mesh shows slightly higher values compared to N2 and N3. Note, due to the stochastic nature of the FRPM turbulence reconstruction a certain degree of uncertainty is always immanent in the solutions. Thus, the turbulence reconstructions from all different meshes can be considered nearly identical. For further computations a patch resolution of $\Delta x/l_c = 0.0005$ (like in the medium N2 grid) is chosen to reduce computational effort.

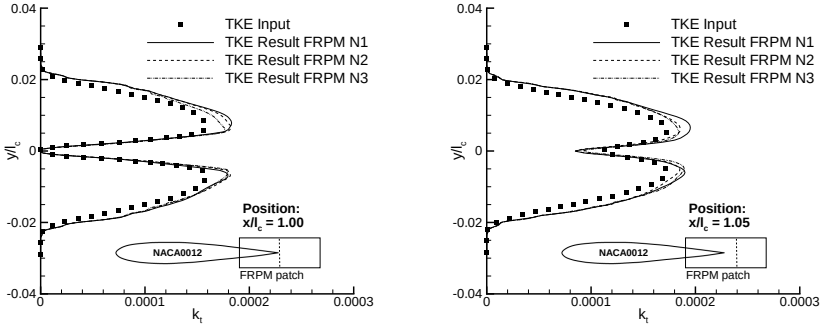

Figure 3.18: Reconstruction of turbulence kinetic energy k_t for NACA0012 ($\alpha = 0\,^\circ$, $M = 0.1664$, $l_c = 0.4\,\mathrm{m}$) with different grid resolutions compared to CFD input; (a) normalized TKE at $x_1/l_c = 1.00$; (b) normalized TKE at $x_1/l_c = 1.05$.

3.3.5 Best Practice Aspects

In this section, the best practice settings for the two-dimensional airfoil trailing-edge noise simulations are summed up. They were found throughout various simulations, test cases and validations with experimental data. The settings are used on all subsequent simulations. If other settings are used, this will be clearly mentioned. However, the diligent and continuous use of these best practice settings will ensure unvarying result quality. It is argued that emerging differences in the results are thus due to the physical mechanisms governing the trailing-edge noise generation and not due to changes in FRPM or CAA settings. Comparisons between the results of different airfoil geometries even with only minor differences can be done in reasonable accuracy.

The main an important settings are:

- **High Quality CFD Inputs**
  - The SST-k-ω turbulence model has to be used for the RANS turbulence simulation.
  - For transition modeling, the $\gamma - Re_\theta$ transition model in combination with the SST-k-ω turbulence model has to be used.
  - The viscous sublayer and the region close to the airfoil's wall (up to $0.3 l_c$ above the wall) need to be resolved with at least 100 grid cells. The dimensionless wall distance must be less than one ($y^+ < 1$).

- **CAA Mesh Requirements**
  - The CAA mesh should extend at least six by six chord lengths with the trailing-edge in the center (consequently, the microphone circle for the evaluation can be set up at a distance of $2.5l_c$ around the trailing-edge).
  - The dimensionless far-field resolution should be $\Delta x/l_c = 0.01$. Thus, the TBL-TEN spectrum lies always within the resolved frequency range. Changes of the absolute reference length (absolute chord length) are covered by Strouhal scaling effects.
  - In the source patch area, the resolution of the CAA mesh and the FRPM patch must be identical. This requires a much finer resolution of the mesh in the vicinity of the trailing-edge. The transition from the fine mesh to the much coarser outer mesh should be done with an O-grid blocking strategy (clamping). The total number of grid cells should be around one million to resolve an area of six by six chord lengths with a reasonable refinement in the source region.
  - Damping spots at trailing and leading-edge of the airfoil must be added for stability enhancement.
- **FRPM Requirements**
  - The patch must be created as one block with squared cells extending from $x/l_c = 0.8$ to $x/l_c = 1.2$ and $y/l_c = -0.05$ to $y/l_c = 0.05$ with a cell size of $\Delta x/l_c = \Delta y/l_c = 0.0005$. For thicker airfoils or thicker boundary layers the y-extension must be adapted so, that the full boundary layer profile lies within the patch area.
  - The number of FRPM particles must be 2.5 times the number of patch cells
  - To ramp the source strength up and down, a weighting function of the form $w(x) = f\left(sin^2\left(\frac{x}{0.18l_c}\frac{\pi}{2}\right)\right)$ scaled to a length of $0.18l_c$ must be used in x-direction on both sides. In the y-direction a weighting function of the form $w = f\left(sin^2\left(\frac{y}{0.01l_c}\frac{\pi}{2}\right)\right)$ with a length of $0.01l_c$ must be used.
  - The minimum resolved length scale must be $l_{\min} = 0.002$. It is resolved by four patch cells.
- **PIANO Requirements**
  - A total number of 400000 time steps must be simulated with a non-dimensional time step of $\Delta t = 2 \cdot 10^{-4}$.
  - A microphone circle with 360 equidistantly positioned microphones should be set up with a radius of $2.5l_c$ around the trailing-edge. It is sufficient to sample the microphone data ($p'(t)$) at every 50th non-dimensional time step.
  - Using 14 CPUs, where the CAA simulation is done parallel on 13 CPUs and the FRPM turbulence reconstruction is done on one single CPU, results in an overall wall clock time of less than 16 hours for a complete simulation[12].

[12] Simulations were conducted in 2014 and 2015 using the DLR case cluster which is equipped with Intel Xeon X5670 processors with a base frequency of 2.93 GHz.

- **Post-Processing**
  - The microphone signals should be converted to narrow-band and one-third-octave band spectra for evaluation.
  - The 2D to 3D correction according to Equation 2.61 must be applied.
  - From the evaluation of several test cases, it was found, that a constant offset calibration of -4.5 dB must be added to all levels in the spectrum, disregarding the frequency (see Reference [70])[13].

A standard `PIANO` input file - as used for all airfoil simulations - with the parameters set as described above is attached in Appendix A.5.

3.4 Data Processing and Scripting

Throughout the investigation of airfoil trailing-edge noise of different geometries and flow conditions (e.g. angle of attack, flow velocity, position of laminar to turbulent boundary layer transition) various simulations needed to be carried out. Therefore, an automized toolchain with automatic data processing was set up. The risk of errors due to manual data input is significantly reduced. Furthermore, several setups can be simulated at the same time (assuming available computational resources). This directly increases the economic yield of the analysis regarding overall simulation time. The consistent use of similar meshing strategies and simulation setups guarantees a proper comparability and reproducibility of the numerical results.

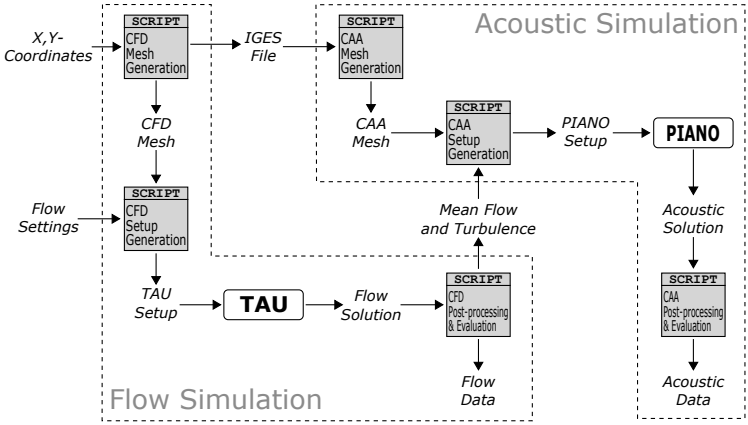

Figure 3.19: Overview of the used scripts for the automation of the simulation process.

[13] One reason for this offset might be the overprediction of the turbulence values by the FRPM reconstruction of 15[%] to 20[%] (see Section 3.3.4).

Figure 3.19 depicts the subsequent automation scripts used for the processing of the simulation. The scripts are highlighted as gray boxes. Each script is written in bash. System commands are used throughout the scripts to run specific software like grid generators or post-processing tools (e.g. `TECPLOT`). Each script can be used on its own, as long as the required input data is available. Thus, it is also possible to run the flow simulation part of the analysis without the acoustic calculations if the main focus lies on the integral flow parameters.

In the following, a short description of each automation script is given:

- **CFD Mesh Generation**
  - The grid generator `ICEM CFD` is automized via an `ICEM` replay script (successive sequence of program commands).
  - The standard replay script is modified to the new x and y coordinates (given as ASCII file).
  - `ICEM` automatically adjusts all structured near airfoil blocks so, that the wall normal edges are as perpendicular as possible to the airfoil surface.
  - The unstructured outside mesh is generated, the airfoil geometry is saved as IGES file and the final mesh in the `TAU` readable format (popform) is written.
- **CFD Setup Generation**
  - A standard `TAU` setup file is copied and the used CFD mesh is adjusted to the new airfoil.
  - The flow parameters (angle of attack, Reynolds number, transition) are read from a user provided table. Individual folders, containing the mesh and the specific `TAU` input files, are created for each parameter set.
  - The folders are copied to the high performance cluster and the simulations are started.
- **CFD Post-Processing and Evaluation**
  - The CFD folders are gathered and copied back to the local machine.
  - From the data, the integral coefficients (lift, drag, torque) are extracted. Moreover, specific distributions, e.g. the pressure coefficient along the airfoil's surface or the TKE and velocity distribution in the trailing-edge region, are extracted using `TECPLOT`.
  - The flow data is prepared for the CAA simulation step. `TECPLOT` is used to nondimensionalize the mean-flow variables and extract the turbulence statistics in the FRPM patch area.
- **CAA Mesh Generation**
  - The grid generator `POINTWISE` is used. Like with the CFD mesh, the procedure is automized using a replay script.
  - The IGES geometry file is read and the default CAA mesh is modified so, that the near airfoil CAA mesh is adapted to the new geometry.

  - A mesh smoothing is performed in `POINTWISE` and the resulting mesh is written in PLOT 3D format and thereafter converted in the `PIANO` readable popform format using `TECPLOT`.

- **CAA Setup Generation**
  - The provided mean-flow is interpolated onto the CAA mesh.
  - A default `PIANO` input file is copied for each set of input parameters and the respective mean-flow, patch and CAA mesh files are set in the `PIANO` input file. For each parameter set, one `PIANO` input folder, with all files needed to conduct the simulation, is created.
  - The folders are copied to the high performance cluster, where the acoustic simulations can be done in parallel on the available resources.

- **CAA Post-Processing and Evaluation**
  - The acoustic solution folders are gathered and copied back to the local machine.
  - From the recorded acoustic pressure over time signals (microphone circle) spectral data is calculated using an FFT analysis.
  - From the spectral data over all sound pressure levels (OASPL) and directivity distributions of the emitted trailing-edge noise signals are calculated.

The vast amount of produced data throughout the conducted simulations builds the basis for the trailing-edge noise investigation. Multiple airfoil shapes under different operational conditions can be studied using the automized procedure. Within an industrial environment, the flow simulation data can be considered given as this analysis is crucial for the particular choice of an airfoil for a new rotor blade design. The only additional expense results from the acoustic simulations, as well as the preparation of the CFD data so, that it can be used as input data for the CAA simulation. After completing both simulation tasks it is possible to compare the airfoil performance on an aerodynamic as well as acoustic scale.

4 Results and Discussion

This chapter contains the results of the two-dimensional airfoil analysis. Relevant aspects for the trailing-edge noise generation as well as the aerodynamic relations will be discussed. For the simulations the models and approaches described in Chapter 3 are inherently used. Variations of this settings (if used) are explicitly mentioned. The results are gathered with the overall focus to highlight the design driving aspects for low noise airfoils. The influences of geometry and flow variations are systematically analyzed. All is done with regard to the aerodynamic performance and under structural constraints.

First, the validation of the hybrid CAA/CFD approach is shown in Section 4.1. Therefore measurement data and test cases from the BANC-II workshop are used to validate the simulated results. Thereafter, the systematic geometry and flow parameter variation strategy is described in Section 4.2. Starting from a reference airfoil different geometry parameters and their influence on the emitted trailing-edge noise signal are analyzed. Moreover, the influence of laminar turbulent boundary layer transition is studied. The results are grouped in Section 4.3. Starting from these general trends, a more precise investigation with aerodynamic data from the boundary layer is conducted in Section 4.4. From these discoveries a strategy for the development of new low noise airfoils is derived in Section 4.5 and purposes for future airfoil design trends are presented.

4.1 Validation Test Cases from BANC-II

The validation of the outlined hybrid CFD/CAA method is shown according to available TBL-TEN measurement data from the BANC-II (Benchmark for Airframe Noise Computations) workshop[73].

The best practice settings according to Section 3.3.5 are used for the numerical simulations. All shown sound pressure level spectra are corrected according to Equation 2.61. Thus, the sound radiation is corrected to account for the 3D case, as measured in the BANC test cases. Untapered, unswept airfoil sections with a wetted span of 1 m are considered. A common off-set calibration of -4.5 dB is used on all simulated CAA spectra.

A microphone position orthogonal to the chord 2.5 chord lengths below the trailing-edge is chosen to compare simulated and measured acoustic data[1]. According to the BANC-II problem statement, the provided measurements have an uncertainty of roughly 3 dB. This is indicated by error bars in the graphs. Furthermore, spectra calculated by the semi-empirical Brooks, Pope and Marcolini BPM tool NAFnoise[19] are additionally plotted in the following graphs (dashed lines). In general, a good match between simulated and

[1] In the BANC test cases airfoils with a chord lengths of $l_c = 0.4$ m were measured. The microphone position was chosen in the far-field at a distance of $r = 2.5 l_c = 1$ m. The same far-field observation position was chosen for the CAA simulations. The simulation data was then scaled to account for an airfoil with a span of 1 m and an observer distance of 1 m.

measured spectra is achieved. The peak frequency and the SPL decrease towards higher frequencies are reproduced by the simulations. Detailed results for each test case will be discussed in the following subsections.

The five test cases contain a NACA0012 airfoil under different angles of attack and flow Mach numbers as well as a cambered DU96 airfoil.

4.1.1 Test case #1 NACA0012 ($l_c = 0.4\,\mathrm{m}$, $\alpha = 0\,^\circ$, $M = 0.1664$)

The agreement of the CFD results with experimental data is reasonably accurate. Thus, it will only be shown and discussed for the first test case of the NACA0012 airfoil at zero degree angle of attack. Figures 4.1 (a) to (f) show boundary layer values simulated by `TAU` and data from wind tunnel experiments conducted by IAG Stuttgart[74]. For the evaluation, profiles are compared along a vertical line (perpendicular to the airfoil chord) positioned at a distance of 0.38 % main chord behind the airfoil's trailing-edge.

The results are in good agreement with the provided experimental data. The values for the normalized velocity profile in streamwise direction x (Figure 4.1 (a)) are in line with the RANS computations. The velocity profile of the `TAU` simulation shows slightly higher values. However, the general shape and boundary layer thickness (location where $0.99U_\infty$ is reached) match. This implies, that the used k-ω-SST turbulence model is suitable for this case. For the used two-equation model with its isotropic turbulence ($\overline{u_1'u_1'} = \overline{u_2'u_2'} = \overline{u_3'u_3'} = \overline{u'u'}$), the Reynolds stresses can be evaluated from the turbulence kinetic energy according to Equation2.18:

$$\overline{u'u'} = \frac{2}{3}k_t. \tag{4.1}$$

Together with the assumption for a flat plate boundary layer, that the main Reynolds stresses in streamwise, spanwise and wall normal direction occur in relative proportion[42, 59, 75]

$$\overline{u_1'u_1'} : \overline{u_2'u_2'} : \overline{u_3'u_3'} = 4 : 3 : 2, \tag{4.2}$$

the separate Reynolds stresses can be calculated from the CFD results. They compare well to the experimental data (see Figure 4.1 (c), Figure 4.1 (d) and Figure 4.1 (e)). For all three directions slightly higher values close to the wall can be observed for the experimental data, driving the assumption that the SST-k-ω model under-predicts the turbulence in this region. However, concerning the comparison made in Figure 3.13, where it is shown, that FRPM tends to over predict the input TKE values, these tow effects seem to annul each other. Thus, the under prediction of the CFD simulation is compensated by the over prediction of the FRPM turbulence reconstruction. Figure 4.1 (d) depicts the longitudinal turbulent length scale l which can be calculated from the turbulence kinetic energy k_t and the specific dissipation ω according to Equation 2.60 ($l = \frac{c_l}{C_\mu} \cdot \sqrt{\frac{k_t}{\omega}}$). It can be observed that, for a $l_{\mathrm{fac}} = c_l/C_\mu$ of 6.0 (referring to Section 2.3.6) the measured length scales (black squares) are higher as the computed ones (dashed line). If the ratio is adapted to 8.0 (solid line), the fitted computational results match the measured values concerning the absolute level. However, the experimental length scales imply a more constant length scale behavior than seen by the numerical solution. Moreover, the choice

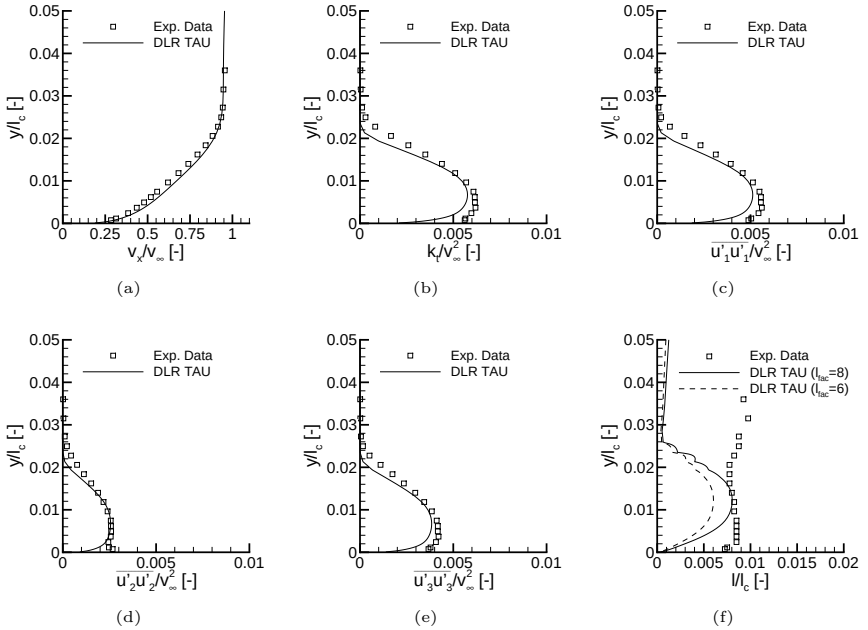

Figure 4.1: Boundary layer properties extracted at $x/l_c = 1$ in y-direction for BANC case #1 (experimental data from IAG Stuttgart[72]); (a) normalized velocity profile in streamwise direction; (b) normalized turbulence kinetic energy; (c) normalized Reynolds stress in streamwise direction; (d) normalized Reynolds stress in wall normal direction; (e) normalized Reynolds stress in spanwise direction; (f) longitudinal integral length scale for different $l_{\text{fac}} = c_l/C_\mu$ ratios.

of $l_{\text{fac}} = 6.0$ has shown better agreement for the far-field noise spectra and is thus chosen for the best practice setup.

Figure 4.2 (a) shows an instantaneous snap shot of the non-dimensionalized fluctuating sound pressure field for the NACA0012 #1 test case. The dipole like behavior and the forward inclined directivity (cardioid) of the main radiation as well as the areas with less sound emission in the direction of the chord are clearly visible. The dashed black circle indicates the position of the virtual microphones at a distance of $2.5l_c$ around the TE. A total number of 360 equidistant positioned virtual microphones is used to calculate the normalized directivity plots in Figure 4.2 (b). The lobe characteristic of the radiated sound can be seen. From these plots, one may infer that with increasing frequency the directivity tends towards the theoretical cardioid shape in an oscillating manner, particularly occuring in the upstream directions as expected. Likewise one may expect the directivity to converge to a true dipole shape for very low frequencies, as soon

as the airfoil becomes an acoustically compact object.

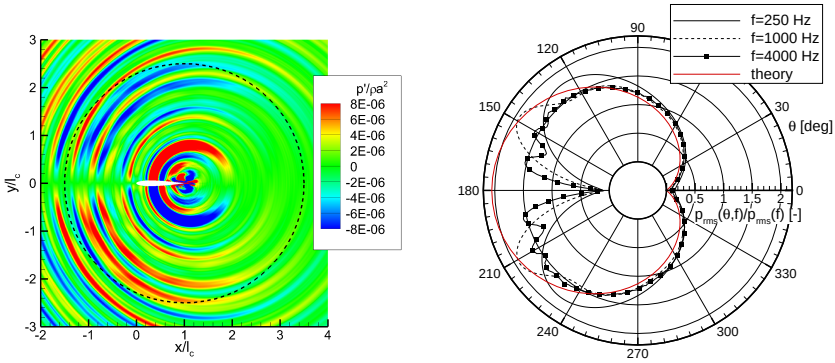

(a) (b)

Figure 4.2: CAA simulation results for BANC case #1: (a) snapshot of non-dimensional sound pressure field around the NACA0012 airfoil with indicated microphone circle with $r = 2.5l_c$; (b) normalized far-field directivities for different frequencies and theoretical flat plate cardioid directivity.

For the reference position ($2.5l_c$) directly below the trailing-edge the resulting TBLTEN spectrum is shown in Figure 4.3 (a). The simulated CAA result is compared to the experimental spectrum[2] as well as to the BPM values. It can be seen, that the CAA spectrum (solid line) matches the peak frequency of the experimental data (black squares) which is around 1.5 kHz and lies in the uncertainty range until approximately 10 kHz. The decrease of the spectrum towards higher frequencies beyond 8 kHz is too strong, which results in a disagreement of values in the frequency range higher than 10 kHz. Note, that the desired maximum resolvable frequency of the used computational mesh is 10 kHz. The spectrum calculated by the tool NAFnoise using the BPM method[19] is represented by the dashed line. While peak frequency and decay towards higher frequencies match, the absolute peak level is slightly over predicted. Note, that the BPM model relies on NACA0012 measurements and is therefore comparatively accurate for this kind of airfoil.

4.1.2 Test case #2 NACA0012 ($l_c = 0.4\,\mathrm{m}$, $\alpha = 4\,^\circ$, $Ma = 0.1641$)

In contrast to the symmetric flow situation in case #1 a higher angle of attack of $\alpha = 4\,^\circ$ is chosen for NACA0012 airfoil in the second test case. Figure 4.3 (b) shows the one-third-octave band SPL spectra. Experimental data are reproduced throughout the whole frequency range. Due to the higher angle of attack the peak frequency is shifted towards

[2] All acoustic experimental data were obtained in DLR's AWB (Acoustic Wind Tunnel Braunschweig) wind tunnel facility in Braunschweig.

lower values. It lies around 1 kHz for the CAA approach, which is in good agreement with the measurement data and the BPM method. Again, beyond 10 kHz (which is the maximum resolvable frequency) the decay of the SPL levels is too steep compared to experimental data. Unfortunately, 1 kHz represents the lower bound for the measured SPL values (due to current wind tunnel characteristics) and no values for validation of the low frequency behavior are available. However, in contrast to the BPM values (dashed black line) higher sound pressure levels are simulated by the CAA method for frequencies lower than 0.5 kHz.

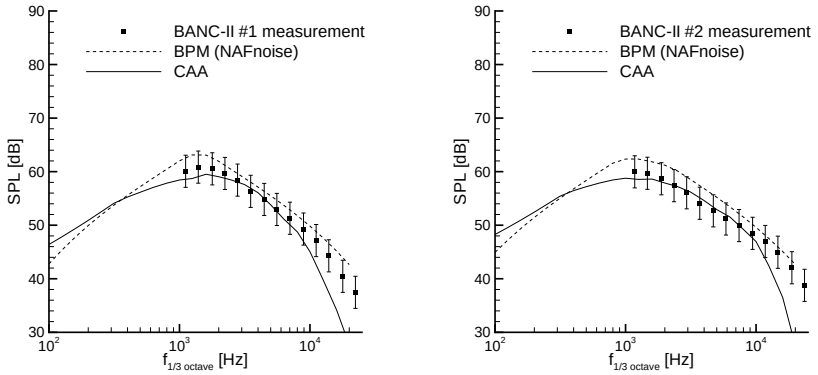

Figure 4.3: Far-field sound pressure level spectrum at reference location for: (a) BANC case #1 and (b) BANC case #2.

4.1.3 Test case #3 NACA0012 ($l_c = 0.4\,\mathrm{m}$, $\alpha = 6\,^\circ$, $Ma = 0.1597$)

While maintaining flow speed and chord length an even higher angle of attack of $\alpha = 6\,^\circ$ was chosen for test case #3. The resulting spectrum is shown in Figure 4.4 (a). It can be observed, that the peak frequency is shifted further towards lower values with higher angle of attack. For this case it is around 0.8 kHz. Unfortunately, measurement data is only available up to lower frequency of 1 kHz. The simulated values are in good agreement and within the uncertainty range of the experimental data up to 10 kHz. It seems, that the reproduction of higher frequencies is now better than in case #1 and case #2. Another fact which can be seen in this case is the general influence of the angle of attack increase on the far-field noise spectrum. The peak frequency shifts towards lower values and for the higher frequencies the SPL values are increasing. This is due to the fact that the spectrum is a combination of two single spectra. One low frequency part coming from the suction side, with its relatively wide boundary layer and a second high frequency part coming from the pressure side, with the thin boundary layer. To

underline this assumption the far-field one-third-octave band SPL spectra from pressure and suction side are simulated independently. This is achieved by separating the patch into two parts at the trailing-edge along the dividing streamline, one for the suction side and one for the pressure side. The results, together with the spectrum simulated with the whole patch, are shown in Figure 4.4 (b). As the angle of attack increases, the two spectra drift more and more apart. This behavior of the simulation is in good agreement with trailing-edge noise theory (see also References [3, 17]).

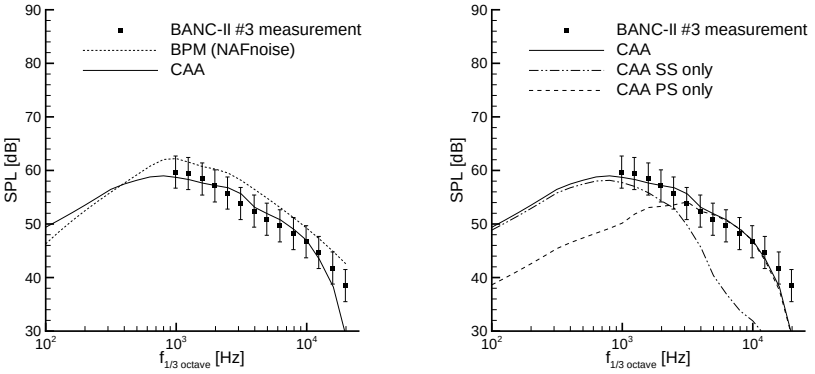

Figure 4.4: Far-field sound pressure level spectrum at reference location for: (a) BANC case #3 and (b) BANC case #3 individual contributions of airfoil suction and pressure side.

4.1.4 Test case #4 NACA0012 ($l_c = 0.4\,\mathrm{m}$, $\alpha = 0\,^\circ$, $Ma = 0.1118$)

In the fourth test case a lower flow speed for the zero degree angle of attack case (test case #1) is investigated. Results are shown in Figure 4.5 (a). The calculated sound pressure levels match the measured values. Peak frequency and decay rate are reproduced by the CAA simulation. Due to the lower velocity in this test case, lower SPL levels compared to case #1 can be observed. Between case #1 and case #4 a SPL difference of roughly 8.5 dB for the SPL spectra as well as for the OASPL values can be seen from the results. This difference is in compliance with the theoretical Mach number scaling law from the Ffowcs Williams and Hall theory for trailing edge noise radiated from a semi-infinite flat plat[9]. It states that the noise scales with the fifth power of the Mach number. The analytically calculated SPL difference with the underlying power law and an exponent of five yields a $\Delta SPL = SPL_1 - SPL_4 = 5 \cdot 10 \log(M_1/M_4) = 8.63\,\mathrm{dB}$. Additionally, a frequency scaling can be applied to case #4 using the formulation for the Strouhal number

St for the relation of the frequency f, the characteristic length L and the velocity u:

$$St = \frac{fL}{u}. \tag{4.3}$$

Assuming the same characteristic length, Strouhal number and ambient conditions, the frequency scaling due to the Mach number can be formulated: $f_{\text{scaled}} = f_4 \cdot (M_1/M_4)$. The comparison of the spectra of case #1 and case #4 is shown in Figure 4.5 (b). Additionally, the spectrum of case #4 is shifted and scaled to the Mach number of case #1 (dashed line with symbols). A nearly perfect agreement can be seen. The underlying physical scaling laws are fully reproduced by the CAA method.

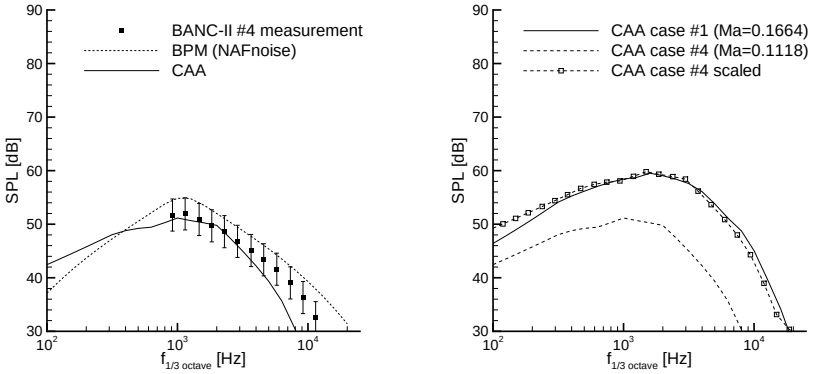

Figure 4.5: Far-field sound pressure level spectrum at reference location for BANC case #4: (a) alone and (b) scaled according to Mach number effects together with BANC case #1.

4.1.5 Test case #5 DU96-W-180 ($l_c = 0.3\,\text{m}$, $\alpha = 4\,^\circ$, $Ma = 0.1730$)

In test case #5 a cambered, non-symmetric DU96-W-180 airfoil section under an angle of attack of $\alpha = 4\,^\circ$ is simulated. In contrast to the NACA0012 airfoil from test cases #1 to #4 this airfoil shape is more similar to the ones used in actual wind turbine blades and as such represents a more realistic test case for the desired use of the CAA simulation method. The computed results are juxtaposed to the experimental data in Figure 4.6 (a). The broadband noise spectrum is in good agreement with the experimental data and lies within the uncertainty range up to 10 kHz. The peak frequency at 1 kHz matches the measured value. In the simulated spectrum two distinct humps can be seen. The first one at the peak frequency of 1 kHz and the second one at a frequency of 4-5 kHz, which also

agrees with the measured data. They can be related to the two individual contributions of suction and pressure side to the overall signal (see detailed description in case #3).

Additionally, results for the semi-empirical BPM code are depicted (dashed line). Rather large inaccuracy can be observed throughout the whole frequency range greater than 2 kHz with this method. These are caused by the geometrical differences from the DU-96-W-180 airfoil to the reference NACA0012 airfoil of the BPM method. The semi-empirical approach tends to over estimate the high frequency levels emitted from the pressure side boundary layer.

Figure 4.6 (b) shows a directivity plot for the simulated overall sound pressure level around the airfoil. The graph is in reasonable agreement with the theoretical directivity for flat plate trailing-edge noise according to Reference [3, 76], where the directivity $\overline{D}(\Theta, \phi)$ is given as:

$$\overline{D}(\Theta, \Phi) \approx \frac{2 \sin(\Theta/2) \sin^2 \phi}{(1 + M \cos\Theta)\left[1 + (M - M_c)\cos\Theta\right]^2}. \tag{4.4}$$

See Figure 2.5 for further details. The smaller simulation values between $\Theta = 150\,^\circ$ and $\Theta = 210\,^\circ$ are due to the presence of the airfoil in this region, which is not considered in the flat plate test case. In order to compare absolute values, the theoretical prediction which is normalized to the TE noise radiation in the $\Theta = 90\,^\circ$ direction is multiplied with the absolute simulated values for the $90\,^\circ$ position. A nearly perfect agreement with experimental data can be found.

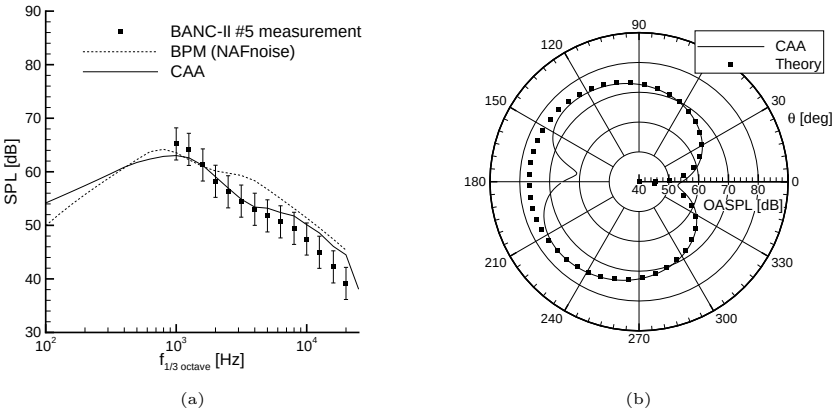

(a) (b)

Figure 4.6: Far-field acoustic data for BANC case #5: (a) one-third octave band spectrum at the reference location and (b) directivity plot of the overall sound pressure levels around the trailing-edge.

4.2 Geometry Variation Strategy

With the validated simulation tool chain, investigations of new airfoil geometries can now be conducted. Therefore, as a baseline setup, a common wind turbine airfoil, the DU96-W-180 developed by the Wind Energy Research Institute from the Delft University (see Reference [60]), is chosen. The airfoil has a maximum relative thickness of $t/l_c = 18\,\%$. It is is located at a chord position of $x/l_c = 35\,\%$. Contrary to airfoils desired for the use in airplane wings, wind turbine airfoils have a higher relative thickness to grantee the structural integrity of the long and slender rotor blades. The basic variation strategy relies on the systematic modification of the geometry. For each new generated geometry multiple simulations for the different flow parameters are conducted. In the post-processing step, aerodynamic and acoustic properties are extracted from the CFD and CAA simulations and the resulting trends are analyzed.

4.2.1 Geometry

A scheme similar to the four-digit NACA airfoil series approach is chosen for the systematic geometry variation. It relies on the assumption that an airfoil could be represented by its thickness distribution and mean line[3]. Therefore, the original thickness distribution from the DU airfoil is first extracted by reducing the camber of the DU96-W-180 to zero, meaning that for every x-coordinate the y-coordinates of suction and pressure side have the same absolute value (symmetric airfoil). The extracted thickness distribution along the chord is thereafter linearly scaled to the desired thickness (e.g. from $t/l_c = 18\,\%$ to $t/l_c = 20\,\%$). Additionally, the four-digit NACA mean line according to Ref.[77] is calculated using the following equations:

$$y_c = \begin{cases} \frac{m}{p^2}\left(2px - x^2\right) & 0 \leq x \leq x_{t_{\max}} \\ \frac{m}{(1-p)^2}\left[(1-2p) + 2px - x^2\right] & x_{t_{\max}} \leq x \leq 1\ . \end{cases} \tag{4.5}$$

The ordinate of the mean line is represented by y_c, with the maximum as a fraction of the chord m and its chordwise position p. By variation of m and p it is now possible to adjust the camber and the position of maximum camber for the DU-96-W-180 airfoil, while maintaining its original thickness distribution. The original DU airfoil shows a maximum camber of $m = 0.025$ at a chordwise position of $p = 0.37$. Using this values with the NACA scheme from Equation 4.5, the new mean line for the modified DU airfoil looks quite similar to the original one. See Figure 4.7 (a). A slight deviation can be observed towards the trailing-edge. The rear loading[4] of the original airfoil is slightly higher. Comparing the final geometries of both airfoils (Figure 4.7 (b)), this slight deviation makes almost no difference for the shape of suction and pressure side.

A relative geometry variation with the above described method is now possible. Thickness and camber are the modified parameters for the first tests. The modified DU airfoil

[3] The mean camber line or mean line is the locus of points midway between the upper and lower surfaces.

[4] Rear loading means the increased camber towards the trailing-edge. It results in a concave shape of the pressure side in the last fraction before the trailing-edge and is usually used to generate more lift from the pressure side. Additionally, due to the higher lift force close to the trailing edge, the pitching moment of the airfoil is influenced.

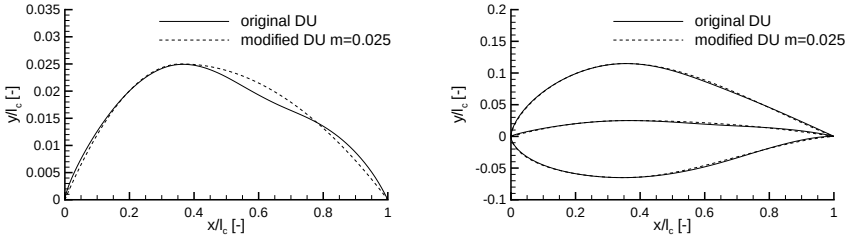

(a) (b)

Figure 4.7: DU-96-W-180 compared to modified baseline airfoil with NACA mean-line systematic; (a) detailed comparison of mean lines; (b) airfoil geometry.

is considered as the baseline airfoil. A total of nine airfoils are created with relative thicknesses of $t/l_c = 0.16, 0.18$ and 0.20 and a camber of $m = 0.015, 0.025$ and 0.035. They are shown in Figure 4.8. The relative thickness distribution and the position of maximum camber are fixed to the original DU values. The trailing-edge thickness is set to zero (thin, one point trailing-edge) for all airfoils, in order to simplify the mesh generation process. The geometrical changes are kept to relative subtle amounts, in order to retain the aerodynamic performance of the airfoils and their structural integrity. The adaptation of the thickness distribution and mean line also guarantees a smooth and steady airfoil surface on pressure and suction side. No dents, bumps or additional curvature discontinuities are added to the surface.

4.2.2 Flow Parameters

All airfoils are analyzed for four angles of attack $\alpha = 3\,^\circ, 4\,^\circ, 5\,^\circ$ and $6\,^\circ$, which are supposed to lie in the linear part (constant slope) of the lift curve, meaning that the lift linearly increases with the angle of attack and no separation should be present at the suction side. The inflow turbulence is nearly zero (0.01 % at the airfoil nose) and thus, the only noise mechanism of interest in this case is TBL-TEN.

The change of angle of attack allows to simulate different aerodynamic conditions for each airfoil. Consequently, it is possible to find matching conditions for noise comparisons. For a fair comparison of the airfoil noise contributions it is essential to compare test cases with same aerodynamic performances (for example lift coefficient c_L or L-over-D ratio (c_L/c_D)). Ambient pressure and temperature are chosen to ISO standard atmospheric conditions. The chord length is set to $l_c = 1\,\text{m}$ and the flow velocity is determined by the desired Reynolds-Number of 3 million[5].

[5] Typical wind turbine Reynolds numbers in the outer part of the rotor blade are often in a range between 3 and 6 million. The acoustic simulation approach is also capable of higher Reynolds Numbers, but the effects linking geometry and noise emission are supposed to be the same. Therefore, only one flow velocity is analyzed so far. If needed, a desired scaling approach can be applied.[54]

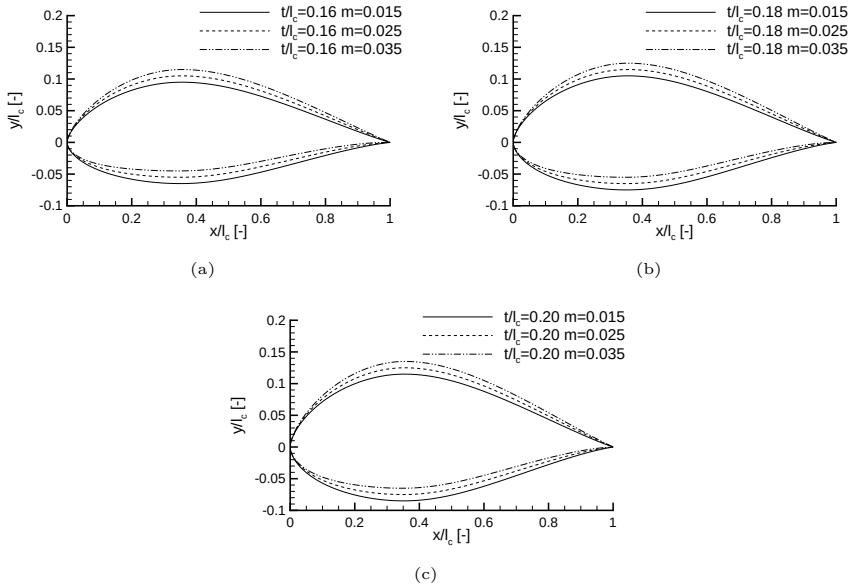

Figure 4.8: Airfoil geometries with varied camber for different relative thicknesses; (a) $t/l_c = 0.16$; (b) $t/l_c = 0.18$; (c) $t/l_c = 0.20$.

As laminar-turbulent transition plays an important role for the aerodynamic and acoustic performance two different settings are analyzed for each airfoil. The first setting comprises a fixed laminar turbulent transition at $x_{\mathrm{tr}} = x/l_c = 0.12$ on the suction side and $x_{\mathrm{tr}} = x/l_c = 0.15$ on the pressure side (which is in agreement with the values chosen in the BANC test case of the DU96-W-180[72]). The second setting uses the transition model ($\gamma - Re_\theta$ see Section 3.2) to calculate the natural transition locations. Normally, this leads to longer laminar running lengths than in the fixed transition case. The airfoil surface is supposed to be hydraulically smooth and the free-stream turbulence intensity less than 0.1 %. The flow parameters are summarized in Table 4.1.

4.3 Geometry Variation Results

First, the influence on the airfoil geometry is evaluated under aerodynamic aspects. Thereafter, a combined aerodynamic and aeroacoustic evaluation is done in Section 4.3.2. A precise analysis of the boundary layer flow data and the emitted trailing-edge noise is done in Section 4.4.

For each of the nine airfoils under investigation four angles of attack are analyzed. Additional to that, all cases are simulated with fixed and free laminar turbulent transition,

Table 4.1: Flow parameters for DU based airfoil variation.

parameter	symbol	value	unit
pressure	p_∞	101325	Pa
temperature	T_∞	288.15	K
density	ρ_∞	1.225	kg/m^3
velocity	u_∞	43.82	m/s
chord length	l_c	1.0	m
Re number	Re	$3 \cdot 10^6$	$-$
Ma number	M	0.129	$-$
angle of attack	α	3; 4; 5; 6	$^\circ$

resulting in total number of 72 combined CFD/CAA simulations. This rather large amount of computations requires the automated data processing strategy explained in Section 3.4. The computationally most expensive step is clearly the CAA simulation. It takes about 16 hours on a high performance cluster node (refer to Section 3.3.5). All other steps, including the `TAU` CFD simulation can be done in less than four hours, bringing the computational time to around 20 hours per case. For the simulations multiple nodes on the DLR CASE-cluster could be used for parallel simulations of the individual runs. This keeps the overall computational time within reasonable limits.

4.3.1 Aerodynamics

Figure 4.9 shows lift curves for the airfoils in the desired angle of attack range. Laminar turbulent transition is fixed according to the values given in Section 4.2.2. The linear increase of the lift coefficient c_L with increasing angle of attack underlines the statement, that no suction side separation is present in the chosen angle of attack range. It is clearly visible, that the airfoil camber m indicated by the symbols in Figure 4.9 (a) is the main influence parameter for the lift. An increase in camber of one percent leads to a lift gain of roughly $\Delta c_L = 0.1$. The slope of the nine curves is almost identical and independent of the geometry. Considering the relative thickness - indicated by the line style - only a minor influence on the lift coefficient can be observed. The 20 % thick airfoil always has the smallest lift compared to thinner airfoils with the same camber. The effect of lift mitigation by thickness increase is most prominent for strong cambered airfoils ($m = 0.035$; $\Delta c_L = 0.03$). It diminishes for only slightly cambered airfoils ($m = 0.015$; $\Delta c_L = 0.01$).

Taking a look at the c_L versus c_D plots depicted in Figure 4.9 (b) the picture changes a little bit. While the main driver for the lift coefficient c_L is the airfoils camber, the drag coefficient c_D is primary influenced by the relative airfoil thickness t/l_c. It is obvious, that thicker airfoils tend to produce more drag than thinner ones because of their bigger cross-section perpendicular to the flow yields more pressure drag (or form drag). Generally speaking, two effects govern the aerodynamic efficiency of the airfoils determined by the L-over-D ratio (ratio c_L/c_D, or sometimes glide ratio). The efficiency is thereby increased by either increasing camber or decreasing thickness. This kind of trivial finding will become more interesting when interpreting the aeroacoustic performance of the airfoils.

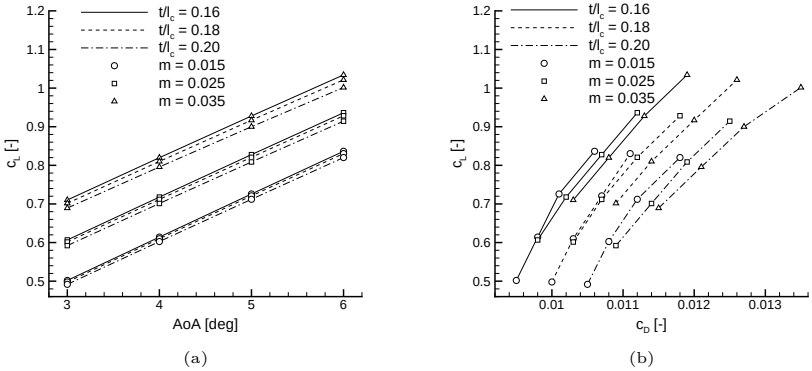

Figure 4.9: Aerodynamic coefficients for the nine different airfoils for fixed laminar turbulent transition; (a) lift coefficient c_L vs. angle of attack α; (b) lift coefficient c_L vs. drag coefficient c_D.

To analyze the effect of natural laminar turbulent transition, the fixed transition model was replaced by the $\gamma - Re_\theta$ transition model. The severe influence of the transition on the performance of the airfoils is shown in Figure 4.10 (a) indicated by the red lines. While the lift coefficient is almost untouched by the transition, the drag coefficient is nearly reduced by 50 %. To evaluate the transition location, the local wall friction coefficient was extracted from the CFD data. Thereby, the position where it rapidly increases indicates the transition from laminar to turbulent boundary layer flow. The so calculated transition location is plotted in Figure 4.10 (b) for all airfoils and different angles of attack. It can be observed that for increasing angles of attack the transition position moves forward on the suction side (due to the increasing adverse pressure gradient) and backward on the pressure side. Thinner airfoils show longer laminar running lengths on the pressure side. The transition on the suction side is more affected by an increase of the angle of attack, especially for low cambered airfoils, which show the strongest decrease of laminar running length.

The main influence of the longer laminar running length and the thinner boundary layers in the natural transition flow regime is the massive reduction in drag by nearly 50 %. In terms of aerodynamic efficiency measured by the lift to drag ratio, this leads to a much better performance of the airfoils, if a laminar boundary layer flow can be maintained as long as possible. The transition location is affected by the turbulence of the incoming flow and surface quality of the airfoils. Unfortunately, under real operation conditions in a wind turbine rotor blade, both parameters are hard to predict in advance. Among others, the turbulence depends on the wind farm location, the terrain, obstacles in the upwind position of the rotor (e.g. other turbines) and meteorological effects. The smoothness of the blade surface is influenced by the production quality, surface erosion, surface repairing and mainly the adherence of dirt and insects on the blades leading-edge. Thus, it is nearly impossible to predict a set of aerodynamic coefficients which will perfectly match expected

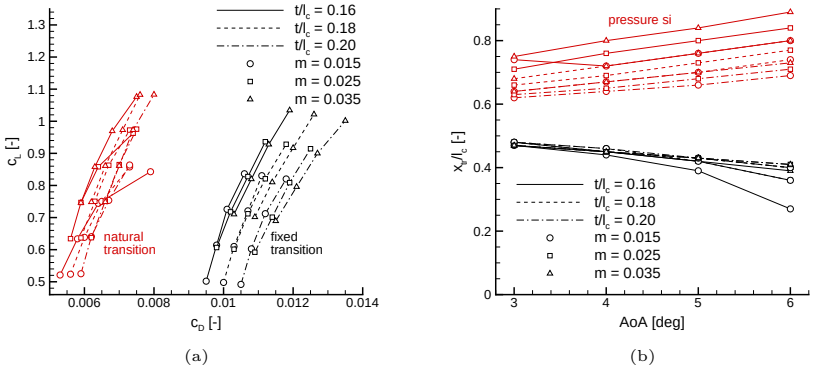

(a) (b)

Figure 4.10: Aerodynamic performance for fixed and natural transition; (a) lift coefficient c_L vs. drag coefficient c_D; (b) location of the transition from laminar to turbulent flow for the natural transition simulations distinguished for pressure and suction side.

values in real operation. Alternatively, the two settings described above (fixed transition and natural transition) can be seen as a best and worst case performance scenario, where the truth lies somewhere in between. This aspect will further be discussed in the context of airfoil selection. It not only influences the aerodynamic behavior, but also the acoustic emissions.

4.3.2 Aerodynamics and Acoustics

While the aerodynamic results show the expected properties and relations for two-dimensional airfoil flow simulations, the aeroacoustic analysis yields a clearer insight into the TBL-TEN problem. Moreover, by having both - aerodynamic and aeroacoustic results - it is now possible to evaluate modifications on both scales and do the trade-off between the two categories.

The CAA analysis is done in the two-dimensional domain around the airfoil. An exemplary snap shot of the non-dimensionalized fluctuating sound pressure field for the baseline airfoil is shown in Figure 4.11 (a). Again, the cardioid directivity of the main radiation, as well as dipole like behavior of the trailing-edge noise radiation, can be observed. For each positive sound pressure signal traveling in the upper half plane, there is a respective negative signal traveling in the lower half plane. In front of the leading-edge and behind the trailing-edge these wave cancel out each other, resulting in zones with less or almost no noise impact directly in the direction of the airfoil chord.

The fluctuating sound pressure p' is recorded over time. For all further investigations the microphone position directly below the trailing-edge ($x/l_c = 1$, $y/l_c = -2.5$) is chosen as the representative microphone position for evaluations. Figure 4.11 (b) shows one-third-octave band spectra processed from the recorded time dependent sound pressure

of the baseline airfoil at this reference position. Four curves are shown, one for each angle of attack. Corrections due to the used CAA method and 2D to 3D scaling are applied (Equation 2.61). Note, that the corrections are independent of the frequency and only yield a constant shift in sound pressure levels. Relative differences between the respective airfoils are not influenced. The given values represent scaled data (for better comparison) for an airfoil of 1 m span at a microphone distance of 1 m directly below the trailing-edge($\Theta = 270\,^\circ$ referring to Figure 2.5).

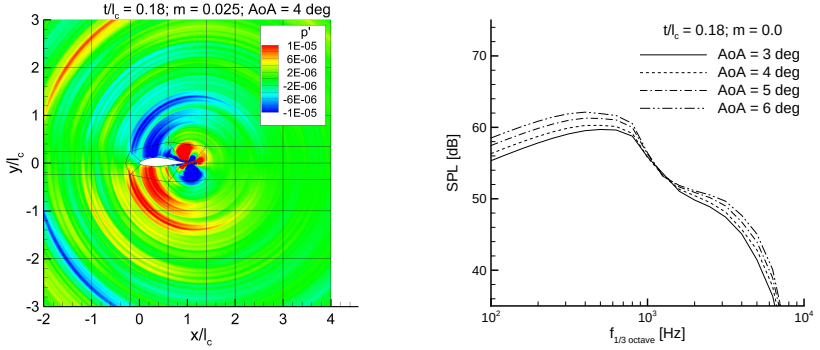

Figure 4.11: Exemplary aeroacoustic results generated by a CAA simulation conducted with PIANO; (a) instantaneous plot of fluctuating sound pressure field around the airfoil; (b) resulting one-third-octave band spectra at microphone directly below the trailing-edge.

A systematic angle of attack influence on the trailing-edge noise can be seen. Each spectrum possesses two peaks, indicated by two humps in the shape of the graphs. The low-frequency peak around $f \approx 350\,\text{Hz}$ is increased and shifted to lower frequencies, while the second (lower) high-frequency peak around $f \approx 2500\,\text{Hz}$ is also increased but shifted in the other direction towards higher frequencies for increasing angles of attack. The cause for this phenomenon is found to be the independent contributions emanating from the airfoil's upper and lower side. Similar to the detailed analysis given in Figure 4.4 for the NACA0012 airfoil. The low-frequency peak is thereby caused by the suction side boundary layer and the high frequency peak by the thinner pressure side BL. Changing the angle of attack influences these boundary layers and is responsible for the different spectra.

For further data evaluation the overall sound pressure level $L_{p(OA)}$ (or OASPL) can be calculated from the single one-third-octave band levels $L_{p(1/3)_i}$ as:

$$L_{p(OA)} = 10 \log_{10} \left(\sum_{i=1}^{n} \frac{10^{L_{p(1/3)_i}}}{10} \right) . \tag{4.6}$$

Using the equation stated above it is now possible to reduce all acoustic information from the CAA simulation into one value. The overall sound pressure level at the microphone position below the trailing-edge[6]. For the angle of attack variation of the baseline airfoil the overall levels increase from $L_{p(OA)} = 69.6\,\text{dB}$ for $\alpha = 3\,^\circ$ to $L_{p(OA)} = 72.1\,\text{dB}$ for $\alpha = 6\,^\circ$. The higher lift production of the airfoil is purchased by higher sound emission.

The concept of reducing all acoustic information into one value, together with an aerodynamic performance indicator, yields a clearer overview. So, multiple airfoils can be compared against each other. For this comparison it is not useful to investigate sound pressure levels for the airfoils at the same angles of attack, as c_L and c_D are changed according to the AoA changes. A fair comparison of aeroacoustics can only be done if the lift-to-drag ratio or at least the lift is viewed in combination with the overall sound pressure levels. An exemplary question for the investigation could be: Which airfoil produces the minimum TBL-TEN signal for a given ratio of c_L/c_D or for a given c_L respectively? Thus, the acoustic performance can be incorporated in the airfoil selection process.

Fixed Transition

Figure 4.12 (a) shows overall sound pressure levels compared to the glide ratio c_L/c_D for all airfoils under different angles of attack. The transition is forced and fixed to the positions given in Section 4.2.2. Each point indicates one angle of attack. The angles increase from bottom left to top right in the plots. For the chosen flow conditions all airfoils can be operated in a c_L/c_D range between 50 and 90 by adjusting the angle of attack. These aerodynamic performances can be achieved with different noise emissions ranging between 68 dB and 74 dB. It seems, that the airfoil thickness is the main driver for noise emission. While the thin airfoils (indicated by the solid lines; $t/l_c = 0.16$) show the smallest overall levels, the thick airfoils (indicated by the dashed-dotted lines; $t/l_c = 0.20$) show levels which are 3-4 dB higher. The values of the medium thick airfoils ($t/l_c = 0.18$, dashed lines) are in between the other thicknesses. The variation in airfoil camber indicates low noise emissions for airfoils with less camber (indicated by circles). The L-over-D ratio shows no clear trend for the camber variation. For the thick and medium thick airfoils, the highest L-over-D ratios are reached with the low cambered geometry, while for the thin airfoils, the low cambered geometries show the smallest glide ratio. As an overall trend it can be observed, that an increase of the L-over-D ratio is always associated with higher noise emissions. For the desired parameter variation of camber and thickness, the airfoil with minimum thickness ($t/l_c = 0.16$) and maximum camber ($m = 0.035$) shows the best performance in terms of L-over-D ratio and overall sound pressure levels.

If one compares overall sound pressure levels against lift coefficient (shown in Figure 4.12 (b)), the range of $L_{p(OA)}$ variations for a certain lift value shortens a bit to 2-3 dB, which is due to the fact that the variation in c_L/c_D ratio is mainly influenced by the changing drag coefficient of the airfoils (see Figure 4.9 (b)). Nevertheless, it is still possible to produce one and the same lift coefficient with different noise emissions. Also in this breakdown the

[6] Note, that all spectral information is lost and the overall value can only be interpreted as an average indication for the airfoil's acoustic performance. Moreover, frequency depend weighting (e.g. A-weighting) needs to be considered for relevant real life cases. Therefore, more geometric data from the real flow problem, especially the chord length must be known in order to correctly scale the one-third-octave-band spectrum of the trailing-edge noise and thereafter apply the weighting function.

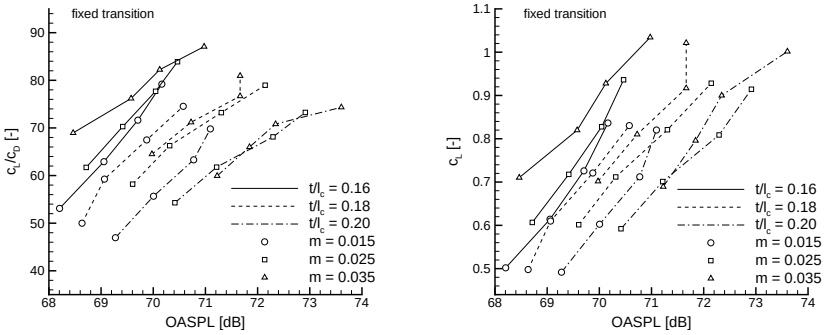

Figure 4.12: Overall sound pressure levels $L_{p(OA)}$ for different geometries and varying angles of attack compared to aerodynamic parameters for fixed laminar turbulent transition; (a) lift-to-drag ratio c_L/c_D; (b) lift coefficient c_L.

thin, strong cambered airfoil shows the best performance. Again, thinner airfoils show a better performance than thicker ones. For camber variations no clear trend concerning the lift coefficient can be identified.

The evaluation shows, that certain L-over-D ratios or lift values can be reached with different noise emissions of the airfoils. Thus, the airfoil geometry is a crucial influence parameter for the trailing-edge noise problem and the chosen simulation method reveals a tool to gain aeroacoustic performance in terms of noise reduction without too much influence on the aerodynamic characteristics. Note, that the chosen geometry variation strategy represents only one systematic approach to vary the geometry within certain very small limits. Thus, it cannot be guaranteed that all relevant geometric parameters are identified. Nevertheless, even with the chosen variation the possible noise emission range for a fixed aerodynamic performance is in the range of several decibels. Thus, there is a high potential for noise reduction which can be investigated by the chosen hybrid procedure.

Natural Transition

So far, only the fixed transition flow regime was analyzed. Figure 4.13 depicts the investigation expanded to the natural transition cases. Again, plots for $L_{p(OA)}$ versus lift-to-drag ratio and versus lift coefficient are shown in Figure 4.13 (a) and (b). For comparison, the fixed transition results are added to the plots (black lines). The natural transition results are indicated by the red lines. The first, most obvious finding is, that a much higher aerodynamic performance (indicated by c_L/c_D ratio) is achieved. Moreover, also the noise emission is reduced by the natural transition flow regime. This can be explained with the much lower drag coefficients due to the longer laminar running

length of the boundary layer flow (see Figure 4.10). While the lift is almost the same for the natural transition flow situation, drag is considerably reduced which results in c_L/c_D ratio range of 90 to 140 instead of 50 to 90 for the turbulent flow. Moreover, due to thinner boundary layers caused by the later transition the trailing-edge noise signal is reduced in the magnitude of 3 dB. So, airfoils sensitive to transition location changes (airfoils designed for long natural laminar flow) are prone to noise increase by an upstream transition movement. Looking at the baseline airfoil ($t/l_c = 0.18$, $m = 0.025$) at an angle of attack of $\alpha = 4\,^\circ$ the L-over-D ratio is reduced by 44.6 % and the overall sound pressure level is increased by 4.2 dB due to the forced transition. Especially in practical wind turbine operation, this transition forcing can be caused by surface contamination with dust or insect impacts.

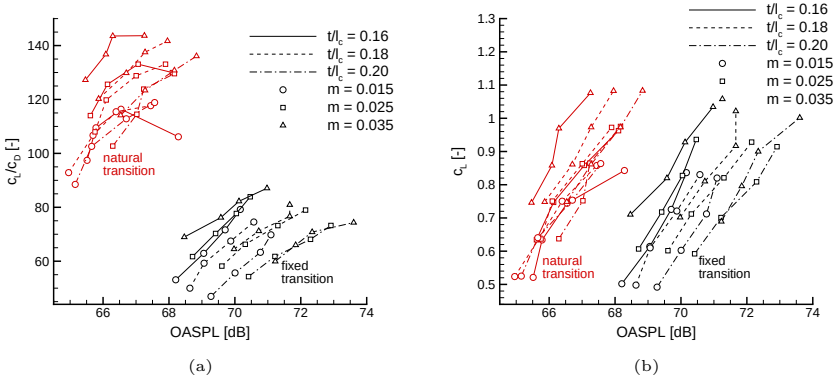

Figure 4.13: Overall sound pressure levels $L_{p(OA)}$ for different geometries and varying angles of attack compared to aerodynamic parameters for natural laminar turbulent transition; (a) lift-to-drag ratio c_L/c_D; (b) lift coefficient c_L.

If the overall sound pressure levels are evaluated against the lift coefficients (shown in Figure 4.13 (b)), one can only see the gain in noise emissions, as the main aerodynamic advantage of the natural laminar boundary layer comes from the reduction in drag. The lift values are almost untouched by the transition.

Even under laminar flow conditions, the thin strong cambered airfoil ($t/l_c = 0.16$, $m = 0.035$) shows the best performance, but a strong dependence on camber reduction can be observed. This can be explained by the fact, that the thin airfoil exhibits a pronounced decrease in laminar running length with angle of attack increase, which is additionally amplified by increasing camber (see Figure 4.10 (b)). Thereby two mechanisms come into play. First, the aerodynamic performance in terms of c_L/c_D ratio is reduced. Second, the thicker boundary layers due to the shorter laminar running length increase the TBL-TEN signal. Generally speaking, the thin airfoils are more critical towards transition locations and tend to lose their good performance faster. Trends seen in the plot of c_L versus $L_{p(OA)}$ indicate that the range of possible $L_{p(OA)}$ values for generating a certain amount

of lift is smaller for natural transition than for fixed transition. But still, a 2 dB difference for the varying geometries can be seen.

The strong dependency of the airfoil performance on the transition locations urges the need for a precise analysis of the two different flow regimes. While the natural transition case can be interpreted as the best possible airfoil performance (e.g. for a perfectly manufactured new rotor blade with smooth surface, no disturbances or dirt adherence), the forced transition at the airfoil nose represents the worst case scenario (contaminated, damaged or eroded leading-edge surface of a rotor blade after many years of operation). The investigation showed, that this performance range is not only important for the blade aerodynamics, but also has a severe influence on the acoustic emissions.

4.4 Relationship between Boundary Layer Values and Noise

To better understand the driving parameters for the trailing-edge issue a deeper investigation of the simulation data of the modified DU airfoils is conducted. Therefore, different cases are chosen and distinct parameters are compared against each other. The vast amount of available simulation data from the CFD and CAA simulation is a clear advantage in this case. First, cases with the same glide ratio c_L/c_D but different noise emissions are compared. Thereafter, the same analysis is done with cases with the same noise emission but different aerodynamic performance. To reduce the complexity, only cases with fixed laminar turbulent transition locations are investigated. It is argued, that the aerodynamic effects in the boundary layer which are supposed to drive the noise generation process at the trailing-edge are the same in both cases.

4.4.1 Cases with same L-over-D Ratio and different OASPL

Three cases with the same aerodynamic performance (in terms of c_L/c_D ratio) but different overall sound pressure levels are chosen from the simulation results. As the angle of attack is only varied in discrete steps, perfect matching of c_L/c_D ratios is not possible. Nevertheless, the cases shown in Table 4.2 all lie closely together with c_L/c_D values around 75. Besides that, the overall sound pressure levels alternate between 69.6 dB and 73.6 dB. The thinnest airfoil has the least noise emission while the thickest airfoil shows the utmost values. To reach the same glide ratio as the thin airfoil it has to operate at a higher angle of attack.

Table 4.2: Test cases with matching c_L/c_D ratio and different $L_{p(OA)}$ values (fixed transition only).

t/l_c	m	α	c_L	c_D	c_L/c_D	$L_{p(OA)}$
[−]	[−]	[°]	[−]	[−]	[−]	[dB]
0.16	0.035	4	0.820	0.0108	76.2	69.6
0.18	0.035	5	0.917	0.0120	76.7	71.7
0.20	0.035	6	1.002	0.0135	74.3	73.6

Figure 4.14 (a) depicts one-third-octave band SPL spectra for the three cases. According to the diagram, deviation can only be found in the low frequency range below 1 kHz. The highest levels are generated for the thick airfoil ($t/l_c = 0.20$) at a peak frequency around $f = 200$ Hz. For the medium thick airfoil ($t/l_c = 0.18$) the maximum sound pressure levels are about 2 dB lower and the peak frequency is increased to $f = 400$ Hz. The low frequency levels of the thin airfoil ($t/l_c = 0.16$) are again lower (about 4 dB compared to the thick airfoil) and the peak frequency is shifted further upward to $f = 600$ Hz. For all airfoils, the low frequency levels (below 1 kHz) are higher than in the high frequency range and as such will dominate the logarithmic addition according to Equation 4.6 to calculate the overall sound pressure level. Thus, the low frequency differences can directly be found in the resulting OASPL differences of the three cases.

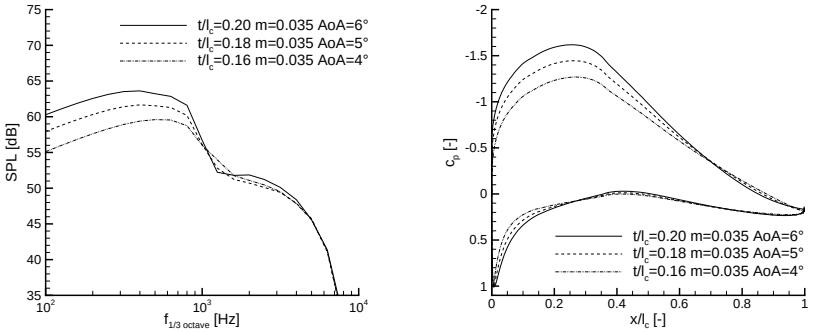

Figure 4.14: Comparison of 3 cases with the same c_L/c_D ratio and different $L_{p(OA)}$ values; (a) one-third-octave band spectra at microphone position directly below the trailing-edge; (b) pressure coefficient c_p for pressure and suction side.

As demonstrated in Section 4.1.3 trailing-edge sound contributions from suction and pressure side can be treated separately and as such are responsible for the different parts of the spectrum. For airfoils which produce positive lift (inclined to the flow or cambered), the thicker suction side boundary layer accounts for the low frequency part and the thinner pressure side BL for the high frequency part. Looking at the pressure distribution depicted in Figure 4.14 (b), it can clearly be seen, that the graphs are nearly identical for the pressure side but show differences at the suction side (mainly due to higher angles of attack to compensate the drag increase with increasing airfoil thickness). Consequently, differences in the suction side flow are responsible for the different low frequency parts of the spectra. No variation occurs in the high frequency range, which is in good agreement with the identical c_p distributions at the pressure side.

For further analysis, the boundary layer profiles of velocity v_x and turbulence kinetic energy k_t are shown in Figure 4.15 (a) and (b). The data is sampled along a chord-perpendicular line located directly at the trailing-edge ($x/l_c = 1$). A wider boundary

layer with higher k_t values can be observed for the thicker airfoil at the suction side. The boundary layer thickness δ can be estimated from the velocity profile as the point where the gradient reduces to zero[7]. Compared to the thick airfoil, the boundary layer of the thin airfoil is reduced by 30 % from $y/l_c = 0.065$ to $y/l_c = 0.045$. Correspondingly, the thick airfoil shows a higher peak in the TKE values at the suction side. The peak is also located further away from the trailing-edge. The shapes of the TKE profiles on the suction side look identical. Their actual size scales with the boundary layer thickness and corresponds to the order of the maximum SPL values in the one-third-octave band spectra. High turbulence and wide boundary layers cause the higher noise emissions in the low frequency range, which is the dominant part of the TBL-TEN spectrum. From a merely acoustic point of view, it does make sense to find airfoils which show thin boundary layers at their desired point of operation. Comparing Figure 4.14 (b) and Figure 4.15 this can be achieved by a low adverse pressure gradient for the suction side pressure regain. As the main function of the airfoils is lift production, this fact is somehow intrinsic in the problem statement. Lift cannot be produced without trailing-edge noise, but with elaborate choice of geometry and point of operation a reduction is possible. One major finding is, that by evaluating the TKE profile at the trailing-edge (an information that can be generated by a rather simple CFD simulation) it is possible to make an assessment for the acoustic performance of the airfoil. This bears the possibility to compare airfoils against each other based on their turbulence production at the suction side to make a relative benchmark in terms of TBL-TEN. Clearly, all considerations need to be evaluated also against concurring branches in the rotor blade design process (e.g. structural mechanics or production aspects).

4.4.2 Cases with different L-over-D Ratio and same OASPL

In contrast to the previous subsection, three different cases with equal noise emissions but different aerodynamic performances are juxtaposed. Representative values can be found in Table 4.3. Again, three airfoils varying in thickness and operating under different angles are investigated. Thereby, the thinnest airfoil has the highest angle of attack, while the thickest airfoil has the lowest. The overall sound pressure levels nearly match with values slightly below 70.5 dB. The higher lift coefficient together with the higher angle of attack results in a better c_L/c_D ratio of 83.9 for the thin airfoil compared to 54.3 for the thick airfoil.

Figure 4.16 (a) shows the one-third-octave band SPL spectra for the three different cases. It can be observed that all three spectra show the same levels in the low frequency range below 1 kHz. Slight differences can only be seen in the high frequency range. As the OASPL is dominated by the highest values in the spectrum, all OASPL values for the three cases match. The difference in the high frequencies has such a minor contribution that it is not important here. Again, c_p distributions for the three cases are analyzed and depicted in Figure 4.16 (b). For the suction side the graphs of the distributions are nearly identical in the pressure regain region downstream of $x/l_c = 0.4$. Only upstream of

[7] Note, that the determination of boundary layer thicknesses with the definition as the position where 99 % of the free stream velocity v_∞ is reached is not applicable for boundary layers with pressure gradients and accelerating and decelerating flow velocities. One suggested definition for the BL thickness in this cases can be found in Reference [73]. Here, the inflection point of the velocity profile is chosen for determination of the boundary layer thickness. The same procedure is used for the calculation of the δ values, stated in this work.

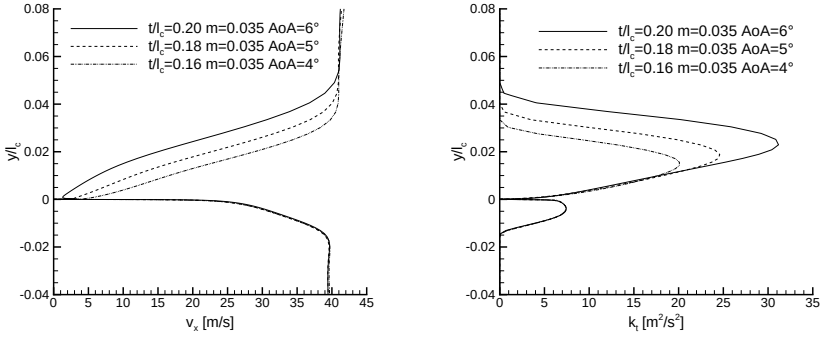

(a) (b)

Figure 4.15: Comparison of 3 cases with the same c_L/c_D ratio and different $L_{p(OA)}$ values directly at the trailing-edge; (a) velocity distribution; (b) turbulence kinetic energy distribution.

Table 4.3: Test cases with matching OASPL ($L_{p(OA)}$) values and different c_L/c_D ratio (fixed transition only).

t/l_c	m	α	c_L	c_D	c_L/c_D	$L_{p(OA)}$
$[-]$	$[-]$	$[°]$	$[-]$	$[-]$	$[-]$	$[dB]$
0.16	0.025	6	0.936	0.0112	83.9	70.5
0.18	0.025	4	0.712	0.0107	66.3	70.4
0.20	0.025	3	0.592	0.0109	54.3	70.5

$x/l_c = 0.4$ more suction is generated by the thin stronger inclined airfoil. As a consequence more lift is produced. Comparing the pressure side distributions, it can be seen, that also here the thin airfoil shows the highest values and, as such, the strongest lift production. The matching c_p distributions in the aft part of the suction side indicate similar boundary layer values. This explains the similar spectra in this region and finally the matching OASPL values. The hypothesis becomes clearer with a closer look at the boundary layer distributions.

Figures 4.17 (a) and (b) depict the distributions of flow velocity v_x and turbulence kinetic energy k_t across the boundary layer. It can be examined, that for the suction side the profiles for velocity as well as the kinetic energy profiles are nearly identical for all three cases. Hence, the same amount of TBL-TEN is present in all three setups. This fact further underlines the argumentation that the suction side BL is mainly responsible for the TBL-TEN issue. The minor differences seen in the pressure side distributions account for the mismatch in the (not so important) high frequency range of the spectrum. Interestingly, the behavior for the pressure side is somehow vice-versa to the one of the suction side. For example, the higher TKE levels lead to the least high frequent noise

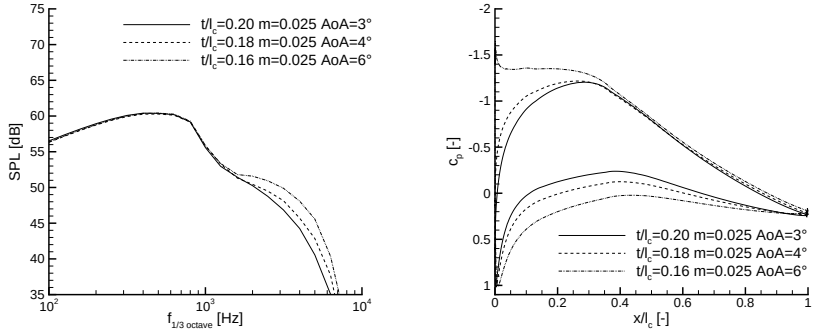

(a) (b)

Figure 4.16: Comparison of 3 cases with different c_L/c_D ratio and the same $L_{p(OA)}$ values; (a) one-third-octave band spectra at microphone position directly below the trailing-edge; (b) pressure coefficient c_p for pressure and suction side.

emission (solid line), while the lowest TKE profile (dashed double dotted line) has the utmost influence on the high frequency noise and shows the highest values. It seems, that flow speed and distance from the trailing-edge become more important for the trailing-edge noise caused by the thin pressure side boundary layer, as the loudest airfoil shows the highest velocities close to the TE (thinnest boundary layer). Also, slightly higher TKE levels are present closer to the wall. This behavior could not be observed for the suction side.

As the high frequency part of the spectrum generated by the pressure side trailing-edge flow shows an influence on the spectra which is in values much lower than the suction side contribution, the thin strong cambered airfoil can still be considered best in case of noise and aerodynamic efficiency. Generating lift either at the pressure side or respectively in the forward part of the suction side is the acoustically favorable method. Doing this, low noise emission can be achieved with only minor aerodynamic drawbacks. The main focus should thereby lie on the pressure regain of the suction side flow, as the turbulent kinetic energy and the velocity profiles which are generated here are responsible for low frequency trailing-edge noise contribution which is dominating the overall levels.

4.4.3 Further Data Analysis

For further evaluations, the automized simulation approach is extended to other available airfoils. One airfoil with 18 % thickness, the NACA64618 and three airfoils with 15 % thickness FX77-W-153, FX79-W-151[8] and ROH15[9] are chosen for the subsequent

[8] Named after their inventor Franz Xaver Wortmann. The 'W' indicates their use for wind turbine applications.

[9] Developed by Claas-Hinrik Rohardt from DLR

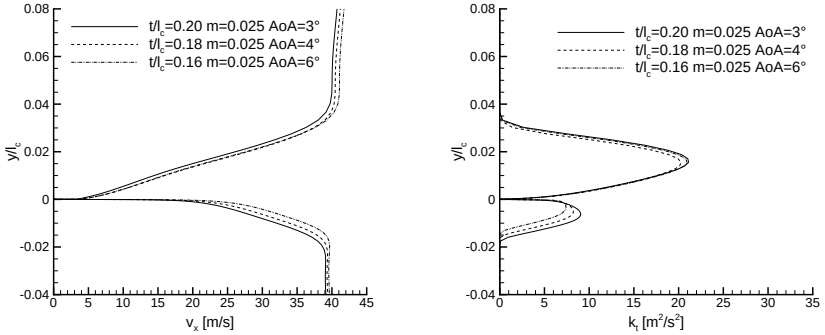

(a) (b)

Figure 4.17: Comparison of 3 cases with different c_L/c_D ratio and the same $L_{p(OA)}$ values directly at the trailing-edge; (a) velocity distribution; (b) turbulence kinetic energy distribution.

simulations. All airfoils are applicable for the use in the outer part of wind turbine rotor blades. The corresponding geometries are depicted in Figure A.6 in Section A.7 of the Appendix. Simulations are conducted for a Reynolds number of $Re = 3 \cdot 10^6$, a Mach number of $M = 0.2$ and a chord length of $l_c = 0.65\,\text{m}$. Fixed and natural transition performance are investigated. For the fixed transition cases the transition locations is set at $x/l_c = 0.05$ on pressure and suction side respectively. For comparison, the simulated sound pressure levels are scaled to a chord length of 1 m and a microphone distance of 1 m. Standard ambient conditions are chosen and the angle of attack is varied between four and eight degrees in steps of one degree to achieve lift coefficients around $c_L = 1.0$.

Analogously to Section 4.3.2 the tradeoff of aerodynamic performance (in terms of L-over-D ratio c_L/c_D) and noise emission (in terms of overall sound pressure level $L_{p(OA)}$) is depicted in Figure 4.18 (a). For the fixed transition setting c_L/c_D ratios between $c_L/c_D = 60$ and $c_L/c_D = 80$ can be reached. A natural laminar turbulent transition yields higher ratios between $c_L/c_D = 100$ and $c_L/c_D = 180$ depending on the airfoil geometry and angle of attack. The dependence of the emitted noise on the airfoil shape and angle of attack can clearly be seen for all airfoils. The ROH15 airfoil has the highest glide ratio in both transition cases but is highly influenced by its transition location. For the natural transition setting it can be observed, that it tends to loose it's high performance faster than the other airfoils with increasing angle of attack due to the increasing drag. Contrary, the FX77 airfoil shows only smaller noise increase with increasing AoA and no loss in L-over-D ratio under natural transition operation. This means, that the ROH15 might be the better airfoil in both noise and aerodynamics but only at a very precise operating point. For the application in a wind turbine rotor blade this 'off-design' performance needs to be considered. The operating point might not always be at the desired optimum (e.g. due to influence of wind speed changes, gusts, or the atmospheric boundary

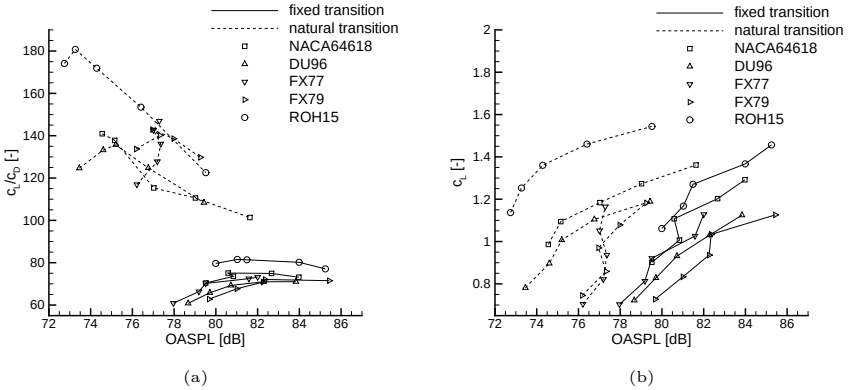

Figure 4.18: Overall sound pressure levels $L_{p(OA)}$ for different airfoils and varying angles of attack compared to aerodynamic parameters for fixed and natural laminar turbulent transition; (a) lift-to-drag ratio c_L/c_D; (b) lift coefficient c_L.

layer). Comparing the performance of the 15 % thick ROH15 with the 18 % NACA64618 a discrepancy in aerodynamic performance of around 20 % can be found while the noise difference is only 1 dB, depending on the point of operation. Consequently, a much higher structural strength could be achieved with the NACA airfoil instead of the ROH airfoil with only minor drawbacks in the acoustic performance and a manageable loss of aerodynamic performance (refer to Section 5.2.3 for a more precise analysis of the L-over-D ratio influence on the rotor blade performance).

Disregarding the effect of airfoil drag, the simulation results for the lift coefficient and the sound pressure level are compared in Figure 4.18 (b). Again, an average increase around 4 dB due to the forced transition can be observed while the lift coefficients are nearly unchanged, ranging between $c_L = 0.8$ and $c_L = 1.5$ depending on the angle of attack. Best results are achieved with the ROH15 airfoil, especially in the natural transition setting due to its low adverse pressure gradient at the second half of the suction side combined with the a thin boundary layer and low TKE values. Under fixed transition conditions, the thicker NACA64618 airfoil shows almost identical performance as the ROH. Again, the FX airfoils show a steady noise emission for increasing lift in the natural transition setting.

The airfoil analysis discussed above mainly shows the capability of the hybrid CFD CAA method to work as a fast and reliable prediction approach for the evaluation of different airfoils. However, the computation time for CAA step is with 16 hours still relatively high, especially if no multi-CPU, high performance cluster is available. A solution, where a noise prediction could be done only with the information gained from the CFD analysis would (if possible) yield a much faster approach. It would also increase the amount of analyzed geometries within an airfoil design process. Moreover, if an extension towards an optimization procedure is needed a reliable relation of CFD parameters and overall noise emission without the computationally expensive CAA simulation might be a feasible ap-

proach. To find this relation a total of 192 individual conducted noise simulations[10] of the hybrid method are chosen. The boundary layer values at the trailing-edge are automatically extracted from the CFD data and significant parameters are calculated. Together with the acoustic data from the CAA analysis it is tried to find useful correlations.

Among others, from the TKE distributions at the trailing-edge (e.g. see Figure 4.15) the maximum value $k_{\mathrm{t,max}}$ and its distance from the trailing-edge $y(k_{\mathrm{t,max}})$ are extracted. Moreover, the TKE distributions are integrated over the height of the boundary layer which yields the value $k_{\mathrm{t,\ int}}$. As it was shown in the previous subsections the turbulence in the suction side boundary layer is mainly responsible for the trailing-edge noise signal for airfoils under normal operation conditions (positive angle of attack below stall). The best coherence could thus be found for these values. They are shown in Figure 4.19 (a) and (b).

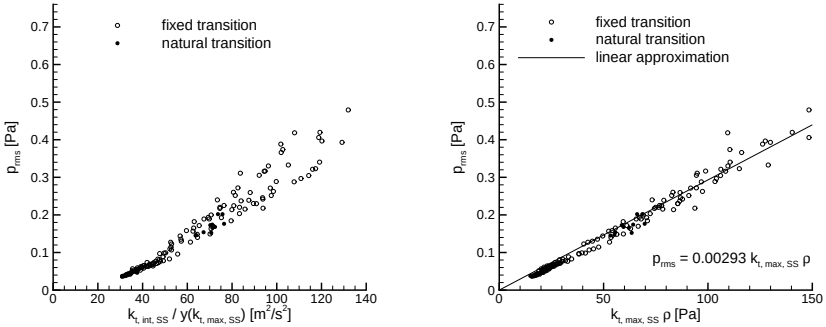

Figure 4.19: Correlation of boundary layer values extracted from the CFD simulations to acoustic pressure gained from the CAA simulations for several airfoils (192 individual simulations); (a) TKE distribution integrated over the suction side BL divided by the location of the maximum TKE at the suction side $k_{\mathrm{t,\ int,\ SS}}/y(k_{\mathrm{t,max,\ SS}})$; (b) maximum TKE value multiplied by density $k_{\mathrm{t,max,\ SS}}\rho$.

The acoustic pressure is calculated from the overall sound pressure levels ($p = 10^{L_p/20} p_{\mathrm{ref}}$ with $p_{\mathrm{ref}} = 2 \cdot 10^{-5}$ Pa) and compared to the quotient of the integral TKE value and the position of the TKE maximum at the suction side (SS) in Figure 4.19 (a). A clear, almost linear alignment of the values for all 192 simulations can be observed. This reveals two major observations. First, the emitted noise scales with the integrated turbulence kinetic energy and as such with the boundary layer thickness over which it is integrated as well as the actual k_t values along the distance from the wall. Second, the noise scales with the inverse of the distance of the maximum (peak) TKE value. Thus, airfoils where $k_{\mathrm{t,max,\ SS}}$ is situated close to the trailing-edge will produce more TBL-TEN. Note, that this finding

[10] Simulations include the DU geometry variations as well as several other airfoils and different operating conditions (e.g. AoA, Mach and Reynolds number, transition setting).

is independent of the applied transition setting. The following relation can be formulated from the results:

$$p \sim \frac{k_{\mathrm{t,\ int,\ SS}}}{y(k_{\mathrm{t,max,\ SS}})}. \tag{4.7}$$

An even more significant correlation can be found if the acoustic pressure is plotted against the maximum TKE multiplied by the density. This is shown in Figure 4.19 (b). The clear, linear relationship between the parameters is indicated by the solid line with the slope 0.00293. This indicates, that the main driving parameter for the trailing-edge noise is clearly the maximum value of the turbulence kinetic energy in the suction side boundary layer at the trailing-edge. Further analysis revealed, that if $k_{\mathrm{t,max,\ SS}}\rho$ is divided by the ambient speed of sound c_∞ the proportionality changes to the value of one (see Figure 4.20). This yields the following relation for an estimation of the acoustic pressure:

$$p \simeq \frac{k_{\mathrm{t,max,\ SS}} \cdot \rho}{c_\infty} \left[\frac{m}{s}\right]. \tag{4.8}$$

Or for the overall sound pressure level:

$$L_{p(OA)} = 20 \log \left(\frac{\frac{k_{\mathrm{t,max,\ SS}} \cdot \rho}{c_\infty} \left[\frac{m}{s}\right]}{p_{\mathrm{ref}}} \right). \tag{4.9}$$

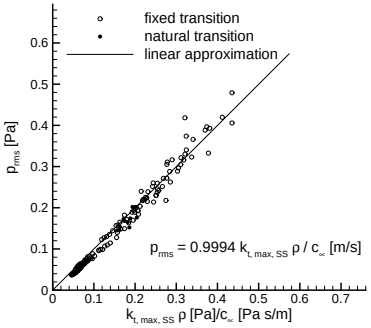

Figure 4.20: Correlation of maximum turbulence kinetic energy in the suction side boundary layer and acoustic pressure scaled with the speed of sound c_∞ for several airfoils (192 individual simulations).

Unfortunately, the unit of a velocity (m/s) had to be added in order to yield the correct physical units of the resulting sound pressure. Nevertheless, Equation 4.9 allows to previously predict the CAA results. For an acoustic airfoil optimization it could be used as a first noise indicator without conducting any CAA simulation. For the 192 simulations plotted in Figure 4.20 the average error between the predicted acoustic pressure and the one simulated by the CAA method is 10 % or in terms of decibel 0.8 dB for the overall sound pressure level. Considering the variety of airfoil geometries and flow conditions

which are analyzed, this is a fairly accurate estimation. It can be used as a guideline for the design of new, low-noise airfoils to filter the available CFD data and thereafter decide which settings should be further investigated by the means of CAA simulations.

4.5 Strategy for Low Noise Airfoils

As a result of the aeroacoustic analysis conclusions for the desired features of low noise airfoils may be drawn. These guidelines can later be used to achieve a noise mitigation in the airfoil design phase. Nevertheless, competing requirements from aerodynamics and structural design still need to be considered. An improvement of one feature will often result in a drawback for another. The tradeoff of the requirements is thus crucial to obtain a good overall design. The subsequent list highlights the major points for a low noise airfoil design.

- **Region of Lift Generation:** More lift should be generated at the pressure side. The relatively thin boundary layer here shows only minor influence on the overall sound emission of the airfoil (see Figure 4.16). This could be done by moving the airfoil's maximum thickness forward which creates a higher flow acceleration beyond the nose. Additionally a more concave shape (rear loading) could be introduced at the back part of the pressure side. Also, the lift generation at the suction side should be concentrated more on the forward part of the airfoil to enhance the moderate pressure regain (see next point).
- **Pressure Regain at the Suction Side:** In Figures 4.14 and 4.15 it is shown that the pressure regain at the aft part of the suction side is mainly responsible for the boundary layer thickness and the turbulence kinetic energy levels. A shallower pressure regain with a lower absolute minimum c_p value is thus favorable. Of course, this also decreases the generated lift force (tradeoff).
- **Reduction of Turbulence Kinetic Energy in the Boundary Layer:** A distinct scaling of the OASPL values of the tested airfoils with the TKE distribution and its maximum levels is shown in Figures 4.19 and 4.20. A reduction of TKE will thus directly lead to a noise reduction. Geometry changes of the aft part of the suction side (e.g. an inverse suction side rear loading) should be considered to achieve a TKE reduction. Possible negative side effects (flow separation, high negative lift production at negative AoAs) need to be closely monitored.
- **Thin Airfoil Design:** For a better aerodynamic performance (mainly due to the reduced form (shape) drag) in combination with low TKE levels in the boundary layer, thinner airfoils should be preferred. Clearly, this decision is often governed by structural issues and it is not always possible to reduce the relative thickness. It could be argued, that with the achievable noise benefit the higher price for stiffer materials (e.g. carbon fiber) is justified which might compensate the structural drawback of the thinner geometry.
- **Long laminar Flow:** Airfoils designed for laminar flow have two main advantages. While the L-over-D ratio is almost doubled, the overall noise is reduced by around 3 dB compared to their fully turbulent performance (e.g. see Figure 4.13). The use of this advantages seems obvious, but is controversial for an actual wind turbine airfoil. Due to surface contamination and aging, an essential smooth surface cannot

be guaranteed throughout the lifetime of a rotor blade. Thus, the performance is highly decreased, especially for laminar designed airfoils. The uncertainty gap between turbulent and laminar performance should be as small as possible if the laminar operation cannot be precisely foreseen. Incorporating a laminar airfoil, which is always operated at its maximum performance, is a challenging task with a high risk of uncertainty but also with a big chance of aerodynamic and acoustic advantages.

The above stated design guidelines will be used to modify the outer rotor blade airfoil NACA64618 of the NREL 5 MW turbine. The results on airfoil and turbine level in terms of aeroacoustic and aerodynamic behavior are presented in Section 5.2.2 in the next chapter.

5 Turbine Evaluation

For the full view of the acoustic wind turbine performance it is necessary to link the results gained in the previous section with the final three-dimensional design of the turbine. This task can be fulfilled in two basic ways. The first is to extend the two-dimensional CAA approach to the third dimension and conduct a three-dimensional CAA simulation for the (acoustically relevant) outer rotor blade region. The second option would be to find a strategy to link the two-dimensional results from the airfoil analysis with the operational parameters of the turbine, the rotor blade geometry and the observer position. This approach is mainly shown in this Chapter. Its advantages against the 3D CAA simulation are discussed and results for the observed trailing-edge noise in the vicinity of a wind turbine are shown. This Chapter unites almost all of the aforementioned methods, beginning with the blade element momentum method (BEM) to determine the wind turbine performance and using the aerodynamic and aeroacoustic results of the airfoil simulation toolchain as high fidelity input data.

5.1 Method

First, the three-dimensional CAA performance is shortly discussed to point out the very high computational effort and to underline the need for a more efficient method which incorporates the previously gained 2D results.

5.1.1 3D CAA Simulation

A three-dimensional simulation is conducted for the NACA0012 airfoil similar to the BANC-II #1 test case settings ($l_c = 0.4\,\mathrm{m}$, $\alpha = 0\,^\circ$, $M = 0.1664$). The 2D CAA mesh is used as the basis for the 3D mesh. In order to reduce the overall amount of cells, the final three-dimensional mesh is cropped to an extend of $2.35 l_c$ in x-direction and $2.2 l_c$ in y-direction. Moreover, the initial blocks are split into smaller blocks for a better parallelization of the computations. This results in a 2D mesh with 162 blocks and finally, with 4 blocks into the z-direction, in 648 blocks for the 3D mesh[1]. The final 3D mesh contains around 40 million cells. Its extend in spanwise direction is $0.05 l_c$. Due to the fine FRPM patch and the adopted resolution in the patch area the mesh shows a higher cell density in the middle and coarsens towards the outer parts. This adaptation is also made in z-direction. The FRPM patch is extended by 50 layers in the spanwise direction, extending $0.025 l_c$ (50 % of the CAA mesh). This results in a total number of 6 million patch cells. One FRPM particle per cell is set. The flow data of the 2D simulation is

[1] The parallelization approach of `PIANO` relies on the distribution of blocks from the computational mesh to individual CPUs. Thus a certain amount of blocks as well as a nearly equal distribution of mesh cells within the individual blocks is necessary for an efficient simulation in a multi-CPU high performance environment.

used. Constant values in z-direction are assumed. The same boundary conditions as in the 2D simulations are used. For the new faces (normal vector pointing in z-direction) a periodic boundary conditions is set.

The simulation is computed on the DLR case cluster using 324 CPUs for the CAA part and one CPU for the FRPM part. The wall clock time for 180000 iteration steps is around 240 hours or ten days. Even with a higher number of CPUs it was not possible to significantly reduce this effort. One reason for this is the communication time between the CAA blocks for the exchange of information over the block borders. Another problem is also the FRPM simulation which is only done by one CPU.

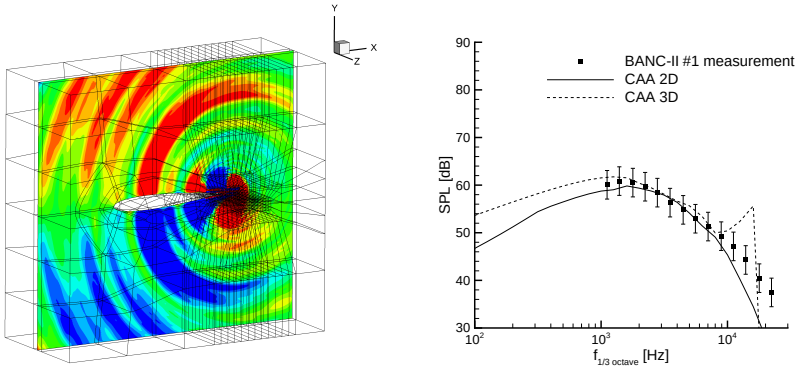

(a) (b)

Figure 5.1: 3D CAA Simulation of the NACA0012 BANC-II #1 test case; (a) snap shot of sound pressure field (red indicating positive pressure values, blue indicating negative values); (b) far-field sound pressure level spectrum at reference location compared to two-dimensional CAA results and measurement data.

Figure 5.1 (a) shows a snap shot of the sound pressure field in a x-y-plane around the airfoil. The typical dipole-like character, the cardioid form and the forward inclined directivity of the main radiation can be seen. The plot is very similar to the simulated sound pressure field of the 2D simulation shown in Figure 4.2 (a). In Figure 5.1 (b) the one-third-octave band spectra of 2D and 3D are compared. Additionally the measurement values are indicated by square symbols together with the error bars. Higher SPL values for the 3D simulation can be observed for lower frequencies. Up to 2 kHz the values are 2 dB to 5 dB higher. This behavior might be triggered by the relatively low number of iterations (180000 compared to 400000 in the 2D case) as the overall simulated time is shorter and less information for the long-wave-length, low-frequency sound waves are contained in the simulation data. Above 10 kHz a spurious peak appears in the 3D spectrum which is supposed to be of artificial nature and triggered either by the mesh resolution (as it is just before the cut-off frequency) or some problems due to the used periodic boundary condition. However, between 1 kHz and 10 kHz the 2D and 3D results are almost identical and both well within the uncertainty range of the measurements. This proves the ability

of the 3D approach for a valid noise simulation. With this approach time resolved data could be collected on a sampling surface around the airfoil and thereafter extrapolated to an arbitrary observer location using the Ffowcs-Williams and Hawkings [8] (FWH) method.

As a consequence of the very high computational times and the massive hardware demand to conduct the 3D CAA simulations, the decision was made to develop an alternative model which relies on the 2D results. Thus, it would be feasible to use the high fidelity CAA results to predict the trailing-edge noise emission of a whole wind turbine based on 2D sections. However, if computational resources are available and the time to obtain the simulation results is not critical, the 3D approach is also an option.

5.1.2 Alternative Method using 2D CAA Results

The combination of the used tools is depicted in Figure 5.2. To determine the overall turbine performance the BEM method (refer to Section 2.1.2) is used. Herein the rotor blade geometry, the general turbine settings and aerodynamic coefficients of the airfoils are needed as input parameters. The aerodynamic polar curves are calculated in advance using the CFD approach described in Section 3.2. Thereafter the turbine operation can be calculated and for each wind speed the local flow conditions at the blade can be determined. This also includes information about the local flow velocity and angle of attack for each radial rotor blade section. This information is used to generate CAA simulations for specific airfoils contained in the rotor blade geometry.

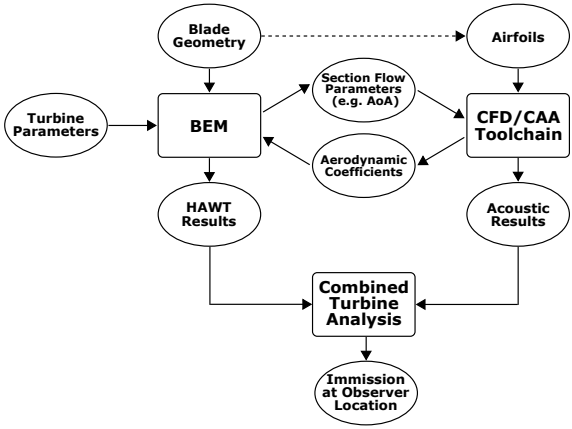

Figure 5.2: Schematic toolchain showing the consecutive steps for the simulation of aerodynamic and acoustic properties for a whole horizontal axis wind turbine (HAWT).

Now, the last step is to combine the acoustic information with the results from the BEM method. Therefore, the directivity $\overline{D}(\Theta, \Phi)$ of the trailing-edge noise (see Figure 2.5 and Equation 4.4) can be used together with the relative position between the observer and

the rotor blade section ($\vec{r}$). As the blade is dived into multiple spanwise sections during the BEM procedure this practically results in a summation of multiple noise sources (one for each section) with different directions and distances towards the ground based observer. Moreover, the variable observer position around the turbine (γ), the position of the rotor blade (φ) and the total number of rotor blades need to be considered. A sketch of the situation can be seen in Figure 5.3.

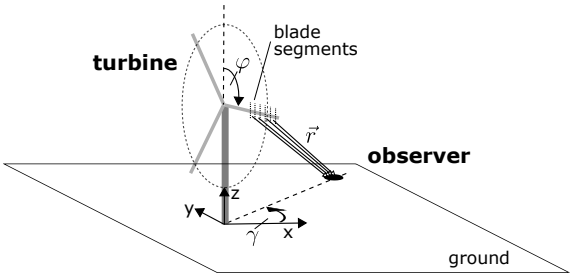

Figure 5.3: Sketch of turbine and observer location with indicated vectors $\vec{r}$ from blade section to observer location which depend on the rotor blade position and the observer location.

The consecutive steps to calculate the sound power level of a wind turbine at an arbitrary observer location are:

1. Obtain polar curves for the airfoils used in the rotor blade design either by CFD simulation or from measurements or literature.
2. Do BEM calculation for desired wind speed and determine flow velocity and angle of attack for the relevant radial blade sections.
3. Do CAA simulations for the airfoil geometries of the relevant sections. Consider the local flow conditions from the BEM method.
4. Determine overall sound pressure levels and directivity ($L_{p,OA} = f(\Theta)$) from the CAA results either at all Θ positions around the trailing-edge or only at the reference position[2] (refer to Figure 2.5).
5. Scale the section sound pressure levels to the desired local geometry and flow conditions (chord length, span, velocity, etc.) and apply the A-weighting if needed.
6. Calculate the distance and angles ($\vec{r}$, Φ, Θ) of each blade segment relative to the microphone position and consider the local twist angle of the section.
7. Calculate the sound pressure level of each segment at the observer position considering the directivity.
8. Sum up all noise signals and repeat for the other turbine blades at their appropriate positions.

[2] For the Θ influence the analytical directivity function can be used later on.

9. Repeat the above stated procedure for other rotor positions and average the results.

The scaling of step 5 and 6 is done via the following equation:

$$L_{p,\mathrm{obs}} = \underbrace{L_{p,\mathrm{OA,ref}} + 10\log\left(\overline{D}\right)}_{\mathrm{I}} + \underbrace{10\log\left(\frac{d}{d_{\mathrm{ref}}}\right)}_{\mathrm{II}} + \underbrace{50\log\left(\frac{v_{\mathrm{rel}}}{v_{\mathrm{ref}}}\right)}_{\mathrm{III}} + \underbrace{20\log\left(\frac{1}{|\vec{r}|}\right)}_{\mathrm{IV}}. \quad (5.1)$$

The scaling equation (Equation 5.1) consists of four distinct parts. In term I, the two-dimensional CAA sound pressure level at the reference position[3] $L_{p,\mathrm{CAA,ref}}$ is combined with the directivity function $\overline{D} = f(\Theta)$ to include the influence of the relative observer position. Note, that contrary to the semi-infinite half plane for which the directivity function is derived, some adaptions need to be made to account for airfoil geometries with limited x-dimension and an extend in the y-direction (thickness). The modification of $\overline{D}$ in the two-dimensional airfoil plane (x-y-plane) is shown in Appendix A.6. The approach of the reference location sound pressure level plus the modified directivity function can be used if acoustic information are only available at this position (i.e. also for measurements with only one microphone). If acoustic results are available for the whole microphone circle around the TE, as it is the case with all CAA simulations, this directivity information (which is a direct result of the simulation) can be used for the procedure. Thus, only the out of plane directivity due to Φ needs to be considered. Term II accounts for the spanwise extend of the section d in comparison to the span of the reference section of $d_{\mathrm{ref}} = 1\,\mathrm{m}$. The velocity scaling is done in term III. Herein, the relative velocity v_{rel} of the rotor blade section due to the radial position the turbine RPM and the wind speed and the reference velocity of the CAA simulation v_{ref} are considered. The last term accounts for the distance of the section to the observer position $|\vec{r}|$.

The presented approach for the evaluation of the sound immission at a certain observer position relies on several assumptions. First, the atmospheric damping of sound waves traveling from source to observer is neglected. Moreover refraction effects due to the wind speed and the atmospheric boundary layer profile are ignored. Also, frequency shifts due to the relative movement of source and observer (Doppler effect) are not taken into account. An assumption which is valid, at least for positions upstream and downstream of the turbine where the relative movement is reasonable small. Also, for A-weighted sound pressure levels the narrow-band spectra need to be considered and appropriately scaled and thereafter weighted for the correct final values. All these drawbacks need to be considered when the approach is used for a full turbine analysis. Nevertheless, the shown procedure in combination with the BEM turbine prediction can be used for a holistic evaluation approach of wind turbine performance and acoustics.

5.2 Results and Discussion

5.2.1 Analysis of the NREL 5MW Reference Turbine

For the predictions the NREL 5 MW reference off-shore turbine from Reference [61] is used. The advantage of this turbine clearly lies in the available data. Ranging from

[3] The reference position directly below the trailing-edge ($\Theta = 90\,^{\circ}$) at a distance of 1 m.

geometric details of the rotor blade like twist and chord distribution over the used airfoils to the control algorithm details. Note, that this turbine design is far away from modern (slender blades) onshore turbines but can still be used to show the relevant results of the evaluation method. Moreover the basic design (on-shore, off-shore, new, old) should not influence the relative comparison (e.g. answering the question of the noise mitigation effect if the standard airfoils are exchanged by low noise versions). A relative comparison of different cases is possible.

Aerodynamic Performance

The three-bladed upwind Turbine has a rotor radius of $R = 63\,\mathrm{m}$. The airfoil geometry is given in Reference [61]. The relevant distributions of chord length l_c twist angle β and relative thickness t/l_c are plotted against the non-dimensional radius position r/R in Figure 5.4 (a). It can be seen, that an almost constant relative thickness of $t/l_c \approx 18\,\%$ is used for the last 36 % of the rotor blade length. In this section the NACA64618 airfoil (appropriately scaled to the thickness distribution) is used.

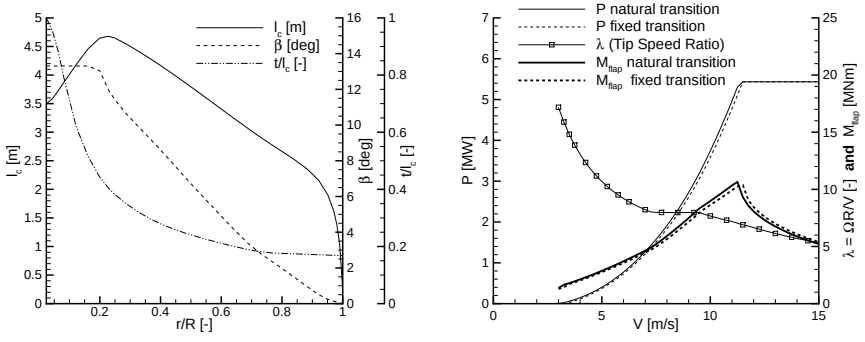

Figure 5.4: NREL 5 MW reference turbine; (a) geometry represented by the distribution of chord length l_c, twist angle β and relative thickness t/l_c along the non-dimensional blade radius r/R; (b) operational data of the wind turbine plotted against the wind speed for power and tip speed ratio (TSR) λ.

Due to the higher relative speed of the outer rotor blade part, the main effort of the analysis is directed to this specific region. Therefore new polar curves are calculated for the NACA64618 airfoil for a Reynolds number of $Re = 6 \cdot 10^6$ and two different transition settings using the CFD method from Section 3.2. The airfoil is simulated with a natural transition setting (best performance) and a fix transition near the leading-edge (worst performance e.g. rough surface due to dirt adherence or erosion). The glide ratio c_L/c_D for both simulations plotted against the angle of attack can be seen in Figure 5.5 (a). A

significant reduction in performance can be seen for the fixed transition case (mainly due to the increase of friction drag with the loss of laminar running length).

With the simulated polar curves and the rest of the given data for the NREL turbine, a BEM calculation is conducted which yields the turbine performance for different wind speeds. The original NACA64618 polar curve (contained in the NREL data) is exchanged by the CFD results in order to obtain consistent results. Again two cases - natural and fixed transition - are calculated. Figure 5.4 (b) depicts the turbine shaft power ($P = M\omega$) for both cases and the tip speed ratio (TSR or λ) indicated by symbols. The power curves of the two cases are almost identical. This is particularly interesting if the severe difference in glide ratio (Figure 5.5 (a)) is taken into account. The influence of the fixed transition of the outer rotor blade airfoils (last 36 % of the blade length) only accounts for a power reduction of $\Delta P \approx -4\,\%$ even as the glide ratio is reduced by $\Delta c_L/c_D \approx -50\,\%$. This behavior is further discussed and analyzed in Section 5.2.3.

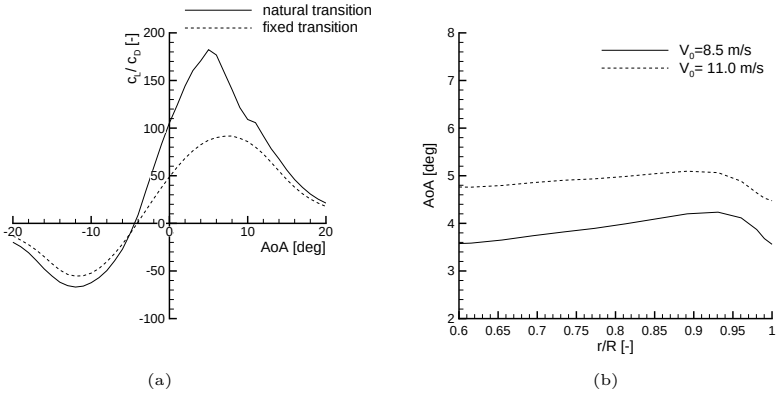

Figure 5.5: Aerodynamic Performance of the NREL 5MW rotor blade: (a) L-over-D ratio c_L/c_D vs. angle of attack α for the NACA64618 airfoil; (b) angle of attack distribution at the outer blade for two different wind speeds.

Beside the power curve, the tip speed ratio is shown in Figure 5.4 (b). It can be seen that λ is constant between $V_0 = 7.5\,\mathrm{m/s}$ and $V_0 = 9.5\,\mathrm{m/s}$ wind speed. This range, where the optimum tip speed ratio is constant (refer to Section 2.1.3) corresponds to the mean wind speed for which the turbine is designed. As it is an off-shore turbine the mean wind speed is quite high (see mean wind speeds of the different wind classes in Table A.1 in Appendix A.1). For further calculations two distinct wind speeds are chosen. The first operating condition is at the optimum tip speed ratio at $V_0 = 8.0\,\mathrm{m/s}$. The second operating condition is at the wind speed just before rated power is reached at $V_0 = 11.0\,\mathrm{m/s}$. For both wind speeds the local angle of attack distribution at the outer rotor blade section is plotted in Figure 5.5 (b). It can be seen, that the angle of attack is almost constant at $\alpha \approx 4\,^\circ$ for the $V_0 = 8.0\,\mathrm{m/s}$ case. For the second wind speed just

before rated Power (before pitching begins) the highest angles of attack are reached. The value is also almost constant and around $\alpha \approx 5\,^\circ$ for $V_0 = 11.0\,\mathrm{m/s}$.

To evaluated the load on the rotor blade the blade root flapwise bending moment[4] M_{flap} is also depicted in Figure 5.4 (b) (thick lines, values on secondary abscissa). The Maximum values for turbulent and natural transition performance are almost identical around $M_{\mathrm{flap}} \approx 10.5\,\mathrm{MNm}$. Due to the slightly lower performance the value for the turbulent operation is approximately 4 % lower than for natural transition. After reaching rated power at $V_0 = 11.5\,\mathrm{m/s}$ the values decrease due to the increasing rotor blade pitch angle which reduces the local angles of attack and thus the local c_L values. An overview of all relevant values can be found in Table 5.1.

Table 5.1: Representative values calculated by the BEM method for two distinct wind speeds of the NREL 5MW turbine distinguished for fixed and natural transition.

wind speed		$V_0 = 8.5\,\mathrm{m/s}$		$V_0 = 11.0\,\mathrm{m/s}$	
transition		nat. trans.	fix. trans.	nat. trans.	fix. trans.
P	[MW]	2.292	2.196 (-4.2 %)	4.968	4.779 (-3.8 %)
M_{flap}	[MNm]	6.679	6.373 (-4.6 %)	10.345	9.921 (-4.1 %)
λ	[-]	7.9		7.2	
α_{avg}	[deg]	3.9		4.9	
c_L/c_D	[-]	169.6	81.6 (-51.9 %)	186.5	83.6 (-55.2 %)
$L_{p,\mathrm{OA,IEC}}$	[dB]	46.3	51.0 (-4.6)	49.6	54.2 (-4.6)

Acoustic Performance

The application of the two-dimensional noise extrapolation method as shown in Section 5.1.2 can now be used to determine the sound pressure levels of the NREL turbine at different observer locations. For certification issues, a distinct observer position defined by the IEC [78] is used to standardize wind turbine noise measurements. This measurement position is located directly downwind of the turbine on the ground at a distance of the tower height plus the rotor blade length. The tower height is supposed to be $H = 100\,\mathrm{m}$. Figure 5.6 (a) depicts the time averaged overall sound pressure level[5] ($L_{p,\mathrm{OA,IEC}}$, where the index IEC is indicating the IEC standard measurement position) at the IEC measurement position as a function of the wind speed V_0. The following results are obtained using the resulting directivity from the CAA simulations. A comparison with the alternative approach (only SPL data at reference location and modified flat plate directivity) can be found in Appendix A.6. Two different settings are shown: one for natural and one fixed transition. Precise OASPL values for the optimum TSR wind speed range ($V_0 = 8.5\,\mathrm{m/s}$) and for the point just before rated power ($V_0 = 11.5\,\mathrm{m/s}$) can be found in Table 5.1.

[4] The flapwise bending moment is the torque around zero-pitch chord axis at the blade root. It is caused by the aerodynamic forces acting on the blade. It can be compared to the wing root bending moment of an airplane wing.

[5] Time averaged means that the SPL values of different rotor positions (φ) for the three turbine blades are taken into account. Averaging is done via: $L_{p,\mathrm{OA,avg}} = 10 \cdot \log\left[\frac{1}{N}\sum_{i=1}^{N} 10^{L_{p,i}/10}\right]$ for N ($N = 36$, $\Delta\varphi = 10\,^\circ$) positions.

Independent of the transition setting, a steady increase of the noise with the wind speed can be observed. Between $V_0 = 3.0\,\mathrm{m/s}$ and $V_0 = 7.5\,\mathrm{m/s}$ the increase is relatively small due to the fifth-power-law of the TBL-TEN scaling (Equation 2.34) and the low increase of the turbine RPM in this region (high TSR but very low wind speed). In the optimum TSR wind speed range ($7.5\,\mathrm{m/s} < V < 9.5\,\mathrm{m/s}$) the turbine RPM is linear increased with the wind speed. The sound emission is increased. Beyond $V_0 = 9.5\,\mathrm{m/s}$ the slope of the SPL curve decreases (decreasing RPM gain with wind speed) until the values are nearly constant for wind speeds greater than $V_0 = 11.0\,\mathrm{m/s}$. This can be explained by the operation of the turbine. Beyond rated power the RPM is kept constant to stay below the generator upper RPM limit. The power is held constant by changing the pitch angle of the blades (adapting the aerodynamic forces to the high wind speeds and constant RPM). As the relative velocity seen by each airfoil section is mainly influenced by the turbine's RPM and the velocity has the main relevance for the TBL-TEN signal strength, the noise emission stays constant. Directivity changes due to small pitch angles (see Figure A.3) are almost negligible for Θ values around $\Theta = 90\,°$.

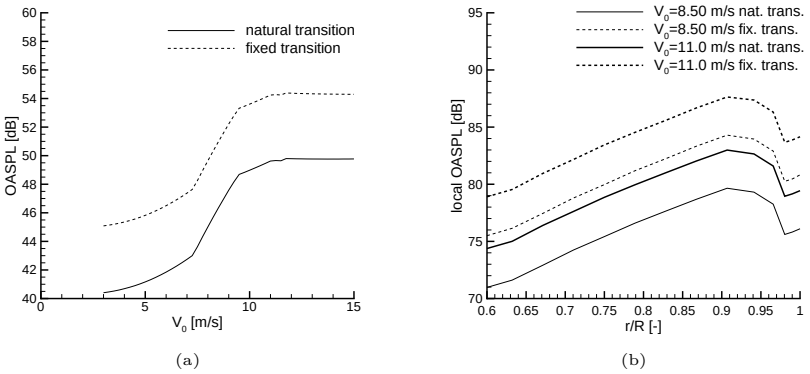

Figure 5.6: Acoustic results for NREL 5 MW turbine for fixed and natural transition at the outer rotor blade airfoils: (a) OASPL at the IEC reference position ($R_1 = 163\,\mathrm{m}$, tower height $H = 100\,\mathrm{m}$); (b) local sound emissions of the blade sections for $V_0 = 8.5\,\mathrm{m/s}$ and $V_0 = 11.0\,\mathrm{m/s}$ at the airfoil local observer position (distance $x/l_c = 1$).

As the NACA64618 airfoil shows a very good aerodynamic performance when operating under perfect conditions in natural transition (see Figure 5.5) and a severe loss of aerodynamic performance - and thus a high increase of BL thickness and TKE levels at fully turbulent conditions - a strong acoustic dependence on the transition setting can be found. Natural transition operation is about 4.5 dB lower than fixed, fully turbulent operation. Figure 5.6 (b) also highlights this difference. Here, the contributions of the respective sections of the rotor blade are plotted. The SPL values are calculated for the blade sections at a distance of 1 m taking into account the local section geometry and relative flow speed. It can be seen, that the outward blade sections show the highest con-

tributions to the overall noise emission. Due to the reduced chord length the SPL values are decreasing beyond 90 % of the rotor radius. Moreover, the twist angle in this region is increasing, which means decreasing angles of attack for the blade tip. The reason for this is the avoidance of the tip vortex in the rotor blade design which reduces the induced drag due to the tip vortex formation and also the tip noise. From an acoustic point of view, the outward 15 % to 20 % of the blade length are the most relevant for introducing noise reduction techniques. It can be seen from Figure 5.6 (b) that the SPL values in this region are more than 5.0 dB higher than the values at inward positions.

The observer position is systematically varied in the vicinity of the turbine. By this, noise maps as depicted in Figure 5.7 and Figure 5.8 can be calculated. Note, the higher SPL values in Figure 5.8 for the higher wind speed. Again, the two representative wind speeds $V_0 = 8.5\,\mathrm{m/s}$ and $V_0 = 11.0\,\mathrm{m/s}$ are analyzed. Moreover, the difference between natural and turbulent transition is shown. The turbine is located in the center of the plots ($x = 0$, $y = 0$). Regions with higher sound emission can be found in the direction upstream and downstream of the turbine. In the direction of the rotor plane ($y = 0$) lower values due to the TBL-TEN noise directivity with small values in the chord direction can be seen. This behavior is present in all cases, disregarding wind speed and transition setting.

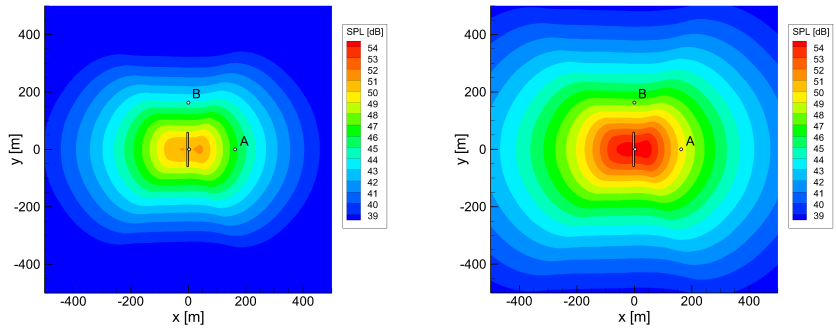

Figure 5.7: Overall sound pressure at ground level in the vicinity of the Turbine (tower height $H = 100\,\mathrm{m}$, turbine location at $x = 0$ and $y = 0$) for natural transition at wind speed: (a) $V_0 = 8.5\,\mathrm{m/s}$ and (b) $V_0 = 11.0\,\mathrm{m/s}$.

For the natural transition settings (Figure 5.7) a 3 dB difference in SPL values due to the increase of wind velocity from 8.5 m/s to 11.0 m/s can be observed. Nearly the same value, but for higher sound pressure levels, can be found for the fixed transition case (Figure 5.8). The only difference is the slightly higher decrease of SPL values for the turbulent case in the direction of the rotor plane. Here the variance of the noise immission around the turbine for a fixed distance is larger. This behavior is further analyzed in Figure 5.9. Here, the overall sound pressure level along a circle with a constant distance from the

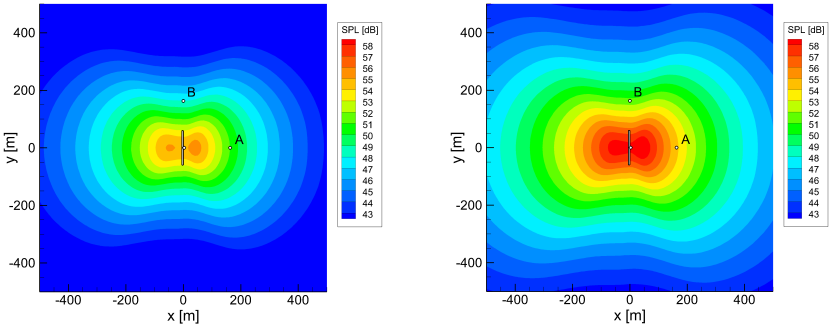

(a) (b)

Figure 5.8: Overall sound pressure at ground level in the vicinity of the Turbine (tower height $H = 100\,\mathrm{m}$, turbine location at $x = 0\,\mathrm{m}$ and $y = 0\,\mathrm{m}$) for fixed transition at wind speed: (a) $V_0 = 8.5\,\mathrm{m/s}$ and (b) $V_0 = 11.0\,\mathrm{m/s}$.

tower of $R_1 = H + R$ is depicted in a polar plot. The Distance R_1 is chosen in accordance with the distance of the microphone for the IEC certification measurement.

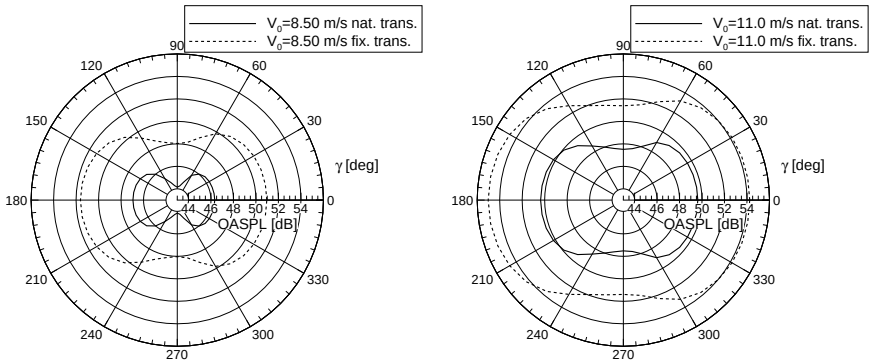

(a) (b)

Figure 5.9: Overall sound pressure at ground level at a distance of $R_1 = 163\,\mathrm{m}$ at wind speed: (a) $V_0 = 8.5\,\mathrm{m/s}$ and (b) $V_0 = 11.0\,\mathrm{m/s}$.

The effect of the louder turbulent airfoils is most prominent in the wind direction. Upstream and downstream of the turbine the natural transition case shows a 4.5 dB lower

level than the fixed transition case. If the observer position is changed to a position in the rotor plane ($\gamma = 90\,^\circ$ or $\gamma = 270\,^\circ$), this difference shortens to 3.8 dB. The noise reduction due to the laminar boundary layer flow is reduced for this observer positions. Following the SPL graphs for the different wind speeds in Figure 5.9, it can be seen, that for the turbulent flow situation the noise reduction due an observer position change from $\gamma = 0\,^\circ$ to $\gamma = 90\,^\circ$ is 2.0 dB. For the natural transition case it is only 1.3 dB. Thus, the noise variation for the turbulent flow regime due to the observer position is larger.

The turbine calculation reveals another interesting fact, when the noise values are calculated for different rotor positions and no averaging (see Footnote 5) is done. Therefore, the rotor position dependent sound pressure levels are calculated at the points A (downstream $\gamma = 0\,^\circ$, distance $R_1 = 163\,\mathrm{m}$) and B (in rotor plane $\gamma = 90\,^\circ$, distance $R_1 = 163\,\mathrm{m}$) as indicated in Figures 5.7 and 5.8. The results for one full revolution of the three-bladed turbine are depicted in Figure 5.10. The fixed transition values are indicated by the bold lines. The inside rotor plane position B is indicated by the dashed graphs.

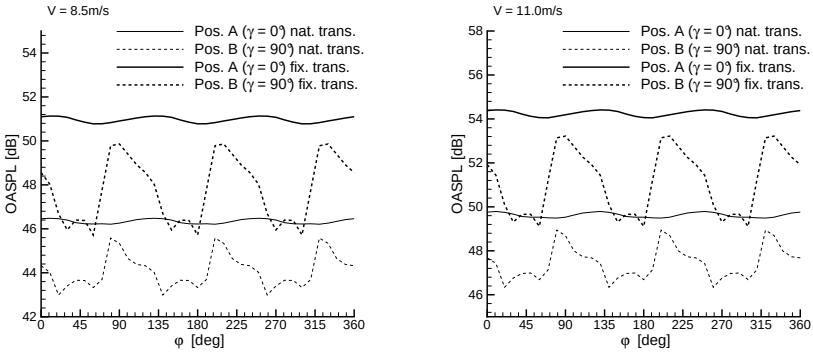

(a) (b)

Figure 5.10: Overall sound pressure level at two observer locations (A: downstream of the turbine ($x = 163\,\mathrm{m}$ and $y = 0\,\mathrm{m}$, IEC reference position) and B: crosswind position in the rotor plane ($x = 0\,\mathrm{m}$ and $y = 163\,\mathrm{m}$)) for different rotor blade positions at wind speed: (a) $V_0 = 8.5\,\mathrm{m/s}$ and (b) $V_0 = 11.0\,\mathrm{m/s}$.

Comparing position A to position B it can be seen that the variation of the sound pressure level with the instantaneous rotor position is much higher for the position in the rotor plane (B). While the actual SPL values are nearly constant at position A ($\Delta L_p < 0.5\,\mathrm{dB}$) the variation at position B is around $\Delta L_p < 4.0\,\mathrm{dB}$ for the fixed transition case and $\Delta L_p < 2.5\,\mathrm{dB}$ for the natural transition case. Three distinct humps, each at the position where one blade is in the horizontal position and in downward motion, can be found in the plots. Note, that the traveling time from source to observer is not taken into consideration in this analysis. For a more precise prediction of the SPL values in observer time a correction must be applied. Nevertheless, the actual results lead to an interesting finding. While the SPL values upstream and downstream of the turbine are higher than

those for crosswind positions in the rotor plane, the variation of the sound power level with the turbine RPM is much higher for the $\gamma = 90\,^\circ$ position. This corresponds to a phenomenon called amplitude modulation (AM). AM is described as a swishing noise at the frequency of the blade passing frequency with a modulation of up to 5 dB (see References [26, 79] which is most prominent in the crosswind direction. Even if the actual SPL values are quite low at a certain distance from the turbine, amplitude modulation and the swishing character of the noise are still described as very annoying [80]. Beside the absolute values, which are higher for the $V_0 = 11.0\,\mathrm{m/s}$ wind speed, the behavior is exactly the same for the lower $V_0 = 8.5\,\mathrm{m/s}$ wind speed. The amplitude modulation for the fixed transition is for both wind speeds higher than for the natural transition which drives the assumption that the AM issue might become more present with increasing age of the turbine and thus a more turbulent BL flow due to dirt adhesion or erosion of the rotor blade surface. Moreover, the dependence of the AM strength on the position γ explains the stochastic occurrence of the phenomena due the changing wind directions and the resulting turbine's yaw movement.

The calculated results show that the use of the BEM method together with the CFD and CAA simulations yields useful results for the overall aerodynamic and aeroacoustic turbine performance. Basically the difference found in the 2D simulations can also be found in the acoustic turbine results. An airfoil with a lower noise signature at its reference location will also be less noisy at an arbitrary observer location if compared to another louder airfoil. Nevertheless, differences are found for the crosswind position and a more detailed look can be taken into the time-resolved noise signature of the turbine. For the NREL turbine the rather big influence of the transition location on the blade has to be kept in mind when doing noise predictions. As it is quite hard to do a prediction of the transition, the two graphs as depicted in Figure 5.6 (a) must be seen as best and worst performance values. The relative high difference between fixed and natural transition noise emission bears a high uncertainty for a noise prediction of this turbine. For the aerodynamics the loss of glide ratio does not show such a strong influence as it is doing for the acoustics. Moreover, it has to be kept in mind, that the presented approach only contains the trailing-edge noise mechanism. For the complete picture other flow-induced and mechanical noise sources (refer to Section 2.3.7) need to be considered. Thus, the rather low noise laminar performance might be masked by another noise source which is just below the turbulent trailing-edge noise signal oterwise.

5.2.2 Improvement of NREL 5MW Turbine with Low-Noise Airfoils

In this last section it is tried to combine the gained knowledge for TBL-TEN prediction and the driving geometric parameters to mitigate the noise of the NREL 5 MW reference turbine. Therefore, the outer part rotor blade airfoil (NACA64618) is adapted according to the guidelines presented in Section 4.5. Several geometric changes are analyzed from which only the airfoil with the most promising characteristics is shown in the following results. The design objectives of the analysis are to maintain the good aerodynamic characteristics of the NACA64618 airfoil (in terms of c_L/c_D ratio) while reducing the TBL-TEN signal. To maintain the structural characteristics the relative thickness of the airfoil is held constant at $t/l_c = 18\,\%$. The geometry changes are done by hand with the help of a spline fitting tool. The initial geometries are smoothed to achieve a steady c_p distribution using the inverse design routines in the airfoil design program XFOIL[81].

Note, that the modifications should only show the feasibility of certain geometry changes for noise benefits and are in no kind an optimization. An optimization procedure is explicitly avoided for these calculations as the main goal is to extract the coherence of shape and acoustics. Ultimately, the method could be given to an optimization tool, but engineering knowledge is higher prioritized for the actual task.

Airfoil Level

Figure 5.11 (a) depicts the geometry of the NACA64618 airfoil (solid line) and the modified low-noise airfoil LNCR18[6]. In the following, the airfoil names will be abbreviated as NACA and LNCR airfoil. For the LNCR airfoil the shape of the aft suction side part is modified for a shallower pressure regain and thus a thinner less turbulent boundary layer at the suction side. To counteract the loss of lift production the rear loading at the aft part of the suction side is increased. Additionally the thickness in the front part of the airfoil is also increased. Due to the overall narrower shape of the LN airfoil the bending stiffness around the x-axis for the skin is reduced by 15 % compared to the NACA airfoil. This loss could be tolerated as the airfoil is used in the outer rotor blade part where aerodynamic parameters are higher prioritized than structural ones. Moreover, the loss of bending stiffness of the skin could be remedied by structural elements inside the blade (girders or spar caps positioned at the maximum thickness position of the airfoils). As the relative thickness is constant at $t/l_c = 18\,\%$ no major structural issues arise. Only the very thin aft part of the noise optimized airfoil (due to the concave shape on suction and pressure side) may need some special treatment concerning manufacturing.

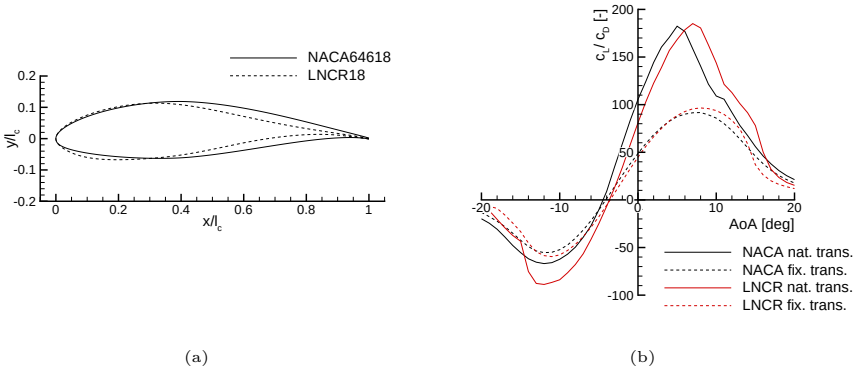

(a) (b)

Figure 5.11: Comparison of original NACA64618 and modified LNCR18 airfoil for the NREL 5MW reference turbine: (a) normalized geometry; (b) c_L/c_D polars for natural and fixed transition.

[6] LN stands for low noise and CR for the initials of the author while the number 18 represents the relative thickness of the airfoil.

Standard CFD calculations are performed to judge the aerodynamic behavior of both airfoils in natural and fixed transition operation. The results for the angle of attack dependent glide ratio are shown in Figure 5.11 (b). For the fixed transition case (dashed lines) a slightly better performance of the LNCR airfoil can be observed for angles of attack higher than $\alpha = 6\,^\circ$. In the natural transition flow regime the LNCR airfoil curve is shifted $1.5\,^\circ$ towards higher angles of attack, meaning that the airfoil can reach almost the same aerodynamic performance as the NACA if a slightly higher angle of attack is chosen for the operation. Again, the performance under natural transition conditions is around 50 % to 80 % better considering the c_L/c_D ratio. From a general perspective the aerodynamic performance of both airfoils can be considered almost identical. As a consequence no major changes in the performance of the turbine are expected if the NACA airfoil is exchanged with the noise optimized LNCR foil.

Acoustic simulations according to the procedure described in Section 3.3 are carried out for both airfoils. A Reynolds Number of $Re = 6.0 \cdot 10^6$ is chosen. The angle of attack is varied between three and six degrees in steps of one degree. For the NREL turbine at the relevant wind speeds the expected AoA lies around five degrees (see Table 5.1). Again, natural and fixed transition are distinguished. The previously conducted CFD simulations yield the flow and turbulence data for the `PIANO` FRPM simulation.

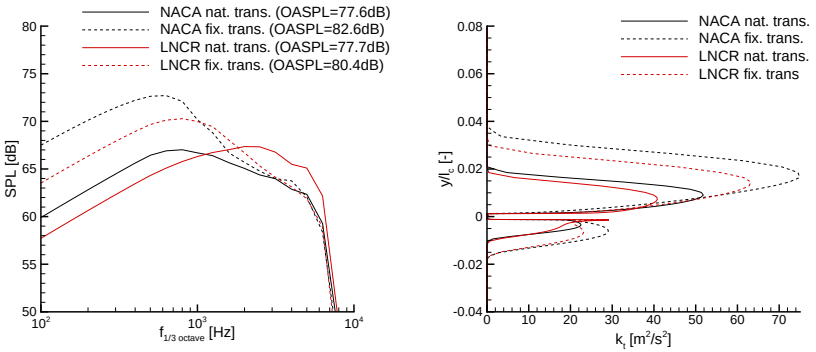

Figure 5.12: Comparison of acoustic performance of NACA and LN airfoil for different transition regimes at $\alpha = 4.0\,^\circ$ an $Re = 6.0 \cdot 10^6$: (a) one-third octave band sound pressure level spectra at 2D reference location; (b) distribution of turbulence kinetic energy k_t along a chord-perpendicular line located at the trailing-edge.

A precise look into the acoustic airfoil data is given in Figure 5.12 for the four degree angle of attack case. Here, spectra for the one-third-octave band sound pressure levels are shown (Figure 5.12 (a)) together with the turbulence kinetic energy profiles directly at the trailing-edge (Figure 5.12 (b)). The close relation between the TKE values and the emitted noise (refer to Section 4.4) can also be found for these airfoils.

For the NACA airfoil (black lines) a strong increase of TKE levels especially at the suction side can be observed when the transition is fixed at the leading edge. Higher TKE levels and a thicker suction side boundary layer result in higher SPL values at lower frequencies. Consequently, the overall sound pressure level is increased by 5 dB. The same behavior can be observed for the low-noise airfoil. The only difference is the spectral shape for the natural transition case of the LNCR foil. Here, the peak frequency is shifted towards higher values (around $f = 3\,\text{kHz}$). One explanation for this could be the pronounced peak at the pressure side TKE profile directly at the wall which seems to trigger higher frequencies. Even though the suction side TKE profile shows lower values in the natural transition case for the LNCR airfoil than for the NACA airfoil the overall sound pressure levels are almost identical for the two airfoils(77.7 dB for the NACA and 77.6 dB for the LNCR airfoil). Considering the fixed transition case the picture changes. Now, the LN airfoil has lower TKE values on both sides resulting in lower SPL values throughout the spectrum and thus in an overall sound pressure 2.2 dB below the NACA value. This noise reduction is achieved without aerodynamic drawbacks (refer to Figure 5.11 (b)).

Turbine Level

A combined view of aerodynamic and acoustic airfoil performance is given in Figure 5.13 (a). Overall sound pressure levels and glide ratios are plotted for angles of attack from three to six degrees in steps of one degree. It can be seen, that for the natural transition case (solid lines) both airfoils can reach glide ratios between 140 and 190 while the overall sound pressure level lies between 77.5 dB and 79.5 dB. The performance on both scales in this case seems almost identical. The main difference between the two airfoils can be observed for the fixed transition simulations. Here, both airfoils reach glide ratios between 75 and 95 in the desired AoA range while clearly reduced overall sound pressure levels can be found for the LNCR airfoil. The NACA airfoil shows OASPL values between 82 dB and 83 dB, the LN airfoil operates at values which are between 1 dB to 2 dB lower. While the same aerodynamic performance is achieved a significant noise reduction is possible with the LNCR airfoil.

In a final step the newly designed low noise airfoil is incorporated into the NREL design by exchanging the outer rotor blade NACA airfoil with the new LNCR airfoil. From CFD simulations all relevant aerodynamic coefficients are known to feed the BEM calculations and determine the overall turbine characteristics. The results for different wind speeds are depicted in Figure 5.13 (b). Precise values for two distinct wind speeds of 8.5 m/s and 11.0 m/s (refer to Section 5.2.1) are grouped together in Table 5.2 for the natural transition case and Table 5.3 for the fixed transition case.

For the natural transition case the new noise optimized airfoils result in a negligible increase of power of 0.3 % at 8.5 m/s which diminishes towards the rated-power wind speed of 11 m/s where no influence can be observed. This behavior was almost expected, as the aerodynamic performance of both airfoils is nearly identical. An interesting fact here is the reduction of the flapwise bending moment M_{flap} of roughly three percent due to the new airfoils throughout both wind speed cases (see Table 5.2). Thus, a load reduction without power influence is achieved with the new airfoils. For the fixed transition case the new LNCR airfoil yields a power increase of roughly one percent, while the flapwise bending moment remains almost unchanged (reduction between 0.3 % and 0.1 %). The power increase is achieved without any load increase which can be seen as a positive

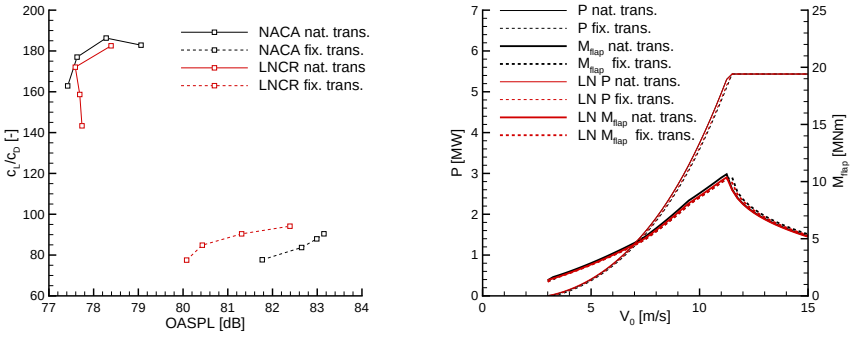

(a) (b)

Figure 5.13: Performance for modified NREL Turbine under different transition conditions: (a) combined plot of airfoil noise (OASPL) and aerodynamic performance (c_L/c_D) for NACA and LNCR airfoil; (b) overall turbine performance with NACA and LN airfoil for power and flapwise bending moment.

Table 5.2: Performance of the NREL turbine with standard NACA and modified LNCR airfoils under natural transition conditions.

wind speed		$V_0 = 8.5\,\mathrm{m/s}$		$V_0 = 11.0\,\mathrm{m/s}$	
modification		standard	low noise	standard	low noise
P	[MW]	2.292	2.300 (0.3 %)	4.968	4.965 (0.0 %)
M_{flap}	[MNm]	6.679	6.493 (-2.8 %)	10.345	10.069 (-2.7 %)
$L_{p,\mathrm{OA,IEC}}$	[dB]	46.3	46.3 (-0.0)	49.6	49.6 (-0.0)
$L_{W,\mathrm{IEC}}$	[dB]	102.9	102.9 (-0.0)	106.2	106.2 (-0.0)

side effect of the new airfoils. Considering the aerodynamic performance and the (very simple) load indication parameter of the flapwise bending moment, the LNCR airfoil shows improved properties for the NREL 5 MW rotor. This is also underlined by the value of the annual energy production (AEP, refer to Section 2.1.2) which can be calculated for a mean wind velocity and a standardized wind speed distribution (refer to Figure A.1 in the Appendix).

Table 5.4 shows the AEP values for different mean wind velocities for the NREL turbine. It is distinguished between natural and fixed transition as well as standard (NACA) and low noise (LNCR) airfoil. The changes due to the LNCR airfoil are indicated in brackets. For both transition cases a slight increase of the AEP can be found with the new airfoils. Higher increases (1.3 % at $\overline{V} = 6.0\,\mathrm{m/s}$ and 0.5 % at $\overline{V} = 10.0\,\mathrm{m/s}$) can be found for the fixed transition case compared to the natural transition case (0.5 % at $\overline{V} = 6.0\,\mathrm{m/s}$ and 0.1 % at $\overline{V} = 10.0\,\mathrm{m/s}$). The reason for this is the better performance of the LNCR airfoil

Table 5.3: Performance of the NREL turbine with standard NACA and modified LNCR airfoils under fixed transition conditions.

wind speed		$V_0 = 8.5\,\mathrm{m/s}$		$V_0 = 11.0\,\mathrm{m/s}$	
modification		standard	low noise	standard	low noise
P	[MW]	2.196	2.225 (1.3 %)	4.779	4.829 (1.0 %)
M_{flap}	[MNm]	6.373	6.357 (-0.3 %)	9.921	9.913 (-0.1 %)
$L_{p,\mathrm{OA,IEC}}$	[dB]	51.0	49.2 (-1.8)	54.2	52.5 (-1.7)
$L_{W,\mathrm{IEC}}$	[dB]	107.6	105.8 (-1.8)	110.8	109.1 (-1.7)

Table 5.4: Annual energy production (AEP) for the NREL turbine with modified airfoils (deltas to standard NACA airfoil are indicated in brackets).

$\overline{V}$ [m/s]	AEP [MWh] natural transition		AEP [MWh] fixed transition	
	standard	low noise	standard	low noise
6.0	9909.7	9959.3 (0.5 %)	9536.6	9661.0 (1.3 %)
7.5	16016.7	16061.4 (0.3 %)	15592.3	15727.7 (0.9 %)
8.5	19635.6	19675.7 (0.2 %)	19214.2	19346.5 (0.7 %)
10.0	23970.7	24004.3 (0.1 %)	23581.3	23701.8 (0.5 %)

under fixed transition conditions. The fading increase towards higher mean wind speeds is caused by the operation of the turbine. With a higher mean wind speed the turbine is operating more often in rated-power conditions (above rated wind speed). The power is held constant by pitching the blades and the same output is generated independent of the used airfoil (see Figure 5.13 (b) for wind speeds above 11.5 m/s).

Beside aerodynamic and load performance indicators, Table 5.2 and Table 5.3 also contain the overall turbine sound pressure level at the IEC reference position ($L_{p,\mathrm{OA,IEC}}$) calculated with the CAA simulation data according to the procedure shown in Section 5.1.2. In the IEC publication [78] a calculation procedure to determine the equivalent turbine sound *power* level L_W from the sound *pressure* level at a given observer position is provided:

$$L_W = L_p + 10\log\left(\frac{4\pi R_1^2}{S_0}\right) . \tag{5.2}$$

Practically, the sound power level calculated by Equation 5.2 does not depend on distance, though theoretically it may diminish with distance due to viscous effects in the propagation of sound which are neglected in this procedure. The distance $R_1 = H + R$ is the microphone distance from the tower. The reference area S_0 is chosen to $S_0 = 1\,\mathrm{m}^2$. Using the sound power level enables the comparison of different wind turbines (e.g. with different hub heights). Thus, this value is mainly used by manufactures and certification organizations for the evaluation of wind turbine noise. As the turbine dimensions as well as the observer positions are equivalent in the present study, the same conclusions may also be drawn for the sound pressure level.

Comparing the overall sound pressure levels for the standard (NACA) and modified

(LNCR) NREL turbine the advantages of the new airfoils can be seen. Figure 5.14 (a) depicts the values for different wind speeds and transition regimes (precise values can be found in Table 5.2 and Table 5.3). As expected, the noise performance is almost identical in the natural transition case because no significant noise reduction is achieved with the LNCR airfoils for this setting (refer to Figure 5.13 (a)). Only for wind speeds below 7 m/s and above 12 m/s a slight noise reduction can be found. For the fixed transition case the main advantage of the new airfoils becomes clearer. Throughout the whole wind speed range, a noise reduction of $\Delta L_{p,\mathrm{OA}} \approx 1.8\,\mathrm{dB}$ can be found which is less than the sound pressure level difference of the NACA and LNCR airfoil of 2.2 dB due to the use of other (not modified) airfoils in the rest of the rotor blade. However, the main reductions from the airfoil level can also be seen for the analysis of the whole turbine. Similar to Figure 5.6 (b) the local sound pressure levels for the rotor blade sections are depicted in Figure 5.14 (b). For the sake of clarity, only the 8.5 m/s case is shown as the same behavior is also found for the 11 m/s case. The noise reduction under fixed transition conditions is also clearly visible in this plot.

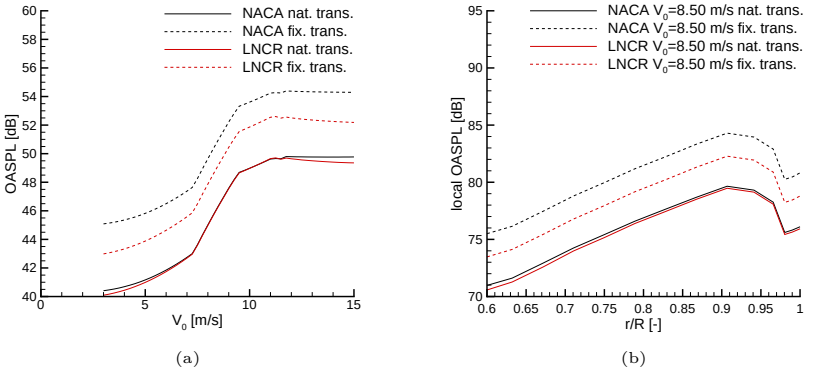

Figure 5.14: Acoustic results for NREL 5 MW turbine for fixed and natural transition with standard (NACA) and low noise (LNCR) airfoil at the outer rotor blade section: (a) OASPL at the IEC reference position ($R_1 = 163\,\mathrm{m}$, tower height $H = 100\,\mathrm{m}$); (b) local sound emissions of the blade sections for $V_0 = 8.5\,\mathrm{m/s}$ and $V_0 = 11.0\,\mathrm{m/s}$ at the airfoil local observer position (distance $x/l_c = 1$).

The noise reduction ability of the LNCR airfoil incorporated into the NREL rotor blade can also be seen in the noise maps shown in Figure 5.15. Again, no benefit - considering noise immission on the ground - can be found for the natural transition case (see Figure 5.15 (a) and Figure 5.15 (b)). In contrast to that, a severe reduction can be seen for the fixed transition case (see Figure 5.15 (c) and Figure 5.15 (d)). A much smaller noise contour with lower overall sound pressure levels can be found for the LNCR airfoil. This finding could help reducing the observer distance while keeping the noise immission constant. For wind turbine sites where the local sound immission determines the observer

distance and thus the available area for new turbines this can be an interesting option (see also Section 5.3 for a more detailed discussion). Due to the same behavior for the rated-power 11.0 m/s operation only the 8.5 m/s case for the optimal TSR performance is shown. Note, that due to the wind speed distribution (see also Section 2.1.3), most of the turbine's operation hours will be spend in this wind regime.

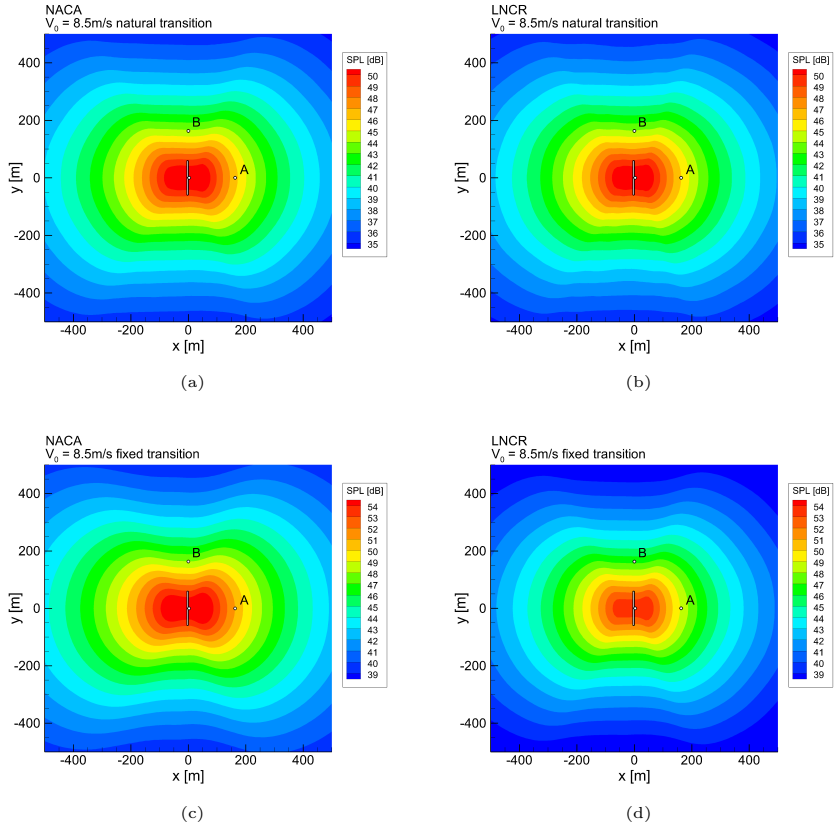

Figure 5.15: Overall sound pressure at ground level in the vicinity of the Turbine (tower height $H = 100\,\mathrm{m}$, turbine location at $x = 0$ and $y = 0$) for $V_0 = 8.5\,\mathrm{m/s}$: (a) NACA airfoil and natural transition; (b) LNCR airfoil and natural transition; (c) NACA airfoil and fixed transition and (d) LNCR and fixed transition.

The noise reduction in the fixed transition operation is equal for all directions around the turbine. This is depicted in the angular plot shown in Figure 5.16 (a). It also shows the

equal sound distribution for the natural and fixed transition case where the same overall levels can be found for every direction around the turbine. A closer look on the noise values for different azimuthal rotor positions (equivalent to the noise immission over time) is taken in Figure 5.16 (b). The behavior for the two positions is identical for the NACA and LNCR airfoil. At the downwind (A) position a constant noise value can be found which is independent of the rotor position, while at the crosswind position (B) higher fluctuations can be seen. However, for the fixed transition case the amplitude of the fluctuations is smaller for the LNCR airfoil (3.0 dB ranging between 45.5 dB and 48.5 dB) compared to the original NACA airfoil (4.5 dB ranging between 45.5 dB and 50.0 dB). This means, that the noise optimized airfoil also reduces fluctuations due to the rotation of the blades and thus might help to remedy the problem of amplitude modulation. For the natural transition case, again an identical performance can be found.

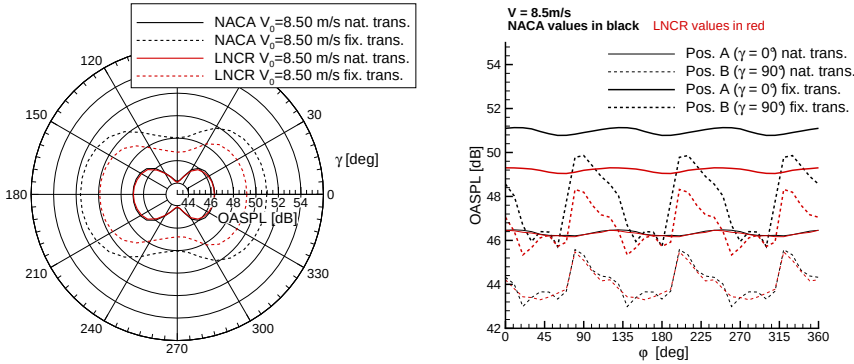

(a) (b)

Figure 5.16: Overall sound pressure level at the ground (distance of $R_1 = 163\,\mathrm{m}$) for a wind speed of $V_0 = 8.5\,\mathrm{m/s}$: (a) around the turbine; (b) for downwind (A) and crosswind (B) position and different rotor positions φ.

The results achieved for the modification of the NREL turbine rotor blades have shown two major things. First, the tools developed from the 2D CFD and CAA analysis are suitable for predicting the influences of geometry variations on aerodynamic as well as aeroacoustic scales. Second, a benefit in terms of noise reduction can be achieved if the conclusions drawn from the two-dimensional airfoil analysis are used to design new (low-noise) airfoils. Even more, the analysis revealed that this noise reduction can be achieved without drawbacks of the aerodynamic performance of wind turbine. Note, that the chosen new airfoil design thought to enhance the acoustic performance is only based on the relations found for the boundary layer turbulence values and that the geometry modification was done by hand. An optimization approach might lead to even better enhancements. However, it could be shown that a noise reduction in the fixed transition flow situation of around 1.8 dB is possible together with an increase of power in the dimension of one percent (and almost the same increase of annual energy production)

while the turbine loads are almost unchanged. Due to the very good performance of the NACA airfoil under natural transition conditions no benefit could be gained for this operation. Under real operating conditions the transition locations on the blade will depend on many different factors (inflow turbulence, surface quality, manufacturing tolerances, etc.) and will be somewhere in between the two extrema analyzed in this study. One might average the two states and come to the conclusion, that an average reduction of 1 dB can be achieved without negative influence on the performance. The benefit of this reduction is further discussed in Section 5.3. However, as the main focus was put on the demonstration of the used toolchain and not on the actual noise reduction by finding new airfoil geometries, the generated results are in a reasonable dimension. Using an optimization strategy which incorporates the shown tools might lead to even greater reductions.

5.2.3 Influence of Airfoil Performance on the overall Turbine Performance

Throughout the investigations a certain trend was found. Considering Figure 5.4 (b) it can be seen, that the the loss of power due to the change of the outer rotor blade airfoils from natural to fixed transition is only a few percent (less than 5 %). This seems kind of paradox, as the L-over-D ratio of the airfoils is almost halved by the forced transition (see Figure 5.5 (a)). So, against the common thinking the influence of the L-over-D ratio in the outer blade section does not seem to have the anticipated high influence on the overall turbine performance. Following Bak [82] an explanation for this behavior can be found using the blade element momentum method (refer to Section 2.1.1). For an annular blade element - rotating with the angular speed ω - the power coefficient C_p (Equation 2.4) can be rewritten to:

$$C_p = \frac{dF_t r\omega}{\frac{1}{2}\rho V_0^3 dA} = \left[(1-a)^2 + \lambda_{\mathrm{loc}^2}\left(1+a'\right)^2\right]\lambda_{\mathrm{loc}} c_t \sigma \ . \tag{5.3}$$

Assuming an ideal axial induction of $a = 1/3$ the equation shortens to:

$$C_p = \left[\frac{4}{9} + \lambda_{\mathrm{loc}^2}\left(1+a'\right)^2\right]\lambda_{\mathrm{loc}} c_t \sigma \ . \tag{5.4}$$

The solidity σ can also be expressed as:

$$\sigma = \frac{2\sin^2\Phi}{c_n} \tag{5.5}$$

and the local inflow angle Φ as:

$$\Phi = \arctan\left(\frac{1-a}{\lambda_{\mathrm{loc}}\left(1+a'\right)}\right) \ . \tag{5.6}$$

Together with the tangential and normal force coefficients (c_t and c_n from Equation 2.7 and 2.8) and the equation for the rotational induction factor a' (Equation 2.10) it is now possible to iteratively solve all equations with the dependency of a', c_t, c_n, σ and Φ. As a result the power coefficient of an annular element can be plotted as a function of the

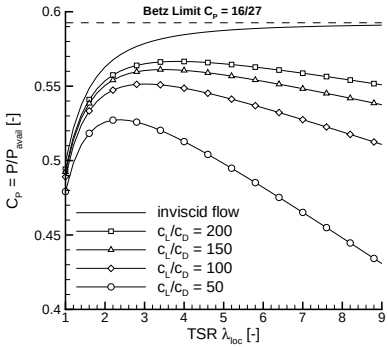

Figure 5.17: Local power coefficient for an annular element at different local tip speed λ_{loc} ratios for varying L-over-D ratio c_L/c_D.

local tip speed ratio λ_{loc} and the L-over-D ratio c_L/c_D of the section. This relation is depicted in Figure 5.17. Note, that ideal axial induction ($a = 1/3$) and zero tip loss are assumed.

In Figure 5.17 the power coefficient is plotted against the local tip speed ratio for different L-over-D ratios. It can be seen, that the highest glide ratio yields the highest power coefficient. For the inviscid flow situation ($c_D = 0$) the Betz limit ($C_P = 16/27$) can be reached. The local tip speed ratio can be interpreted as the radial position of the airfoil section. The higher relative speed (ωr) due to the radius position of the outer rotor blade sections results in higher values for λ_{loc}.

A reduction of the L-over-D ratio leads to a decrease of the maximum power coefficient of the section. This trend becomes stronger as the absolute values for c_L/c_D become lower. For example for an outer rotor blade section (assuming $\lambda_{\text{loc}} = 7$) the change of L-over-D ratio from $c_L/c_D = 200$ to $c_L/c_D = 150$ results in a 2 % decrease of C_p while the change from $c_L/c_D = 100$ to $c_L/c_D = 50$ yields a C_p reduction of 12 %. This explains why the rather large difference in glide ratio for the different transition settings only shows a reduced influence on the overall turbine performance. From a practical point of view the highest increases of the power coefficient can be reached if airfoils with small L-over-D ratios (e.g. $c_L/c_D < 100$) are improved. For high L-over-D ratio airfoils (e.g. $c_L/c_D > 100$) a further increase of the aerodynamic performance only yields minor improvements on the overall turbine scale. Considering the very high effort for designing airfoils with ultra high glide ratios (laminar boundary layer flow, low thickness etc.) this insight has to be kept in mind. Other structural parameters, like a high bending stiffness for airfoils with increased thickness, might justify the choice of an airfoil with a glide ratio around $c_L/c_D = 100$ as the gain with a higher glide ratio is rather small.

5.3 Benefit of Noise Reduction

Reducing wind turbine noise is also interesting from a more commercial point of view. The assumption is, that the actual noise reduction is not directly used to design a quieter turbine or wind farm, but instead is spend in other disciplines to yield a reduction of costs or an increase of energy production. Doing this, the question of the effective value of a noise reduction, of for example one decibel, can be answered. Using simple relationships some main aspects can be derived (see also Figure 5.18):

- **Amount of Turbines in a Wind Farm:** Considering a sound pressure level at a certain site generated by N incoherent and mutually uncorrelated sources (wind turbines set up in a wind farm), the summation of the single sound pressure levels L_p yields the total sound pressure level $L_{p,\text{total}} = 10\log\left(N \cdot 10^{L_p/10}\right)$. A reduction of L_p for each turbine could thus be used to increase the amount of turbines if the total sound pressure level $L_{p,\text{total}}$ is held constant: $\Delta L_p = 10\log\left(\frac{N_1}{N_2}\right)$. A reduction of 1 dB for each turbine theoretically yields an increase of 25 % of the total number of turbines in the wind farm. The profit of the wind farm directly scales with this figure, as more energy can be produced with the increased number of turbines.

- **Power Increase:** As stated in Equation 2.34 TBL-TEN scales with the fifth power of the flow velocity. A noise reduction could be traded against an increase of the turbine tip speed v_{tip} with the relation: $\Delta L_p = 10\log\left(\frac{v_{\text{tip1}}}{v_{\text{tip2}}}\right)^5$. If the rotational speed of the turbine is held constant (ω = const.), a longer rotor blade could be built ($v_{\text{tip}} = R\omega$). As the turbine power scales linear with the rotor area ($P \sim A$) a noise reduction of 1 dB could be used for a power increase of roughly 10 % when longer rotor blades are used and the same sound power level as before should be reached. Again, this figure can directly be added to the turbine's revenue, but higher loads and more material need to be considered.

- **Load Reduction:** Contrary to the point above, the tip speed influence of the noise reduction could also be used for a reduction of loads if the turbine power and the blade length are held constant. Due to $P = M\omega$ a noise reduction can be used to increase the tip speed by increasing the angular rotor speed ω. A reduction of 5 % of the rotor torque M can be utilized if the turbine noise can be reduced by 1 dB. The rotor torque is the main driver for the dimensioning loads of the main shaft, the gearbox and all connected parts e.g. bearings. Thus, a load reduction would directly reduce the dimensions of these parts and finally their cost.

- **Observer Distance to the Turbine:** Another benefit of noise reduction can be seen from Equation 5.1. Disregarding damping effects in the medium, the sound pressure level decreases quadratically with the distance from the turbine: $\Delta L_p = 10\log\left(\frac{|r_2|}{|r_1|}\right)^2$. Consequently, if a wind turbine site is influenced by a certain noise level at a distinct location, a noise reduction of the turbine could be used to reduce the distance between the turbine and the location by maintaining a constant noise immission. A distance reduction of 10 % is possible with a noise reduction of 1 dB. New wind farm areas especially in noise sensitive surroundings can be conquered this way.

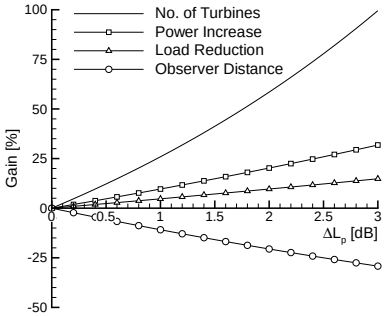

Figure 5.18: Relationships showing the benefit of a distinct noise reduction for different disciplines.

Note, that the facts stated above are derived from a merely commercial point of view. The benefit in terms of noise reduction could - of course - also be used to design quieter turbines with almost the same power and load characteristics as before and thus decrease noise immissions for the annoyed residents in near wind farm areas. But, as long as the legislation is not adapted to newer and quieter designs and the old thresholds for noise immissions hold the allowed limits might be exploited as described.

6 Conclusions and Future Work

This thesis is the result of over three years of progressive work in the field of wind turbine acoustics and aerodynamics. It started with the main objective to better understand the wind turbine noise issue and to find a simulation method which is suitable for the work in an industrial environment and can be used for design purposes. As such, the method needed two main cornerstones. First, it had be computationally efficient, meaning a turn-around-time of less than 24 hours when applied on common hardware. Second, the results had to be reliable and the method needed to be capable to predict the influence of even subtle geometric changes to the object under investigation.

The main noise driver for modern wind turbines was identified to be turbulent boundary layer trailing-edge noise. For its simulation within the scope of the stated cornerstones, the hybrid CFD/CAA method developed by DLR was adapted for the use in an airfoil design toolchain. Compared to semi-empirical methods, which are based on reference measurements, the hybrid approach shows a better result quality and a better agreement with experimental results, especially for airfoil shapes dissimilar of the reference NACA0012 shape. Compared to high fidelity LES or DNS simulations, the computational effort is much lower (e.g. less than 20 hours for a complete CFD and CAA simulation using 14 CPU hardware) particularly at the relatively high Reynolds numbers.

The used method for the airfoil noise prediction consists of a RANS CFD simulation from which the main aerodynamic properties of the airfoil can be extracted. Moreover, the flow velocity vector as well as the pressure and density distribution around the airfoil are used as the background flow in a subsequent CAA simulation with the code `PIANO`. Aeroacoustic sources due to the presence of convecting turbulent eddies within the airfoil boundary layer are realized using the FRPM stochastic turbulence reconstruction method. FRPM was fed with turbulence statistics from the two equation turbulence model of the RANS computations. Throughout intensive testing, a best practice setup for all incorporated tools was found which showed the best agreement of the simulated far-field noise spectra with available measurement data.

For the CFD simulations a computational mesh with 100000 cells could be used with good accuracy. The SST-k-ω turbulence model had shown a good performance in terms of the prediction of viscous effects. Thus, the aerodynamic coefficients of the airfoil could be calculated. Furthermore, the simulated turbulence statistics were in agreement with measurement data and suitable for the stochastic turbulence reconstruction with the FRPM method. For the two-dimensional CAA mesh, a finer resolution with a total number of one million cells was needed to cover the source region and the airfoil surrounding where the noise data was evaluated. During the simulations the influence of the FRPM source strength weighting function ($w(x)$) was identified as an important parameter towards the production of artificial noise. A smoother weighting function of the form $w(x) \sim sin^2(x)$ was suggested which almost remedied the artificial noise problem. Moreover, the minimum patch cell size was found to be at least one fourth of minimum

resolved turbulent length scale ($l_{\min}$), to correctly reproduce the high frequency part of the noise spectrum.

After finding the best possible settings for each step in the airfoil acoustic simulation toolchain, a lot of effort was spend on the automation and scripting of the procedure. Several Linux shell scripts and Python routines were developed which govern the automation of the mesh generation, the setup and data gathering of the CFD simulation, the post processing of the CFD results in terms of aerodynamic coefficient determination as well as in preparing the flow data for the subsequent CAA step and other major parts in the analysis. Moreover, the CAA mesh is created from an automatic script using the same input geometry as for the CFD mesh. All files needed for the `PIANO` and FRPM CAA run are gathered and prepared by a script. After the simulations are completed, another script is used for the post processing and the extraction of the relevant acoustic results. The use of automated scripts did not only accelerate the work and generate a greater amount of output, it also resulted in a quality enhancement, as it avoided user input errors e.g. by always generating computational meshes with the same input data, cell sizes and blocking strategy for the different cases. Errors due to the use of wrong input data, especially for the CAA simulations where a lot of different files are needed, could be completely reduced. Thanks to the semi-automized two-dimensional airfoil simulation chain it was possible to evaluate a lot of geometries at several different flow conditions.

Comparing the simulated results to available measurement data from the BANC-II workshop emphasized the validity of the used approach. It was shown, that throughout all frequencies covered by the measurements the simulations were able to reproduce the experimental data within the given uncertainty range. Basic physical relations, e.g. between the angle of attack and the form of the far-field noise spectrum were correctly simulated. For the NACA0012 simulation under six degrees angle of attack the two separate spectra from suction side (thick boundary layer - low frequencies) and pressure side (thin boundary layer - high frequencies) could be solely simulated in individual simulations and later on superimposed to indeed yield the same result as for the simulation of the complete case and also the same result as in the measurements. The mentioned increase in result quality could clearly be shown for the wind turbine designed DU-96 airfoil, where the hybrid CFD/CAA approach showed a good alignment with the measured spectra in contrast to the NACA-calibrated semi-empirical BPM method.

After showing the validity of the chosen approach the toolchain was used to evaluate the design driving parameters for airfoil trailing-edge noise. For this purpose the geometry of the DU-96 airfoil was systematically varied. The four-digit NACA series approach was adapted for this task. In a first step the geometry was bent back to its symmetrical shape. Thereafter, the NACA mean-line function was calculated for a specific amount of camber and a desired camber position. This mean-line was then used to modify the thickness-scaled symmetric DU airfoil to a new shape with the appropriate values. For a holistic comparison of the data it was important to not only judge an airfoil by its overall noise emission at a certain reference position. Even as import as the acoustic performance was the look on the aerodynamic performance. The objective was to find an airfoil shape which shows a low noise emission but also a high aerodynamic grade in terms of L-over-D ratio (c_L/c_D) and lift coefficient (c_L). Closest to this objective came a strongly cambered thickness-reduced version of the DU-96 airfoil. For a chosen L-over-D ratio, the noise levels of all analyzed airfoils varied in the range of three to five decibels. This clearly underlined the fact, that the same aerodynamic performance could

be generated under different noise emissions and that an acoustic enhancement is thus possible. Moreover, the influence of the very important laminar to turbulent boundary layer transition was investigated. For cases where the transition was fixed close to the airfoil nose (e.g. representing the operation under with an uneven surface due to dirt adhesive or erosion), higher noise levels were emitted and the overall noise was increased by as much as four decibels while the aerodynamic performance in terms of L-over-D ratio dropped by almost 50 % due to the increased airfoil drag. As this is a severe influence and it is further hard to set a transition location in accordance with real wind turbine operations, all subsequent results were calculated for a nose-region fixed transition (worst case scenario) as well as the natural transition case (best case scenario).

The availability of a whole lot of simulation data from CFD and CAA calculations for different airfoils under several flow conditions, made it possible to draw conclusions between the relevant flow parameters and their influence on the aeroacoustics. Relevant boundary layer parameters were extracted and compared to the far-field noise immissions. It was found, that the maximum value of the turbulence kinetic energy in the usually thicker (positive angle of attack implied) suction side boundary layer at the trailing-edge almost directly predicts the overall far-field sound pressure level. A relationship between this value and the acoustic pressure in the far-field was shown which can be used for predictions within the accuracy of 0.8 dB. Moreover, beside the value also the distance of the maximum TKE from the trailing-edge needs to be considered. The closer this maximum moves to the TE, the more efficient becomes the TBL-TEN source. Identifying the main noise driving aspects it was possible to formulate some major recommendations for a low-noise airfoil design:

- The turbulence levels within the suction side boundary layer should be as low as possible (soft pressure regain, concave surface shape in the back of the suction side).
- Other areas than the aft part of the suction side should be used to compensate the loss of lift production (e.g. shift more load to the pressure side by using a rear-loading).
- More lift should be generated in the forward part of the airfoil and the minimum c_p values should be kept low (absolute) to avoid a to steep slope of the pressure regain at the suction side.
- The position of the laminar turbulent transitions needs to be considered as it has a severe influence on the TKE levels within the boundary layer and thus the aerodynamic as well as aeroacoustic performance of the airfoil.

Beside the two-dimensional analysis it was planned to continue the study with a three-dimensional modeling approach, to evaluate the acoustic performance, not only of rotor blade airfoils, but for a whole three-dimensional section of the blade and finally the whole turbine. First tests showed, that this was only possible by using massive computational resources, even for a relative small 3D extrapolation of a NACA0012 test case. As this demand for resources was outside the scope of the preferred industrial fast and reliable mantra, an alternative strategy was developed to generate results for a complete wind turbine. Therefore, the classic blade element momentum theory, which is a standard for aerodynamic examinations of whole wind turbines, was coupled with the developed two-dimensional toolchain. Simulations were conducted for the relevant 2D rotor blade sections. The aerodynamic data (lift and drag coefficients) was used to feed the BEM from which local angles of attack as well as other relevant operating parameters to determine

the relevant acoustic data (from previously conducted CAA simulations) were calculated. Using the acoustic information plus the geometric information of the relative position from the rotor blade sections towards a ground based observer at an arbitrary position, it was possible to calculate the directivity influence. Moreover, an appropriate scaling for each section's geometric extensions (local chord lengths) and flow speed was done and the emission of all seperate sections from the three blades were superposed in the observer position. This combined procedure yielded the acoustic immission at the observer position plus a lot of turbine performance data from the BEM e.g. the power curve or the development of the blade root bending moment over different wind speeds. With the method, noise maps for the trailing-edge noise emission in the vicinity of the wind turbine could be calculated.

The described turbine simulation procedure was tested with available data from the NREL 5 MW reference turbine. Setting up the BEM and acoustic calculations, the baseline values for this turbine could be calculated. In a second step the main outer rotor airfoil (NACA64618) was exchanged by a self-modified low noise airfoil, the LNCR-18 airfoil. The geometry of the LNCR airfoil was made by hand using the mentioned key facts for a low noise airfoil design. As the NACA airfoil showed a quite good performance under natural transition conditions no improvement could be gained here. But also no deterioration was present and the performance (acoustically and aerodynamically) remained almost unchanged by the new airfoil. In fact, the flapwise bending moment could even be reduced on the order of three percent. The main advantages of the low noise airfoil design came into play in the fixed transition case. Here, a noise reduction on the order of two decibels over the complete frequency range of interest was achieved without influencing the aerodynamic performance of the blade. The turbine power was even increased by one percent and the flapwise bending moment remained untouched (-0.3 %). Under real turbine operating conditions, this case is also closer to reality due to dirt and disturbances which are always present on the blade surface and lead to earlier transition. Generally speaking, a noise reduction in the range of one decibel with a manually shaped airfoil represents a truly significant advantage. Note, that so far no optimization techniques were used, which are thought to generate an even higher noise reduction. Nevertheless, a noise reduction of even only one decibel is quite valuable in a wind turbine design case. The noise reduction could help winning noise sensitive projects with the turbine where often every single dB counts. For immission based regulations it could help to either put more (quieter) wind turbines in a certain wind farm or even reduce the distance to the immission point but still keep the threshold levels set by legislation.

The main outcomes of this thesis are the used tool-chains and tools which allow the wind turbine designer to previously evaluate the noise emission of a planned new turbine. In an early stage of the design, these tools help to choose the correct airfoils for which ever constraints (aerodynamic or acoustically) are present. For short notice the main results are grouped in the following list:

- Development of a combined aerodynamic and acoustic toolchain on airfoil and turbine level with an appropriate best practice setup and validated results.
- Extraction of the main noise driving parameters in the airfoil design.
- Identification of useful aerodynamic parameters which can be generated throughout a simple CFD simulation and their influence towards TBL-TEN.
- Design of an example low-noise airfoil.

- Improvement of the baseline wind turbine in terms of acoustics without any aerodynamic drawbacks.

6.1 Impact of Results on Next-Generation Turbines

Throughout the wind turbine industry a clear trend can be found. Each new turbine generation is not only bigger than the one before (concerning overall dimensions, rated power, etc.), it also comprises newly developed technologies as well as new insights gained by progressive research and testing. Especially in the field of acoustics the results of this thesis can help to incorporate the evaluation of the turbine's noise emissions in an early stage of the rotor blade design. So far, the acoustic predictions in the design phase of a rotor blade were often limited to basic estimations mainly based on the tip speed and the fifth-power law. Noise measurements of actual turbines helped to tune these simple estimations, but only to a limited extend. Using semi-empirical prediction codes eased the situation a little bit, but due to the inaccuracy for non-NACA-similar airfoils they were not able to correctly predict geometric changes in the airfoil design with a credibility demanded. Often, the reliable statements on the acoustic performance could only be made after the first prototype was built. Errors, for example a too noisy design could thus primarily be seen at this very advanced project stage. This led to the situation, that in order to avoid a costly reworking a more conservative design approach was used. Thus, safety margins were often quite high and the resulting output of the turbine (in terms of actual power output or even load reduction) was lower than possible. A reliable prediction tool can tackle this issue and help judging design decisions in the early stages of a new rotor blade design process. The shown toolchain can be used on an airfoil as well as turbine level to support the work in this field. Moreover, the shown relationships of boundary layer turbulence data can be used in simpler models to quickly judge the performance on a noise emission scale. Using the turbine noise prediction technique, specific noise maps can be calculated for every single point of operation. This allows a better coordination of the turbine control as well as the turbine positioning for the agreement with local regulations. As discussed, the acoustic benefits can be spend in different ways.

Condensed, the basic advantages of the presented work on new turbine generations might be:

- Incorporating the acoustic predictions into the design of new rotor blades on a highly validated level.
- Reducing security margins due to the better understanding and prediction of the design and thus gaining more yield.
- Selective acoustic enhancement of rotor blades (optimization).
- Judging of the effects of noise reduction or increase on the aerodynamic performance of the rotor blade.

6.2 Outlook

For progression in the field of wind turbine aeroacoustics it would make sense to spend more effort on the extension of the presented hybrid approach towards a three-dimensional cases. As shown, this is actually possible but only with a high demand of computational resources. A better parallelization strategy might help here. The three-dimensional simulations are of major interest so far, as 3D flow effects, e.g. in the region of the blade tip and the related tip vortex were not covered by the presented two-dimensional toolchain. Also, it would be possible to judge other interesting noise effects if a reliable three-dimensional method would be available. This would for example include the simulations of vortex generators which are often used on the rotor blade airfoils to avoid a too early flow separation by introducing higher momentum air flow into the boundary layer through a vortex. Moreover, noise mitigation devices, for example trailing-edge serrations could be analyzed to better understand their noise mitigation effect and to quantify their impact in the overall blade noise emissions. Geometric design studies would be possible.

Another interesting field to use the shown methods of this thesis would be the field of optimization. Due to the massive use of automation procedures, the method is either on airfoil as well as on full turbine scale prone to be used within an optimization process, to e.g. find the airfoil design with the least noise but best aerodynamic performance. A lot more parameters than presented within this work could be tested towards their influence on trailing-edge noise as well as other competing disciplines. Considering the actual work, engineering knowledge, as well as the setup of robust and reliable toolchains were higher prioritized than a geometry study driven by an optimization with a few hundred or thousand designs. In the mind of the author, this is the more trustful way to go which also has the higher impact considering the understanding of relevant features and the overall context. Nevertheless, a fully automized optimization procedure might help to find the last bit of noise reduction and add the last few percent on the power generation, which from a purely cost driven industrial view are still worth to be found.

A Appendix

A.1 Derivation of the BEM Method

In addition to the deliberations in Section 2.1, a more detailed view on the derivation of the BEM method in accordance with Reference [33] will be given here.

First, the 1D momentum theory is applied to an annular control volume with the radius r and the spanwise extension dr intersecting the rotor disc. For the intersection area $(2\pi r dr)$ thrust dT (force in wind direction acting against the rotor) and torque dM (torque around the axis of rotation driving the rotor) can be derived:

$$dT = 4\pi r \rho V_0^2 a\,(1-a)\,dr\ , \tag{A.1}$$

$$dM = 4\pi r^3 \rho V_0 \omega a\,(1-a)\,a' dr\ . \tag{A.2}$$

From Figure 2.3 it can be seen, that the flow angle Φ depends on the wind speed V_0, the speed ωr due the rotation and the induction factors a and a':

$$\tan\Phi = \frac{(1-a)\,V_0}{(1+a')\,\omega r}\ . \tag{A.3}$$

The angle of attack α is:

$$\alpha = \Phi - \Theta\ . \tag{A.4}$$

Where the local pitch $\Theta = \Theta_p + \beta$ is a combination of the pitch angle of the blade Θ_p (which can be varied through the pitch system) and the local twist angle β(implemented in the rotor blade design). From the known aerodynamic coefficients c_L and c_D of the section the forces can be calculated:

$$L = \frac{\rho}{2} V_{rel}^2 l_c c_L \tag{A.5}$$

and:

$$D = \frac{\rho}{2} V_{rel}^2 l_c c_D\ . \tag{A.6}$$

The projection into a coordinate system normal and tangential to the rotor plane yields:

$$F_n = L\cos\Phi + D\sin\Phi \tag{A.7}$$

and:

$$F_t = L\sin\Phi - D\cos\Phi\ . \tag{A.8}$$

Applying a normalization with respect to $\frac{\rho}{2} V_{rel}^2 l_c$ yields:

$$c_n = c_L\cos\Phi + c_D\sin\Phi \tag{A.9}$$

and:

$$c_t = c_L \sin\Phi - c_D \cos\Phi \ . \tag{A.10}$$

Where the coefficients c_n and c_t are:

$$c_n = \frac{F_n}{\frac{\rho}{2} V_{rel}^2 l_c} \tag{A.11}$$

and:

$$c_t = \frac{F_t}{\frac{\rho}{2} V_{rel}^2 l_c} \ . \tag{A.12}$$

Now, normal force (thrust) and torque on the control volume of the thickness dr can be calculated using the local forces F_n and F_t:

$$dT = B F_n dr \ , \tag{A.13}$$

$$dM = r B F_t dr \ . \tag{A.14}$$

B denotes the number of blades. Introducing Equation A.11 into Equation A.13, with the relation for the relative velocity $V_{rel} \sin\Phi = V_0 \left(1 - a\right)$ seen in Figure 2.3, the thrust becomes:

$$dT = \frac{\rho}{2} B \frac{V_0^2 \left(1 - a\right)^2}{\sin^2 \Phi} l_c c_n dr \ . \tag{A.15}$$

For the torque analogously Equation A.12 is combined with Equation A.14 and the velocity relation $V_{rel} \cos\Phi = \omega r \left(1 + a'\right)$ which yields:

$$dM = \frac{\rho}{2} B \frac{V_0 \left(1 - a\right) \omega r \left(1 + a'\right)}{\sin\Phi \cos\Phi} l_c c_t r dr \ . \tag{A.16}$$

If now the Equations A.1 and A.15 or respectively A.2 and A.16 are equalized, formulations for the induction factors a and a' are found:

$$a = \frac{1}{\frac{4 \sin^2 \Phi}{\sigma c_n} + 1} \ , \tag{A.17}$$

$$a' = \frac{1}{\frac{4 \sin\Phi \cos\Phi}{\sigma c_t} - 1} \ . \tag{A.18}$$

Herein σ denotes the solidity:

$$\sigma(r) = \frac{l_c(r) B}{2\pi r} \ . \tag{A.19}$$

With the above derived formulas it is now possible to set up an iterative algorithm to compute the local forces and induction factors for each control volume. After choosing the wind speed V_0 and the rotational speed of the turbine ω, the induction factors are initialized (typically $a = a' = 0$). The procedure then looks as follows:

- Use Equation A.3 to calculate Φ and Equation A.4 to calculate α
- Look up the know aerodynamic coefficients c_L and c_D which are calculate the separately (e.g. with panel method or a numerical procedure (CFD)

- Compute c_n and c_t from Equation A.9 and A.10
- Use Equation A.17 and A.18 to calculate a and a'

The above described steps are repeated until the change of the induction factors is within the desired limit. By then, the local loads and forces of the blade segment can be computed. The integration of the segments over the blade radius R yields the global parameters such as the mechanical power, thrust or the bending moment of the blade in edge-wise or flap-wise direction.

Prandtl's Tip Loss Factor

Prandtl found, that a correction for a finite number of blades needs to be applied in order to account for the vortex system in the wake behind the turbine. Therefore he derived the correction factor:

$$F = \frac{2}{\pi} \cos^{-1} \left(e^{-\frac{B(R-r)}{2r \sin \Phi}} \right) . \tag{A.20}$$

It is introduced into Equations A.17 and A.18 which yields:

$$a = \frac{1}{\frac{4F \sin^2 \Phi}{\sigma c_n} + 1} , \tag{A.21}$$

$$a' = \frac{1}{\frac{4F \sin \Phi \cos \Phi}{\sigma c_t} - 1} . \tag{A.22}$$

Glauert Correction

For axial induction factors larger than approximately 0.4, the mometum theory breaks down [33] and a correction needs to be applied. An empirical approach was shown by Spera [83] where the formulation for the tangential load coefficient is modified:

$$c_t = \begin{cases} 4a\left(1-a\right)F & \text{for } a \leq a_c \\ 4\left(a_c^2 + \left(1-2a_c\right)a\right)F & \text{for } a > a_c \end{cases} \tag{A.23}$$

By that, Equations A.17 changes to:

$$a = \begin{cases} \frac{1}{\frac{4F \sin^2 \Phi}{\sigma c_n} + 1} & \text{for } a \leq a_c \\ \frac{1}{2}\left[2 + K\left(1-2a_c\right) - \sqrt{\left(K\left(1-2a_c\right)+2\right)^2 + 4\left(Ka_c^2 - 1\right)}\right] & \text{for } a > a_c \end{cases} \tag{A.24}$$

with:

$$K = \frac{4F \sin^2 \Phi}{\sigma c_n} . \tag{A.25}$$

Wind speed distribution

The probability density function can be expressed by a Rayleigh (h_r) or Weibull (h_w) distribution[33]. The Rayleigh distribution can be used for general side under standard conditions while the Weibull distributions can be adjusted (through a scaling factor A and a form factor k) to specific conditions depending on the local site (vegetation, landscape, etc.).

$$h_w\left(V_0\right) = \frac{k}{A}\left(\frac{V_0}{A}\right)^{k-1} \exp\left(-\left(\frac{V_0}{A}\right)^{k}\right) \tag{A.26}$$

$$h_r\left(V_0\right) = \frac{\pi}{2}\frac{V_0}{\overline{V}^2} \exp\left(-\frac{\pi}{4}\left(\frac{V_0}{\overline{V}}\right)^{2}\right) \tag{A.27}$$

For standardization the International Electrotechnical Commission (IEC) defined different wind classes with respective mean wind velocities (see Table A.1). As an example the standard Rayleigh distributions for the four IEC classes are depicted in Figure A.1.

Table A.1: IEC Wind Classes.

IEC class	$\overline{V}[m/s]$
I	10.0
II	8.5
III	7.5
IV	6.0

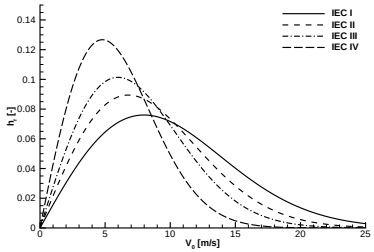

Figure A.1: Rayleigh distribution of the wind speed for the different IEC classes according to Equation A.27.

A.2 Governing Equations

Navier-Stokes equations in conservative integral form (non-moving control volume) as implemented in the DLR Tau code[40]:

$$\frac{\partial}{\partial t}\iiint_V \vec{W} = -\iint_{\partial V} \boldsymbol{F}\cdot\vec{n}dS \tag{A.28}$$

With the vector of conserved quantities $\vec{W}$:

$$\vec{W} = \begin{pmatrix} \rho \\ \rho u \\ \rho v \\ \rho w \\ \rho E \end{pmatrix} \tag{A.29}$$

The flux density tensor $\boldsymbol{F}$ with inviscid (index i) and viscid (index v) flux vectors $\vec{F}$, $\vec{G}$ and $\vec{H}$ (superscript c indicates the convective nature of the terms):

$$\boldsymbol{F} = \left(\vec{F}_i^c + \vec{F}_v^c\right)\cdot\vec{e}_x + \left(\vec{G}_i^c + \vec{G}_v^c\right)\cdot\vec{e}_y + \left(\vec{H}_i^c + \vec{H}_v^c\right)\cdot\vec{e}_z \tag{A.30}$$

The viscous and invicid fluxes:

$$\vec{F}_i^c = \begin{pmatrix} \rho u \\ \rho u^2 + p \\ \rho uv \\ \rho uw \\ \rho Hu \end{pmatrix}, \vec{F}_v^c = \begin{pmatrix} 0 \\ \tau_{xx} \\ \tau_{xy} \\ \tau_{xz} \\ u\tau_{xx} + v\tau_{xy} + w\tau_{xz} + k\frac{\partial T}{\partial x} \end{pmatrix} \tag{A.31}$$

$$\vec{G}_i^c = \begin{pmatrix} \rho v \\ \rho uv \\ \rho v^2 + p \\ \rho vw \\ \rho Hv \end{pmatrix}, \vec{G}_v^c = \begin{pmatrix} 0 \\ \tau_{xy} \\ \tau_{yy} \\ \tau_{yz} \\ u\tau_{xy} + v\tau_{yy} + w\tau_{yz} + k\frac{\partial T}{\partial y} \end{pmatrix} \tag{A.32}$$

$$\vec{H}_i^c = \begin{pmatrix} \rho w \\ \rho uw \\ \rho vw \\ \rho w^2 + p \\ \rho Hw \end{pmatrix}, \vec{H}_v^c = \begin{pmatrix} 0 \\ \tau_{xz} \\ \tau_{yz} \\ \tau_{zz} \\ u\tau_{xz} + v\tau_{yz} + w\tau_{zz} + k\frac{\partial T}{\partial z} \end{pmatrix} \tag{A.33}$$

The equation of state for the pressure p:

$$p = (\kappa - 1)\,\rho\left(E - \frac{u^2 + v^2 + w^2}{2}\right) \tag{A.34}$$

The temporal change of the conservative variables $\vec{W}$ can be derived from Equation A.28 as:

$$\frac{\partial}{\partial t}\vec{W} = \frac{\iint_{\partial V} \boldsymbol{F} \cdot \vec{n} dS}{\iiint_{V} dV} \ . \tag{A.35}$$

It can be seen, that the the change of the flow conditions is related to the fluxes over the volume boundary ∂V and its size V. For a control volume fixed in time and space Equation A.35 changes to:

$$\frac{d}{dt}\vec{W} = -\frac{1}{V} \cdot \vec{Q}^F \ . \tag{A.36}$$

The vector $\vec{Q}^F$ represents the fluxes over the control volume boundaries. Dividing the boundary into n faces leads to:

$$\vec{Q}^F = \sum_{i=1}^{n} \vec{Q}_i^F = \sum_{i=1}^{n} \left(\vec{Q}_i^{F,c} - \vec{D}_i \right) \ . \tag{A.37}$$

Inviscid fluxes over the representative face are denoted by $\vec{Q}_i^{F,c}$, additional dissipative terms with $\vec{D}_i$. With the determination of the convective fluxes over the control volume boundaries the temporal change of the flow quantities inside the volume can be determined. For upwind solving schemes the $\vec{D}_i$ terms are zero, for central schemes additional dissipation has to be computed.

A.3 From Governing Equations to Wave Equation

Starting from the continuity and the momentum equation (2.11 and 2.12) in Section 2.2, the homogenous wave equation (without right hand side source terms) can be derived. After the neglection of the mass flow $\dot{m}$ the time-derivative of Equation 2.11 yields:

$$\frac{\partial^2 \rho}{\partial t^2} + \frac{\partial}{\partial t} \nabla \cdot (\rho \vec{v}) = 0 \ . \tag{A.38}$$

From the momentum equation (2.12) the divergence is taken (mass flow, external forces and viscous friction neglected).

$$\frac{\partial}{\partial t} \nabla \cdot (\rho \vec{v}) + \nabla \cdot \nabla \cdot (\rho \vec{v} \vec{v}) + \nabla \cdot \nabla p = 0 \tag{A.39}$$

Equation A.39 is subtracted from Equation A.38 which yields:

$$\frac{\partial^2 \rho}{\partial t^2} - \nabla \cdot \nabla \cdot (\rho \vec{v} \vec{v}) - \nabla \cdot \nabla p = 0 \ . \tag{A.40}$$

The variables are split into a steady mean flow part (subscript 0) and a small fluctuating part (superscript $'$).

$$p = p_0 + p', \ \rho = \rho_0 + \rho', \ \vec{v} = \vec{v}_0 + \vec{v}' \tag{A.41}$$

With these terms Equation A.40 then becomes:

$$\frac{\partial^2 \left(\rho_0 + \rho'\right)}{\partial t^2} - \nabla \cdot \nabla \cdot \left(\left(\rho_0 + \rho'\right)\left(\vec{v}_0 + \vec{v}'\right)\left(\vec{v}_0 + \vec{v}'\right)\right) - \nabla \cdot \nabla \left(p_0 + p'\right) = 0 \ . \quad \text{(A.42)}$$

It can now be linearized by neglecting products of small quantities (indicated by supersript $'$). Additionally, the mean pressure and density p_0 and ρ_0 are supposed to be constant and the medium is at rest ($\vec{v}_0 = 0$). Equation A.42 therefore becomes:

$$\frac{\partial^2 \rho'}{\partial t^2} - \nabla \cdot \nabla p' = 0 \ . \quad \text{(A.43)}$$

Now, the relationship of the fluctuating acoustic density ρ' and the acoustic pressure p' as given in Equation 2.26 can be used which yields the homogeneous wave equations for the acoustic pressure:

$$\frac{\partial^2 p'}{\partial t^2} \frac{1}{c_0^2} - \Delta p' = 0 \ . \quad \text{(A.44)}$$

The Laplacian operator $\Delta = \nabla \cdot \nabla$ is used to shorten the equation.

A.4 Realizing a Liepmann Turbulence Spectrum with FRPM

The following section describes the realization of of Liepmann turbulence spectrum by the superposition of different scaled FRPM realizations according to the procedure described in Reference [70].

It is supposed that the decrease of the far-field sound pressure level spectrum is linked to the form of the realized turbulent energy spectrum $E(k)$ provided by FRPM. A different form of the energy spectrum can be achieved by a superposition of different FRPM stochastic fields, each generated from independent random particle representations and different length scales per field. Therefore, each realization is scaled with a length scale dependent weighting function. Since the different FRPM realizations are mutually uncorrelated, it means that the realized turbulent spectra for each length scale can simply be superposed.

Each FRPM realization of a specific length scale realizes a turbulent Gaussian spectrum E_G of the form:

$$E_G(k, l) = \frac{8 k_t k^4 l^5}{3\pi^3} \exp\left(-\frac{k^2 l^2}{\pi}\right). \quad \text{(A.45)}$$

Here k_t denotes the turbulence kinetic energy, k is the wave number, and l the integral length scale of the Gaussian spectrum. The Gaussian spectrum is normalized such that its integral over all wave-numbers is one for $k_t = 1$, i.e.

$$\int_0^\infty E_G(k)|_{k_t=1} \, dk = 1. \quad \text{(A.46)}$$

The aim is to find a weighting function (variance for each length scale) $f(l)$ to realize:

$$E(k) = \int_0^\infty f(l) \ E_G(k, l)|_{k_t=1} \, dl = \frac{8k^4}{3\pi^3} \int_0^\infty f(l) l^5 \exp\left(-\frac{k^2 l^2}{\pi}\right) dl \ . \quad \text{(A.47)}$$

With the substitution $l^2/\pi = 1/2\sigma^2$ and $dl = -\sqrt{\pi/8}/\sigma^3\, d\sigma^2$ the integral is written in a form suitable for Gaussian transformation as introduced by Alecu et al.[84],

$$p(k) = \frac{E(k)}{k^4} = \int_0^\infty \underbrace{\frac{\sqrt{2\pi}}{6\sigma^7} f\left(\frac{\sqrt{\pi/2}}{\sigma}\right)}_{\mathcal{G}(\sigma^2)} \underbrace{\frac{1}{\sqrt{2\pi}\sigma} \exp\left(-\frac{k^2}{2\sigma^2}\right)}_{\mathcal{N}(x|\sigma^2)} d\sigma^2. \tag{A.48}$$

Hence, from the Gaussian transform $\mathcal{G}(\sigma^2)$ the weighting function derives as

$$f\,(l) = \frac{6\sigma^7}{\sqrt{2\pi}}\mathcal{G}(\sigma^2), \quad \text{with} \quad \sigma = \frac{\sqrt{\pi/2}}{l}. \tag{A.49}$$

The weighting function $f(l)$ is the variance realized by the FRPM field with length scale l. Hence, that amplitude used in FRPM must be $\propto \sqrt{f(l)}$ (and therefore $f(l)$ must be positive).

Besides the Gaussian spectrum Liepmann[71] proposed a different form of the energy spectrum E_L, with a much shallower decay of turbulence energy towards higher wavenumbers. This drives the assumption, that with a realized Liepmann spectrum a benefit in the simulation of sound pressure levels in the higher frequencies could be achieved. Thus, a solution was searched to implement this feasibility into the FRPM approach with its Gaussian realization with the above stated method. From the Liepmann spectrum

$$E_L(k) = \frac{16 k_t k^4 \Lambda^5}{3\pi\left(1+\Lambda^2 k^2\right)^3} \tag{A.50}$$

the left-hand side expression of Eq. (A.48) to be inverted by Gaussian transform becomes

$$p(k) = \frac{E(k)}{k^4} = \frac{16 k_t}{3\pi\Lambda} \frac{b^{2\nu}}{\left(b^2+k^2\right)^{\nu+2.5}}. \tag{A.51}$$

This is of the form of the generalized Cauchy distribution shown in the appendix of the Alecu paper[84] with $\nu = 2.5$ and $b = 1/\Lambda$. As shown there, the Gaussian transform is derived from the inverse Laplacian transform of $\mathcal{L}^{-1}(b^2+s)^{-3}$, with $b = 1/\Lambda$ and

$$\mathcal{L}^{-1}\left(f(s)\right) = \frac{1}{2\pi i}\int_{\epsilon-i\infty}^{\epsilon+i\infty} f(u) e^{ut} du. \tag{A.52}$$

The Laplacian transform yields $t^2/2\exp(-t/\Lambda^2)$, i.e. it is positive everywhere. Furthermore, the Gaussian transformation demands for replacing t by $t = 1/(2\sigma)^2$. This gives

$$\mathcal{G}(\sigma^2) = \frac{2k_t}{3\sqrt{2\pi}\Lambda\sigma^7} \exp\left(-\frac{1}{2\sigma^2\Lambda^2}\right) \tag{A.53}$$

Finally, this yields with the help of Eq. (A.49)

$$f(l) = \frac{2k_t}{\pi\Lambda} \exp\left(-\frac{l^2}{\pi\Lambda^2}\right). \tag{A.54}$$

Consequently, the Liepmann spectrum derives from the integral Eq. (A.47) with weighting Eq. (A.54) as

$$E(k) = \int_0^\infty \frac{16 k_t k^4 l^5}{3\pi^4 \Lambda} \exp\left(-\frac{l^2}{\pi \Lambda^2}\right) \exp\left(-\frac{k^2 l^2}{\pi}\right) dl. \tag{A.55}$$

This integral can be approximated by a summation over different realizations each with a different length scale l ranging from $l_{\min}$ to $l_{\max}$:

$$E_L(k) = \sum_{l=l_{\min}}^{l_{\max}} \frac{16 k_t k^4}{3\pi^4 \Lambda} l^5 \exp\left(-\frac{l^2}{\Lambda^2 \pi}\right) \exp\left(-\frac{k^2 l^2}{\pi}\right) \Delta l \ . \tag{A.56}$$

Therefore, the kinetic energy used in FRPM for each single realization is simply:

$$k_{t_{\mathrm{mod}}}(l) = f\,(l)\,\Delta l = k_t \frac{2\Delta l}{\pi \Lambda} \exp\left(-\frac{l^2}{\Lambda^2 \pi}\right) \ . \tag{A.57}$$

For practical use, the above derived weighting function for the turbulence kinetic energy $k_{t_{\mathrm{mod}}}(l)$ (where Λ represents the initial length scale distribution on the patch) will be used on multiple patches with different predefined length scales l ranging from the minimum non-dimensional length scale $l_{\min}$ to the maximum length scale $l_{\max}$. Between $l_{\min}$ and $l_{\max}$ steps with the distance of Δl need to be defined. Hence, $N = (l_{\max} - l_{\min})/\Delta l$ single FRPM calculations will be conducted and later on superposed to obtain the total spectrum. Note, the minimum length scale $l_{\min}$ depends on the resolution of the used computational grid in the source area. To avoid an under resolution $l_{\min}$ should have the size of at least four grid cells.

A test case was simulated with FRPM to check the abovementioned weighting function. The results are shown for isotropic turbulence wavenumber spectra Φ_{ij}. They can be determined by

$$\Phi_{ij} = \frac{E(k)}{4\pi k^2} \left(\delta_{ij} - (k_i k_j)/k^2\right) \ , \tag{A.58}$$

which yields

$$\Phi_{11}(k_1, k_2, k_3) = \frac{E(k)}{4\pi k^2} \left(1 - k_1^2/k^2\right) \ . \tag{A.59}$$

To obtain a one dimensional spectrum in dependence of the axial wavenumber k_1 the integration has to be performed over the wavenumber k_2 (normal) und k_3 (spanwise).

$$\Phi_{11}(k_1) = 4 \int_0^\infty \int_0^\infty \Phi_{11}(k1, k2, k3)\, \mathrm{d}k_2 \mathrm{d}k_3 \tag{A.60}$$

Substituting the Gauss spectrum from Eq. A.45 and the Liepmann spectrum from Eq. A.50 using $l = \Lambda$ as length scale parameter, this yields:

$$\begin{aligned} \Phi_{11\ G}(k_1) &= \frac{2 k_t \Lambda}{3\pi} \exp\left(-k_1^2 \Lambda^2/\pi\right) \\ \Phi_{11\ L}(k_1) &= \frac{2 k_t \Lambda}{3\pi(1 + k_1^2 \Lambda^2)} \ . \end{aligned} \tag{A.61}$$

For the frozen turbulence assumption $\Phi_{11}(k_1)$ is directly related to $\Phi_{11}(f)$ by the wavenumber with $u_1/2\pi$ in positive k_1 domain. Figure A.2 shows the two different non-dimensionalized

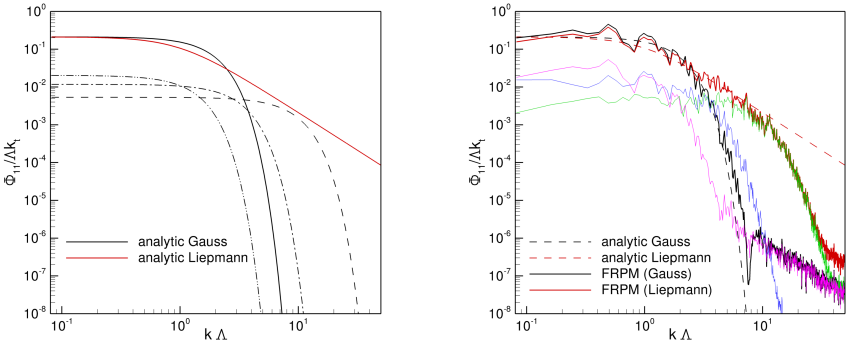

Figure A.2: Non-dimensional $\Phi_{11}(k_1)$ wavenumber spectrum Gauss vs. Liepmann: (a) analytical; (b) with FRPM test realization.

energy spectra $\Phi_{11}(k_1)$ from Eq. A.61. It can be seen, that the Liepmann spectrum has a much shallower decay in the higher wavenumber range. The single Gaussian spectra modified with the weighting function from Eq. A.57 are indicated by the dashed and dashed-dotted black lines in Fig. A.2 (a). The summation (Eq. A.56) yields the Liepmann spectrum (solid red line). For testing of this procedure in FRPM, a test patch with a constant turbulence kinetic energy distribution $k_t(\vec{x}) = const.$ was used. The graphs of the single modified Gaussian spectra realized by FRPM are shown in Fig. A.2 (b) (pink, blue and green line). The Liepmann spectrum (solid red line) can be realized by superposition of the aforementioned spectra. It matches the analytical solution. In contrast to the Gaussian spectrum (solid black line) a shallower decay in the higher wavenumber region can be observed.

A.5 PIANO Input File for CAA Airfoil Simulations

PIANO input file with standard settings used for CAA airfoil simulation with FRPM ($$ is used for comments):

```
$$ Tend 0 activate to enforce immediately regular stop of current run
QuickEnd
$$ mandatory files
$$ ----------------------------------
FilLog          logic_file.log
FilGrd          caa_mesh_file.popform
```

```
FilMean         mean_flow_file.popform
FilProc         cpu_distribution_file
$$ FRPM files
$$ ----------------------------------
FilFRPM         FRPM_patch_file.dat
FilFRPMRec      FRPM_record_file
FRPM_FILOUT     FRPM
$$ Restartfile
$$ ----------------------------------
FilRec          PIANO_record_file
Tsave           100000
$$ output:
$$ ----------------------------------
DirOut ./output
$$ Contour Output
FilNois         Contour ({'.bin','.plt'}/'.dat' depending on sign of Tout)
AreaVar0     u     first rec.  var.  out of {rho, u, v, [w,] p, [uqRPM,omega]}
AreaVar1     p     last rec.  var.  out of {rho, u, v, [w,] p, [uqRPM,omega]}
$$ Microphones
FilHis       Time  ({'.bin','.plt'}/'.dat' depending on sign of HistoryOut)
HistoryOut   -50   store time history in FilHis after HistoryOut steps
MicsVar0      p    first rec.  var.  out of {rho, u, v, [w,] p, [uqRPM,omega]}
MicsVar1      p    last rec.  var.  out of {rho, u, v, [w,] p, [uqRPM,omega]}
$$ Circle Output
FilCirc       Circle  ({'.bin','.plt'}/'.dat' depending on sign of CircOut)
CircOut      -50      store circle values after CircOut steps in FilCirc
CircNoMic     360     number of microphones refering whole circumference
CircNormVec   0.D0 0.D0 1.D0   normal vector of directivity circle
CircStartVec  1.D0 0.D0 0.D0   start vector of directivity circle
CircCentre    1.0D0 0.0D0 0.D0 centre of directivity circle
CircRadius    2.5D0   radius of directivity circle
$$ Solver
$$ ----------------------------------
dt            2.0E-4
Tend          400000
Tout          100000
Tupdate       50000
APE4
stabilimit    1.D3
new
Xref 1.0D0 0.0D0 0.D0 reference point (as normal as possible to boundary)
```

```
$$ specification of FRPM (fast Random Particle Mesh) parameters:
$$ ----------------------------------
FRPMlmin 0.002D0
FRPMlfac 6.0D0 scaling factor for patch-data length scale
FRPM_norm filtered_field
FRPM_lambsource
FRPM_RESTRICTIVE_VEL
FRPM_nparticle 450000
FRPM_NFILTER 4
FRPM_LTECOUT
$$ Damping
$$ ----------------------------------
damping     5.D-2 general damping coefficient
$$ LE
XDamp       0.0D0 0.0D0 0.D0
MagDamp     0.2D0
RadDamp     0.4D0
$$ TE
XDamp       1.0D0 0.0D0 0.D0
MagDamp     0.2D0
RadDamp     0.4D0
End
```

A.6 Modified Trailing-Edge Noise Directivity

For the use of the directivity function $\overline{D} = f(\Theta)$ according to Equation 4.4 in the turbine evaluation of Chapter 5, a modification is made to account for the geometrical difference of airfoils and the flat plate from which the theory was originally developed.

Contrary to the semi-infinite flat plate, the forward directivity of airfoils looks different. Due to their limited extend the opposite phasing sound waves can cancel out each other just in front of the airfoils. Moreover, the geometric extend of the airfoils in the thickness direction yields some shadow zone in front of the airfoil, as the trailing-edge source is hidden behind the airfoil, when looking downstream from an upstream position in extension of the chord.

Figure A.3 (a) depicts the theoretical in-plane two-dimensional directivity ($\Phi = 90\,^\circ$) for the flat plate (dashed line). It is calculated by using Equation 4.4 from Reference [3]. The difference to the NACA0012 directivity extracted from the CAA results of the BANC-II case #1 simulation (solid line) is clearly visible. The theoretical results thus need to be correct for Θ values between $\Theta_{\text{begin}} = 110\,^\circ$ to $\Theta_{\text{end}} = 260\,^\circ$. To obtain the corrected directivity function, indicated by the black circles in Figure A.3 (a), Equation A.62 can

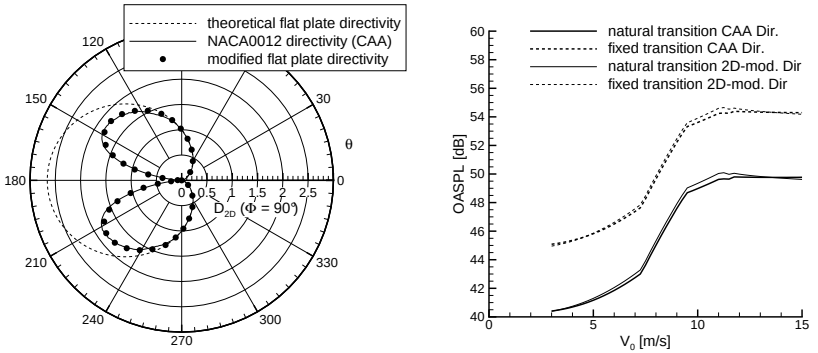

(a) (b)

Figure A.3: Modified directivity flat plate function (a) and the influence of this modification on the turbine overall sound pressure level at the IEC reference position (b).

be used.

$$\overline{D}_{\text{modified}} = \begin{cases} \overline{D}\,(\Phi = 90\,^\circ) & \text{for } \Theta < \Theta_{\text{begin}} \\ \overline{D}\,(\Phi = 90\,^\circ) \cdot F & \text{for } \Theta_{\text{begin}} \leq \Theta \leq \Theta_{\text{end}} \\ \overline{D}\,(\Phi = 90\,^\circ) & \text{for } \Theta > \Theta_{\text{end}} \end{cases} \tag{A.62}$$

Between Θ_{begin} and Θ_{end} the flat plate directivity is multiplied with the correction factor F:

$$F = 1 - \frac{\cos\left(\Theta^*\right) + 1}{2 \cdot \left[2\sin^2\left(\Theta^*\right) + 1\right]}\ , \tag{A.63}$$

with:

$$\Theta^* = \left(\frac{\Theta - \Theta_{\text{begin}}}{\Theta_{\text{end}} - \Theta_{\text{begin}}} - \frac{1}{2}\right) \cdot 2\pi\ . \tag{A.64}$$

Note, that for $\Theta = 90\,^\circ$ the directivity $\overline{D} = 1$. This legitimates the assumption in term I of Equation 5.1 to use the overall sound pressure level at the reference position and thereafter simply correct for the directivity by the addition of $10\log\left(\overline{D}\right)$ using the modified directivity of Equation A.62.

It must be said, that this approach is only needed if no directivity information exist (e.g. measurements or simulations only carried out at the reference location). If a CAA simulation also yields directivity information (e.g. due to multiple microphone positions around the trailing-edge.) these information can also be directly used in the computations making the modified analytical directivity function obsolete.

For a simplified validation both approaches are compared against each other for the noise calculations of the NREL 5 MW reference turbine. For the baseline calculations the

NACA64618 directivity, obtained directly from the CAA simulations, is used. To test the simpler approach, only the sound pressure level from the airfoil reference position is taken and combined with the modified flat plate directivity function according to Equation A.62. According to Section 5.2 the sound pressure level at the IEC reference position is calculated for the NREL turbine for different wind speeds and transition settings. The results are plotted in Figure A.3 (b). A slight overprediction of 0.5 dB due to the modified directivity can be observed. It is most prominent at a wind speed of $V_0 = 11\,\mathrm{m/s}$.

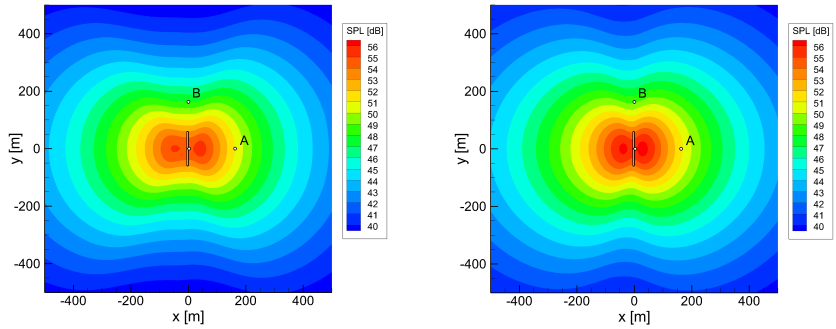

Figure A.4: Overall sound pressure at ground level in the vicinity of the Turbine (tower height $H = 100\,\mathrm{m}$, turbine location at $x = 0$ and $y = 0$) for fixed transition and a wind speed of $V_0 = 8.5\,\mathrm{m/s}$: (a) with CAA directivity information and (b) with modified two-dimensional flat plate directivity.

Figure A.4 depicts the time-averaged sound pressure levels on the ground for arbitrary observer positions around the turbine at a wind speed of $V_0 = 8.5\,\mathrm{m/s}$. While the CAA directivity (a) indicates a bigger area with higher levels downstream of the turbine, the modified directivity (b) yields an almost symmetric sound distribution. Moreover, the SPL decay, when moving into the rotor plane (positions where $x \approx 0$), is more pronounced for the modified directivity. Nevertheless, the general agreement of Figure A.4 (a) and (b) indicates the feasible use of the modified directivity with only minor drawbacks.

In FigureA.5 (a) the overall sound pressure level around the turbine for a constant distance of $R_1 = 163\,\mathrm{m}$ is plotted for both cases at a wind speed of $V_0 = 8.5\,\mathrm{m/s}$. For the upstream and downstream position the values are almost identical. For the positions of $\gamma = 90\,^\circ$ and $\gamma = 270\,^\circ$ the values for the modified directivity are about 1 dB higher.

If the current rotor dependend SPL values are analyzed (FigureA.5 (b)), it can be seen, that the variations are higher for the modified directivity, especially in the rotor plane $\gamma = 90\,^\circ$ or $\gamma = 270\,^\circ$. In contrast to the downstream position the directivity of the TBL-TEN results in a much higher variation of the received noise with changing rotor positions.

The amplitude modulation phenomena is over predicted by the modified directivity. The general effect is similar to the found with the CAA directivity.

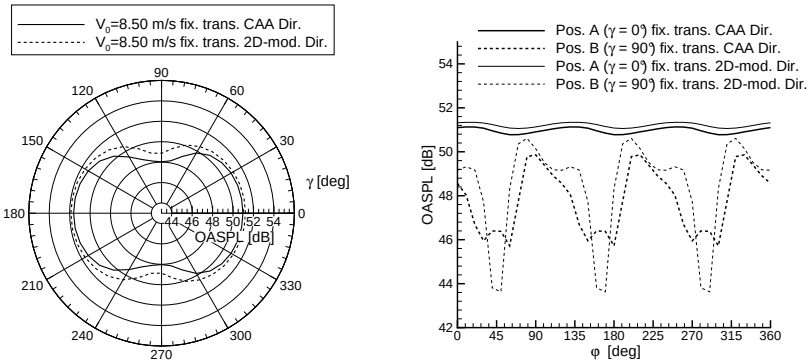

(a) (b)

Figure A.5: Overall sound pressure at ground level at a distance of $R_1 = 163\,\mathrm{m}$ and a wind speed of $V_0 = 8.5\,\mathrm{m/s}$ with fixed transition: (a) for different observer angles (γ); (b) directly downstream the turbine ($\gamma = 0$) for variable rotor positions φ.

All in all, the comparison reveals, that the modified flat plate directivity can be used with in uncertainty of 0.5 dB to 1 dB. The highest deviation are found for observer positions in the rotor plane, where precise directivity information are needed to calculate the correct OASPL values. For up- and downstream positions (e.g. the IEC reference measurement position) the modified directivity approach yields reasonable accurte results with an uncertainty of less than 0.5 dB for the overall sound pressure level.

A.7 Additional Airfoil Geometries

Figure A.6 shows the additional airfoil geometries (dashed line) simulated in Section 4.4.3 compared to original DU96-W-180 airfoil geometry (solid line).

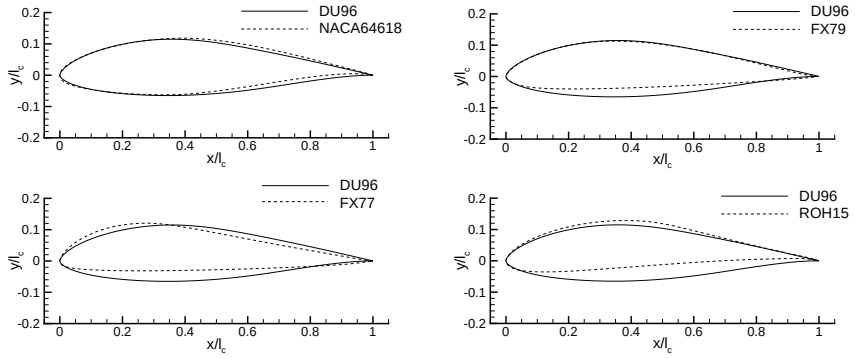

(a) (b)

Figure A.6: Additional airfoil geometries.

Bibliography

[1] GWEC: *Global Wind Report 2014: Annual market update*. Brussels, 2014

[2] EWEA: *Wind in Power: 2015 European statistics*. 2015

[3] Brooks, Thomas F. ; Pope, Stuart D. ; Marcolini, Michael A.: Airfoil self-noise and prediction. In: *NASA Refrence Publication* (1989), Nr. 1218, S. 1–137

[4] Wagner, S. ; Bareiss, R. ; Guidati, G.: *Wind Turbine Noise*. Berlin and , New York : Springer, 1996. – ISBN 3–540–60592–4

[5] Lighthill, M. J.: On Sound Generated Aerodynamically. I. General Theory. In: *Proceedings of the Royal Society A: Mathematical, Physical and Engineering Sciences* 211 (1952), Nr. 1107, S. 564–587. http://dx.doi.org/10.1098/rspa.1952.0060. – DOI 10.1098/rspa.1952.0060. – ISSN 1364–5021

[6] Lighthill, M. J.: On Sound Generated Aerodynamically. II. Turbulence as a Source of Sound. In: *Proceedings of the Royal Society A: Mathematical, Physical and Engineering Sciences* 222 (1954), Nr. 1148, S. 1–32. http://dx.doi.org/10.1098/rspa.1954.0049. – DOI 10.1098/rspa.1954.0049. – ISSN 1364–5021

[7] Curle, N.: The Influence of Solid Boundaries upon Aerodynamic Sound. In: *Proceedings of the Royal Society A: Mathematical, Physical and Engineering Sciences* 231 (1955), Nr. 1187, S. 505–514. http://dx.doi.org/10.1098/rspa.1955.0191. – DOI 10.1098/rspa.1955.0191. – ISSN 1364–5021

[8] Ffowcs Williams, J. E. ; Hawkings, D. L.: Sound Generation by Turbulence and Surfaces in Arbitrary Motion. In: *Philosophical Transactions of the Royal Society A: Mathematical, Physical and Engineering Sciences* 264 (1969), Nr. 1151, S. 321–342. http://dx.doi.org/10.1098/rsta.1969.0031. – DOI 10.1098/rsta.1969.0031. – ISSN 1364–503X

[9] Ffowcs Williams, J. E. ; Hall, L. H.: Aerodynamic sound generation by turbulent flow in the vicinity of a scattering half plane. In: *Journal of Fluid Mechanics* 40 (1970), Nr. 04, S. 657–670

[10] Howe, M.S: A review of the theory of trailing edge noise. In: *Journal of Sound and Vibration* 61 (1978), Nr. 3, S. 437–465. http://dx.doi.org/10.1016/0022-460X(78)90391-7. – DOI 10.1016/0022–460X(78)90391–7. – ISSN 0022460X

[11] Crighton, D. G. ; Leppington, F. G.: Scattering of aerodynamic noise by a semi-infinite compliant plate. In: *Journal of Fluid Mechanics* 43 (1970), Nr. 04, S. 721. http://dx.doi.org/10.1017/S0022112070002690. – DOI 10.1017/S0022112070002690

[12] Crighton, D. G.: Radiation Properties of the Semi-Infinite Vortex Sheet. In: *Proceedings of the Royal Society A: Mathematical, Physical and Engineering Sciences* 330 (1972), Nr. 1581, S. 185–198. http://dx.doi.org/10.1098/rspa.1972.0139. – DOI 10.1098/rspa.1972.0139. – ISSN 1364–5021

[13] Chase, David M.: Sound Radiated by Turbulent Flow off a Rigid Half-Plane as Obtained from a Wavevector Spectrum of Hydrodynamic Pressure. In: *The Journal of the Acoustical Society of America* 52 (1972), Nr. 3B, S. 1011. http://dx.doi.org/10.1121/1.1913170. – DOI 10.1121/1.1913170. – ISSN 00014966

[14] Chase, David M.: Noise Radiated from an Edge in Turbulent Flow. In: *AIAA Journal* 13 (1975), Nr. 8, S. 1041–1047. http://dx.doi.org/10.2514/3.60502. – DOI 10.2514/3.60502. – ISSN 0001–1452

[15] Amiet, R.K: Acoustic radiation from an airfoil in a turbulent stream. In: *Journal of Sound and Vibration* 41 (1975), Nr. 4, S. 407–420. http://dx.doi.org/10.1016/S0022-460X(75)80105-2. – DOI 10.1016/S0022–460X(75)80105–2. – ISSN 0022460X

[16] Amiet, R.K: Noise due to turbulent flow past a trailing edge. In: *Journal of Sound and Vibration* 47 (1976), Nr. 3, S. 387–393. http://dx.doi.org/10.1016/0022-460X(76)90948-2. – DOI 10.1016/0022–460X(76)90948–2. – ISSN 0022460X

[17] Brooks, T.F ; Hodgson, T.H: Trailing edge noise prediction from measured surface pressures. In: *Journal of Sound and Vibration* 78 (1981), Nr. 1, S. 69–117. http://dx.doi.org/10.1016/S0022-460X(81)80158-7. – DOI 10.1016/S0022–460X(81)80158–7. – ISSN 0022460X

[18] Parchen, Rene ; TNO Institute of Applied (Hrsg.): *Progress Report DRAW: A Prediction Scheme for Trailing-Edge Noise Based on Detailed Boundary-Layer Characteristics: TNO Rept. HAG-RPT-980023*. Netherlands, 1998

[19] Moriarty, P. ; Migliore, P.: *Semi-Empirical Aeroacoustic Noise Prediction Code for Wind Turbines: NREL/TP-500-34478*. 2003

[20] Moriarty, Patrick ; Guidati, Gianfranco ; Migliore, Paul: Recent Improvement of a Semi-Empirical Aeroacoustic Prediction Code for Wind Turbines. In: *10th AIAA/CEAS Aeroacoustics Conference*, 2004, S. 1–25

[21] Schepers, J. G. ; Curvers, A. P. W. M. ; Oerlemans, S. ; Braun, K. ; Lutz, T. ; Herrig, A. ; Wuerz, W. ; Mantesanz, A. ; Garcillán, L. ; Fisher, M. ; Koegler, K. ; Maeder, T. ; ECN Wind Energy (Hrsg.): *SIROCCO: Silent rotors by acoustic optimisation: ECN-M–07-064*. 2007

[22] Lutz, Thorsten ; Herrig, Andreas ; Würz, Werner ; Kamruzzaman, Mohammad ; Krämer, Ewald: Design and Wind-Tunnel Verification of Low-Noise Airfoils for Wind Turbines. In: *AIAA Journal* 45 (2007), Nr. 4, S. 779–785. http://dx.doi.org/10.2514/1.27658. – DOI 10.2514/1.27658. – ISSN 0001–1452

[23] Oerlemans, S. ; Sijtsma, P. ; Méndez López, B.: Location and quantification of noise sources on a wind turbine. In: *Journal of Sound and Vibration* 299 (2007), Nr. 4-5, S. 869–883. http://dx.doi.org/10.1016/j.jsv.2006.07.032. – DOI 10.1016/j.jsv.2006.07.032. – ISSN 0022460X

[24] Oerlemans, S. ; Schepers, J. G.: *Prediction of wind turbine noise and validation against experiment*. 2009

[25] Oerlemans, Stefan ; Fisher, Murray ; Maeder, Thierry ; Kögler, Klaus: Reduction of Wind Turbine Noise Using Optimized Airfoils and Trailing-Edge Serrations. In: *AIAA Journal* 47 (2009), Nr. 6, S. 1470–1481. http://dx.doi.org/10.2514/1.38888. – DOI 10.2514/1.38888. – ISSN 0001–1452

[26] Oerlemans, S. ; Schepers, J. G.: Prediction of wind turbine noise and validation against experiment. In: *Noise Notes* 9 (2010), Nr. 2, S. 3–28. http://dx.doi.org/10.1260/1475-4738.9.2.3. – DOI 10.1260/1475–4738.9.2.3. – ISSN 1475–4738

[27] Hutcheson, Florence V. ; Brooks, Thomas F.: Measurement of Trailing Edge Noise Using Directional Array and Coherent Output Power Methods: 8th AIAA/CEAS Aeroacoustics Conference. (2002)

[28] Hutcheson, Florence V. ; Brooks, Thomas F.: Effects of angle of attack and velocity on trailing edge noise. In: *AIAA paper* (2004), Nr. 1031, S. 2004

[29] Ewert, Roland: RPM - the fast Random Particle-Mesh method to realize unsteady turbulent sound sources and velocity fields for CAA applications. In: AIAA (Hrsg.): *13th AIAA/CEAS Aeroacoustics Conference*, 2007, S. 1–27

[30] Ewert, R. ; Appel, C. ; Dierke, J. ; Herr, M.: RANS/CAA based prediction of NACA 0012 broadband trailing edge noise and experimental validation: AIAA. (2009)

[31] Ewert, R. ; Dierke, J. ; Siebert, J. ; Neifeld, A. ; Appel, C. ; Siefert, M. ; Kornow, O.: CAA broadband noise prediction for aeroacoustic design. In: *Journal of Sound and Vibration* 330 (2011), Nr. 17, S. 4139–4160. http://dx.doi.org/10.1016/j.jsv.2011.04.014. – DOI 10.1016/j.jsv.2011.04.014. – ISSN 0022460X

[32] Hau, Erich: *Windkraftanlagen: Grundlagen, Technik, Einsatz, Wirtschaftlichkeit*. 4. Berlin : Springer, 2008. – ISBN 3540721509

[33] Hansen, Martin O. L.: *Aerodynamics of wind turbines*. 2. London and Sterling, VA : Earthscan, 2008. – ISBN 1844074382

[34] Gasch, Robert: *Windkraftanlagen: Grundlagen, Entwurf, Planung und Betrieb*. 7. Aufl. Wiesbaden : Vieweg + Teubner, 2011 (Studium). – ISBN 3834814601

[35] Burton, Tony: *Handbook of wind energy*. Chichester [u.a.] : Wiley, 2001. – ISBN 0471489972

[36] Ferziger, Joel H. ; Perić, M.: *Computational methods for fluid dynamics*. 3rd, rev. ed. Berlin and New York : Springer, 2002. – ISBN 3540420746

[37] Anderson, John D.: *Computational fluid dynamics: The basics with applications*. New York : McGraw-Hill, 1995 (McGraw-Hill series in mechanical engineering). – ISBN 0070016852

[38] Glauert, H.: Airplane Propellers. Version: 1935. http://dx.doi.org/10.1007/978-3-642-91487-4{_}3. In: Durand, William F. (Hrsg.): *Aerodynamic Theory*. Berlin, Heidelberg : Springer Berlin Heidelberg, 1935. – DOI 10.1007/978–3–642–91487–4_3. – ISBN 978–3–642–89630–9, S. 169–360

[39] Troen, Ib ; Petersen, Erik L.: *European wind atlas*. Roskilde, Denmark : Published for the Commission of the European Communities, Directorate-General for Science, Research, and Development, Brussels, Belgium by Risø National Laboratory, 1989. – ISBN 87–550–1482–8

[40] DLR TAU: *Technical Documentation of the DLR TAU-Code Release 2015.1.0*. Braunschweig, 2015

[41] Menter, F. R.: Two-equation eddy-viscosity turbulence models for engineering applications. In: *AIAA Journal* 32 (1994), Nr. 8, S. 1598–1605. http://dx.doi.org/10.2514/3.12149. – DOI 10.2514/3.12149. – ISSN 0001–1452

[42] Wilcox, David C.: *Turbulence modeling for CFD*. 3. ed. La Cañada and Calif : DCW Industries, 2006. – ISBN 1928729088

[43] Delfs, Jan W. ; Ewert, Roland ; Bauer, Markus ; Dierke, Jürgen ; DLR – German Aerospace Center (Hrsg.): *Numerical Simulation of Aerodynamic Noise with PIANO*. Braunschweig, 2015

[44] Ewert, Roland: Acoustic perturbation equations based on flow decomposition via source filtering. In: *Journal of Computational Physics* 188 (2003), Nr. 2, 365–398. http://dx.doi.org/10.1016/S0021-9991(03)00168-2. – DOI 10.1016/S0021–9991(03)00168–2. – ISSN 00219991

[45] Tam, C. ; Webb, J.: Dispersion-Relation-Preserving Finite Difference Schemes for Computational Acoustics. In: *Journal of Computational Physics* 107 (1993), S. 262–281. – ISSN 00219991

[46] Tam, Christopher K. W. ; Webb, Jay C. ; DONG, ZHONG: A study of the sort wave components in computational acoustics. In: *Journal of Computational Acoustics* 01 (1993), Nr. 01, S. 1–30. http://dx.doi.org/10.1142/S0218396X93000020. – DOI 10.1142/S0218396X93000020. – ISSN 0218–396X

[47] Hu, F. Q. ; Hussaini, M. Y. ; Manthey, J. L.: Low-Dissipation and Low-Dispersion Runge–Kutta Schemes for Computational Acoustics. In: *Journal of Computational Physics* 124 (1996), Nr. 1, S. 177–191. http://dx.doi.org/10.1006/jcph.1996.0052. – DOI 10.1006/jcph.1996.0052. – ISSN 00219991

[48] Ewert, R. ; Edmunds, R.: CAA Slat Noise Studies Applying Stochastic Sound Sources Based on Solenoidal Digital Filters. In: AIAA (Hrsg.): *11th AIAA/CEAS Aeroacoustics Conference*, 2005, S. 1–23

[49] Tam, Christopher W. K. ; Auriault, Laurent: Jet Mixing Noise from Fine-Scale Turbulence. In: *AIAA Journal* 37 (1999), Nr. 2, S. 145–153. http://dx.doi.org/10.2514/2.691. – DOI 10.2514/2.691. – ISSN 0001–1452

[50] Bailly, Christophe ; Juve, Daniel: A stochastic approach to compute subsonic noise using linearized Euler's equations. In: *5th AIAA/CEAS Aeroacoustics Conference and Exhibit*, 1999, S. 496–506

[51] Lowson, Martin V. ; Flow Solutions Ltd (Hrsg.): *Assesment and Prediction of Wind Turbine Noise: Flow Solutions Report ETSU/W/13/00284/REP*. 1992

[52] Pinder, J. N.: Mechanical noise from wind turbines. In: *Wind Engineering* 16 (1992), Nr. 3, S. 158–168

[53] Fink, Martin R.: Noise Component Method for Airframe Noise. In: *Journal of Aircraft* 16 (1979), Nr. 10, S. 659–665. http://dx.doi.org/10.2514/3.58586. – DOI 10.2514/3.58586. – ISSN 0021–8669

[54] Herr, Michaela: *Trailing-Edge Noise - Reduction Concepts and Scaling Laws: Dissertation: DLR-Forschungsbericht DLR-FB-2013-32*. Bd. DLR-FB-2013-32. 2013

[55] Ewert, R.: Broadband slat noise prediction based on CAA and stochastic sound sources from a fast random particle-mesh (RPM) method. In: *Computers & Fluids* 37 (2008), S. 369–387. – ISSN 00457930

[56] Gerhold, T. ; Galle, M. ; Friedrich, O. ; Evans, J.: Calculation of complex three-dimensional configurations employing the DLR-tau-code. In: *35th Aerospace Sciences Meeting and Exhibit*, 1997, S. 1–10

[57] Schwamborn, D. ; Gerhold, T. ; Heinrich, R.: The DLR TAU-Code: Recent Applications in Research and Industry. In: *Proc. of Europ. Conf. on Computational Fluid Dynamics ECCOMAS CFD*, 2006, 1–25

[58] Bauer, Marcus ; Deutsches Zentrum für Luft- und Raumfahrt e.V. (Hrsg.): *Airframe noise prediction using a discontinuous Galerkin method: Dissertation: Forschungsbericht*. Braunschweig, 2011

[59] Schlichting, Hermann ; Gersten, Klaus: *Boundary layer theory: With 22 tables*. 8. Berlin[u.a.] : Springer, 2003 (Physics and astronomy online library). – ISBN 3540662707

[60] Timmer, W.A ; Rooij, R.P.J.O.M: Summary of the Delft University Wind Turbine Dedicated Airfoils. In: *41st Aerospace Sciences Meeting and Exhibit*, 2003, S. 1–11

[61] Jonkman, J. ; Butterfield, S. ; Musial, W. ; Scott, G.: Definition of a 5-MW Reference Wind Turbine for Offshore System Development. (2009)

[62] Menter, F. R. ; Langtry, R. B. ; Likki, S. R. ; Suzen, Y. B. ; Huang, P. G. ; Voelker, S.: A Correlation-Based Transition Model Using Local Variables—Part I: Model Formulation. In: *Journal of Turbomachinery* 128 (2006), Nr. 3, S. 413. http://dx.doi.org/10.1115/1.2184352. – DOI 10.1115/1.2184352. – ISSN 0889504X

[63] Abbott, Ira H. ; Doenhoff, Albert E. v.: *Theory of wing sections: Including a summary of airfoil data*. New York : Dover, 1959. – ISBN 978–0486605869

[64] Roache, P. J.: Perspective: A Method for Uniform Reporting of Grid Refinement Studies. In: *Journal of Fluids Engineering* 116 (1994), Nr. 3, S. 405. http://dx.doi.org/10.1115/1.2910291. – DOI 10.1115/1.2910291. – ISSN 00982202

[65] Bauer, Marcus ; Dierke, Juergen ; Ewert, Roland: Application of a Discontinuous Galerkin Method to Predict Airframe Noise. In: AIAA (Hrsg.): *15th AIAA/CEAS Aeroacoustics Conference (30th AIAA Aeroacoustics Conference)*, 2009, S. 1–24

[66] Bauer, Marcus ; Ewert, Roland: Slat Noise Prediction Using Discontinuous Galerkin Method and Stochastic Turbulent Sound Source. In: AIAA (Hrsg.): *16th AIAA/CEAS Aeroacoustics Conference*, American Institute of Aeronautics and Astronautics, 2010. – ISBN 978–1–60086–955–6, S. 1–22

[67] Bauer, Marcus ; Dierke, Jürgen ; Ewert, Roland: Application of a Discontinuous Galerkin Method to Discretize Acoustic Perturbation Equations. In: *AIAA Journal* 49 (2011), Nr. 5, S. 898–908. http://dx.doi.org/10.2514/1.J050333. – DOI 10.2514/1.J050333. – ISSN 0001–1452

[68] Anderson, John D.: *Fundamentals of aerodynamics*. 4. Boston : McGraw-Hill Higher Education, 2007 (McGraw-Hill series in aeronautical and aerospace engineering). – ISBN 0071254080

[69] Tam, Christopher ; DONG, ZHONG: Wall boundary conditions for high-order finite difference schemes in computational aeroacoustics. In: *32nd Aerospace Sciences Meeting and Exhibit*, 1994, S. 1788–1796

[70] Rautmann, Christof ; Dierke, Juergen ; Ewert, Roland ; Hu, Nan ; Delfs, Jan: Generic Airfoil Trailing-Edge Noise Prediction using Stochastic Sound Sources from Synthetic Turbulence. In: AIAA (Hrsg.): *20th AIAA/CEAS Aeroacoustics Conference*, 2014, S. 1–21

[71] Liepmann, H. W. ; Laufer, J. ; Liepmann, Kate ; National Advisory Committee for Aeronautics (Hrsg.): *On the spectrum of isotropic turbulence: NACA Technical Notes*. 1951 (NACA-TN-2473)

[72] Herr, M. ; Kamruzzaman, M.: Benchmarking of Trailing-Edge Noise Computations|Outcome of the BANC-II Workshop: AIAA. (2013)

[73] Herr, M. ; Bahr, C. ; Kamruzzaman, M.: *Workshop Category 1: Trailing-Edge Noise. Problem Statement for the AIAA/CEAS Second Workshop on Benchmark Problems for Airframe Noise Computations (BANC-II): June 7-8 2012, Colorado Springs, Colorado, USA*. https://info.aiaa.org/tac/ASG/FDTC/DG/BECAN_files_/BANCII_category1. Version: 2012

[74] Herrig, Andreas: *Validation and application of a hot-wire based method for trailing-edge noise measurements on airfoils: Doctoral thesis*. Stuttgart : IAG, 2011

[75] Townsend, A. A.: *The structure of turbulent shear flow*. 2. Cambridge [Eng.], New York : Cambridge University Press, 1980 (Cambridge monographs on mechanics and applied mathematics). – ISBN 0521298199

[76] SCHLINKER, R. ; AMIET, R.: Helicopter rotor trailing edge noise. In: *7th Aeroacoustics Conference*, 1981, S. 1–25

[77] Eastman ; Jacobs, N. ; Kenneth, E. ; Ward, E. ; Pinkerton, Robert M.: *The Characteristics of 78 Related Airfoil Sections from Tests in the Variable-density Wind Tunnel: NACA Rept. No. 460*. 1933

[78] IEC: *IEC 64100-11 second edition*. 2. 2002

[79] Bowdler, Dick: Amplitude modulation of wind turbine noise: a review of the evidence. In: *Institute of Acoustics Bulletin 33.4* 33 (2008), Nr. 4, S. 31–41

[80] Lee, Seunghoon ; Kim, Kyutae ; Choi, Wooyoung ; Lee, Soogab: Annoyance caused by amplitude modulation of wind turbine noise. In: *Noise Control Engineering Journal* 59 (2011), Nr. 1, S. 38. http://dx.doi.org/10.3397/1.3531797. – DOI 10.3397/1.3531797. – ISSN 07362501

[81] Drela, Mark: XFOIL: An Analysis and Design System for Low Reynolds Number Airfoils. Version: 1989. http://dx.doi.org/10.1007/978-3-642-84010-4{_}1. In: Brebbia, C. A. (Hrsg.) ; Orszag, S. A. (Hrsg.) ; Seinfeld, J. H. (Hrsg.) ; Spanos, P. (Hrsg.) ; Cakmak, A. S. (Hrsg.) ; Silvester, P. (Hrsg.) ; Desai, C. S. (Hrsg.) ; Pinder, G. (Hrsg.) ; McCrory, R. (Hrsg.) ; Yip, S. (Hrsg.) ; Leckie, F. A. (Hrsg.) ; Ponter, A. R. S. (Hrsg.) ; Holz, K.-P (Hrsg.) ; Bathe, K.-J (Hrsg.) ; Connor, J. (Hrsg.) ; Wunderlich, W. (Hrsg.) ; Argyris, J. (Hrsg.) ; Mueller, Thomas J. (Hrsg.): *Low Reynolds Number Aerodynamics* Bd. 54. Berlin, Heidelberg : Springer Berlin Heidelberg, 1989. – DOI 10.1007/978–3–642–84010–4_1. – ISBN 978–3–540–51884–6, S. 1–12

[82] Bak, Christian: *Risø R, Report*. Bd. 1611: *Research in aeroelasticity EFP-2006*. Roskilde : Risø National Laboratory, 2007. – ISBN 978–87–550–3610–9

[83] Spera, David A.: *Wind turbine technology: Fundamental concepts of wind turbine engineering*. New York : ASME Press, 1994. – ISBN 0791812057

[84] Alecu, Teodor I. ; Voloshynovskiy, Sviatoslav ; Pun, Thierry: The gaussian transform. In: *EUSIPCO2005, 13th European Signal Processing Conference* Bd. 2005, 2005, S. 4–8